A Study of $B \to J/\psi K^{(*)0} X$ Decays

A thesis presented
by

Stephen John Bailey

to
The Department of Physics
in partial fulfillment of the requirements
for the degree of
Doctor of Philosophy
in the subject of

Physics

Harvard University
Cambridge, Massachusetts
April 2001

Thesis advisor
John Huth

Author
Stephen John Bailey

A Study of $B \to J/\psi K^{(*)0} X$ Decays

Abstract

This thesis reports the results of a study of $B \to J/\psi K^{(*)0} X$ decays. The decay modes reported here have not been previously observed nor are there any prior branching ratio limits. We see evidence for several new decay modes and describe their potential for CKM related physics measurements. The branching ratio measurements are summarized as:

- $\mathrm{BR}(B^0 \to J/\psi K^{*0}\pi^+\pi^-) = (8.0 \pm 2.2 \pm 1.5) \times 10^{-4}$
  - Contribution seen from $B^0 \to \psi(2S)K^{*0}$
  - No other identifiable substructure seen
- $\mathrm{BR}(B^0 \to J/\psi K^0\pi^+\pi^-) = (1.1 \pm 0.4 \pm 0.2) \times 10^{-3}$
  - $\mathrm{BR}(B^0 \to J/\psi K^0\rho^0) = (5.8 \pm 3.1 \pm 1.2) \times 10^{-4}$
  - $\mathrm{BR}(B^0 \to J/\psi K^{*+}\pi^-) = (8.3 \pm 4.4 \pm 1.7) \times 10^{-4}$

  Contributions also seen from $B^0 \to J/\psi K_1(1270)$ and $B^0 \to \psi(2S)K^0$.
- $\mathrm{BR}(B_s \to J/\psi K^0\pi^\pm K^\mp) < 3.9 \times 10^{-4}$ (Feldman Cousins 95% CL)
- $\mathrm{BR}(B_s \to J/\psi \bar{K}^{*0}) < 1.0 \times 10^{-4}$ (Feldman Cousins 95% CL)

For some reason it has not yet trickled down to the man on the street that some physicists now are a bunch of wild-eyed, raving mystics. For they have perfected their instruments and methods just enough to whisk away the crucial veil, and what stands revealed is the Cheshire cat's grin.

— Annie Dillard, *Pilgrim at Tinker Creek*

There will be a time, there will be time
To prepare a face to meet the faces that you meet;
There will be time to murder and create,
And time for all the works and days of hands
That lift and drop a question on your plate;
Time for you and time for me,
And time yet for a hundred indecisions,
And for a hundred visions and revisions,
Before the taking of a toast and tea.

— T.S. Eliot, The Love Song of J. Alfred Prufrock

Acknowledgements

A huge thanks goes to Petar Maksimović for his assistance with this analysis. He introduced me to CDF B physics and guided me through arcane code, documentation, and datasets. Petar's obsession with reuseable code and general solutions produced the reconstruction code that allowed me to easily study many different B decay modes. He also shared Run II hardware responsibilities with me which freed me to occasionally hide and work on my thesis while he handled SVX DAQ issues. Having a close connection to Petar has enabled me to graduate much sooner than would have otherwise been possible.

Thanks also to my thesis advisor, John Huth, who invariably provided helpful advice when we actually managed to coordinate our schedules and talk. He also generously flew me to exotic destinations to study or give talks in the name of physics. His willingness to let me frequently return to Cambridge from Fermilab is largely responsible for keeping me in high energy rather than some other field of physics.

My thesis committee has also been helpful. Michael answered my questions about supersymmetry. Howard answered my questions about calculating the B mixing box diagram and thankfully did not ask me to reproduce it during my orals. Melissa deserves a huge thanks for crucial and timely advice — she was the one who finally convinced me to do a Run I thesis and thus saved me several years of graduate school.

Lester has done an excellent job of taking over my life at Fermilab, including my hardware responsibilities, my room in West Chicago, and my garden plot. For once I think I'm glad I don't have a girlfriend.

Thanks to Nathan for his help with the SRC and for not getting caller ID to block my calls for help after I moved out to Fermilab. Thanks also to the rest of the HEPL staff who have assisted my work through the years.

Thanks to my housemates in recent years: Carter found us a wonderful place in West Chicago and is the best hardware student I know. Kirby, for good or for bad, has influenced my life by exposing me to a TV show I get excited about (Iron Chef) and even more surprisingly, getting me to watch (even follow!) college basketball.

Thanks to Paul for many conversations and for bike and car advice.

Thanks to David van Dyk, my personal statistician, for his frequent help and continued friendship.

Speaking of David, thanks to everyone who housed me during my frequent trips back to Cambridge: Paul, Andy, Mary, and at least four different Davids.

How can I thank my parents enough? They raised me well, guided me in what was right and nurtured my creativity and intellect. And as I grew older, they gave me the freedom to explore even when I sometimes took directions they would rather not have me go. Thanks. I love you.

Thanks to my grandparents who nurtured me as a child. My Bailey grandparents gave me my first physics book. Grandma Bailey took me to the Seattle Science Center and then, in her own quiet way, occasionally blew my mind with outings like a Metallica laser show. Grandpa Bailey once commented, "You do realize that the world's greatest problems have nothing to do with physics, don't you?" He is right, of course. I spent many hours in Grandpa Jones' workshop building all sorts of contraptions, and Grandma Jones flew kites with me and chased my hot air balloon down into the canyon when it flew higher and further than expected.

Tom Trainor taught me to think like a physicist.

And of course there are many others. Peter and Wendy and company kept me sane in suburbia. Alicia has been a faithful friend, providing both support and challenge to always grow. I've enjoyed many conversations over beer or coffee with Rebecca. I've had useful physics conversations with Isi, Amol, Alexey, Andy, and others. My class of physics grad students has a good social life that made grad school quite enjoyable.

But most of all I would like to thank God for giving us a world which is orderly enough to be amenable to study, yet subtle enough to be both interesting and beautiful. I am grateful for the tremendous privilege of studying it.

Contents

List of Figures

List of Tables

Chapter 1

Introduction

The Standard Model of particle physics has been extremely successful in explaining observed phenomena regarding fundamental particles and their interactions. In some cases such as the existence and masses of the gauge bosons it has had stunning predictive success. In other cases such as CP violation the Standard Model explanation is more retrodictive than predictive, yet even with CP violation the explanation predicted a third generation of quarks long before there was any experimental evidence for them.

Despite its success, there there is good reason to believe that the Standard Model is at best incomplete. *E.g.*, currently the quark and lepton masses are simply inputs to the Standard Model. Yet their hierarchy has a suggestive structure and a more predictive theory might explain that structure using a smaller number of input parameters. A more specific problem arises in calculating the mass corrections to the Higgs boson. The loop terms are potentially divergent and require extreme fine tuning of the parameters (to the tune of one part in 10^{16}) to cancel the divergences. Although this is possible in principle, this difficulty is a primary motivation for theories such as supersymmetry [1] which provide a more natural cancellation of the divergences.

CP violation with B mesons, to be described in chapter 2, is one of the few remaining areas of the Standard Model which has not yet been precision tested. It is also a portion of the Standard Model which is highly predictive — only experimental difficulties have prevented its detailed study prior to current experiments. Additionally, non-Standard Model theories often predict different CP violation results which makes this a promising area of study.

This thesis is a study of B meson decays to a J/ψ plus a neutral kaon plus additional charged pions and kaons. $B \to J/\psi X$ decays[1] have played a central role in B physics measurements. Studies of these decays benefit from precise theoretical predictions as well as the experimental advantages of the clean $J/\psi \to \mu^+\mu^-$ signature.

[1] Throughout this thesis, "X" will refer to any combination of particles. Thus $B \to J/\psi X$ includes $B \to J/\psi K$, $B \to J/\psi K\pi\pi$, etc.

This thesis adds several new decay modes to the set of known $B \to J/\psi X$ decays. In some cases we have ideas for physics measurements to perform with these modes when we have more data; in other cases, their usefulness is not yet known. The decay modes studied here are not part of the standard B physics phenomenology literature, but B physics phenomenologists have shown remarkable resourcefulness in finding uses for nearly every known B decay. We hope this thesis highlights a class of new B decays which will be useful for B physics measurements in the future.

Chapter 2

Theoretical Overview

2.1 History

The development of the Standard Model has enjoyed fruitful interchange between theory and experiment. An example of this beneficial exchange is in the area of the symmetries of spatial inversion (also known as parity, P) and exchange of particle and anti-particle (charge conjugation, C).

Until the 1950's these were presumed to be good symmetries — that all the laws of physics were invariant under these transformations. Indeed, at the time there was ample evidence for this assumption in strong and electromagnetic interactions. Yet there was an outstanding puzzle in the experimental data: there appeared to be two particles with identical mass, spin, lifetime, and charge; one of them decayed to two pions (an even parity state) and one decayed to three pions (an odd parity state). Because of P symmetry, these were assumed to be different particles.

In 1956 Lee and Yang [2] suggested that these were in fact the same particle (now known as the K^+) and that parity was not conserved in weak decays. They proposed several experiments which were quickly performed [3, 4] to experimentally confirm that parity was not a good symmetry of weak interactions. The results were such that although P was violated, C was simultaneously violated in such manner that the combination CP appeared to be a valid symmetry of weak interactions.

The previous year, Gell-Mann and Pais [5] had noted that neutral kaons (at that time known as θ^0 mesons) could mix between their particle and anti-particle states via flavor changing weak interactions. Based upon C symmetry (which was still thought to be a good symmetry), they predicted that in addition to the known C-even eigenstate which decays to two pions, there would be a C-odd eigenstate that would decay to two pions and a photon, or three pions. The predicted decay rates to these final states is much less than to two pions[1], thus they predicted that the C-odd

[1]For the three pion final state, the suppressed rate is largely due to phase space: The mass of three pions is barely below that of a neutral kaon, thus there is very little phase space available for the decay. The decay to two pions has much more phase space available and proceeds at an

eigenstate would have a much longer lifetime than the C-even eigenstate[2].

Although the C symmetry assumption was incorrect, the basic argument applies equally well to CP eigenstates and in 1956 the long lived $K_L^0 \to \pi\pi\pi$ was discovered [6]. It appeared that the neutral kaon mass eigenstates came in two forms: a short lived CP-even eigenstate (the K_S^0) and a long lived CP-odd eigenstate (the K_L^0). Thus it came as quite a surprise in 1964 when $K_L^0 \to \pi\pi$ decays were observed [7]. Apparently the neutral kaon mass eigenstates are different than the CP eigenstates — this is evidence for CP violation.

To explain CP violation, Kobayashi and Maskawa [8] noted that if there were three generations of quarks whose mass eigenstates were different from their weak eigenstates, the mixing matrix relating these two bases would in general have a complex phase which could give rise to CP violation in the Standard Model Lagrangian. At the time even the charmed quark of the second generation had not yet been discovered, yet their prediction of three quark generations has since been confirmed and the complex phase in the quark mixing matrix remains as the Standard Model explanation for CP violation.

2.2 The $V_{\rm CKM}$ Quark Mixing Matrix

The mixing matrix $V_{\rm CKM}$ proposed by Kobayashi and Maskawa[3] relates the mass eigenstates of down type quarks ($d\,s\,b$) to their weak eigenstates ($d'\,s'\,b'$):

$$\begin{pmatrix} d' \\ s' \\ b' \end{pmatrix} = \begin{pmatrix} V_{ud} & V_{us} & V_{ub} \\ V_{cd} & V_{cs} & V_{cb} \\ V_{td} & V_{ts} & V_{tb} \end{pmatrix} \begin{pmatrix} d \\ s \\ b \end{pmatrix} \tag{2.1}$$

The components of this matrix enter the electroweak Lagrangian in the charged current interaction:

$$\mathcal{L}_{Wq} = -\frac{g}{2\sqrt{2}} \left[\bar{u}_i \gamma^\mu W_\mu^+ (1-\gamma_5) d_i' + \bar{d}_i' \gamma^\mu W_\mu^- (1-\gamma_5) u_i \right] \tag{2.2}$$

$$= -\frac{g}{2\sqrt{2}} \left[\bar{u}_i \gamma^\mu W_\mu^+ (1-\gamma_5) V_{ij} d_j + V_{ij}^* \bar{d}_j \gamma^\mu W_\mu^- (1-\gamma_5) u_i \right] \tag{2.3}$$

where u and d represent the vector of up- and down-type quarks and V is the $V_{\rm CKM}$ quark mixing matrix. *E.g.*, the matrix element for a $b \to c$ quark decay has a V_{cb} term. The off diagonal elements of $V_{\rm CKM}$ allow inter-generational quark decay.

appropriately faster rate.

[2]Note that only neutral particles which are their own anti-particles can be eigenstates of C. Gell-Mann and Pais suggested the eigenstates $\theta_{1,2}^0 = \theta^0 \pm \bar{\theta}^0 (= K_{S,L}^0)$. Since a charged particle cannot be an eigenstate of C (or CP), the argument does not apply to K^+: although it can decay to either two or three pions, there isn't a long lived and a short lived version of the charged kaon.

[3]The "C" in the $V_{\rm CKM}$ quark mixing matrix is for Cabibbo who formed the theory of two generation quark mixing.

In general a 3×3 complex matrix has 18 free parameters but in the case of the $V_{\rm CKM}$ matrix, five quark phase adjustments[4] and nine unitarity constraints reduce the number of free parameters to three amplitudes and one phase [9]. There is some freedom in the parameterization chosen [10]; the standard parameterization [11] uses three angles and one phase:

$$V_{\rm CKM} = \begin{pmatrix} c_{12}c_{13} & s_{12}c_{13} & s_{13}e^{-i\delta} \\ -s_{12}c_{23} - c_{12}s_{23}s_{13}e^{i\delta} & c_{12}c_{23} - s_{12}s_{23}s_{13}e^{i\delta} & s_{23}c_{13} \\ s_{12}s_{23} - c_{12}c_{23}s_{13}e^{i\delta} & -c_{12}s_{23} - s_{12}c_{23}s_{13}e^{i\delta} & c_{23}c_{13} \end{pmatrix} \tag{2.4}$$

where $c_{ij} = \cos\theta_{ij}$ and $s_{ij} = \sin\theta_{ij}$ for the generation labels 1,2,3. This parameterization places the terms with the largest phases in V_{ub} and V_{td}.

Although the standard parameterization is exact, it is somewhat cumbersome and does not provide an obvious relationship between the various elements. The Wolfenstein parameterization [12] is an approximation which captures several of the most salient features of the $V_{\rm CKM}$ matrix — the hierarchical nature of the magnitudes and the relationship of those with large phases:

$$V_{\rm CKM} = \begin{pmatrix} 1 - \frac{1}{2}\lambda^2 & \lambda & A\lambda^3(\rho - i\eta) \\ -\lambda & 1 - \frac{1}{2}\lambda^2 & A\lambda^2 \\ A\lambda^3(1 - \rho - i\eta) & A\lambda^2 & 1 \end{pmatrix} + \mathcal{O}(\lambda^4) \tag{2.5}$$

In this approximation $\lambda = \sin\theta_C \approx 0.22$ and A, ρ, and η are all $\mathcal{O}(1)$. The phase information is contained in the parameters ρ and η in the V_{ub} and V_{td} terms.

2.3 The Unitarity Triangle

Many of the important magnitudes and phases of $V_{\rm CKM}$ are related by the unitarity condition

$$V_{ud}V_{ub}^* + V_{cd}V_{cb}^* + V_{td}V_{tb}^* = 0. \tag{2.6}$$

Dividing by $V_{cd}V_{cb}^*$ and treating each term as a vector in the complex plane yields the unitarity triangle shown in figure 2.1. In the $V_{\rm CKM}$ approximation of equation 2.5 the apex is (ρ, η) and $V_{td} \sim e^{-i\beta}$ and $V_{ub} \sim e^{-i\gamma}$. Many B physics measurements may be directly related to aspects of this triangle. *E.g.*, CP violation in $B^0 \to J/\psi K_S^0$ is proportional to $\sin(2\beta)$ while $B_s \to D_s^{\mp}K^{\pm}$ may be used to measure $\sin\gamma$. The rate of $B^0 \leftrightarrow \bar{B}^0$ mixing is proportional to the magnitude of V_{td} which is the least well known component of the right hand side of the triangle. Thus the unitarity triangle provides a simple framework for relating the consistency within the Standard Model of numerous $V_{\rm CKM}$ related measurements.

[4] Adjusting the sixth quark phase would be equivalent to an overall phase adjustment to the entire matrix which would have no observable effect.

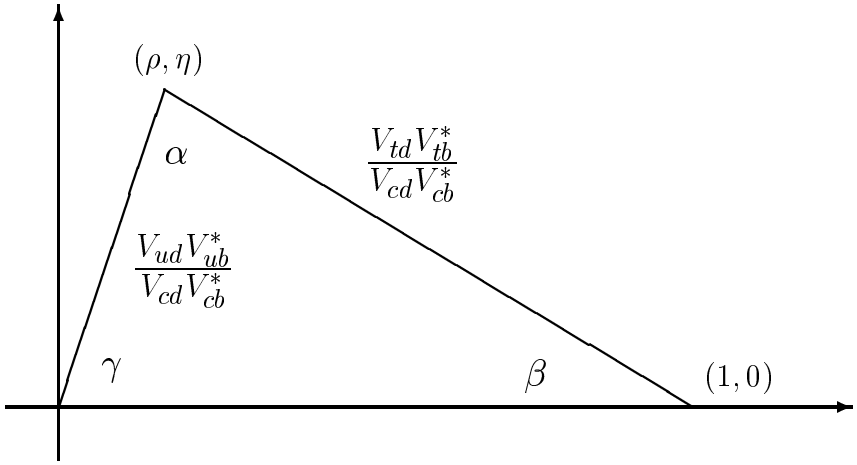

Figure 2.1: The unitarity triangle

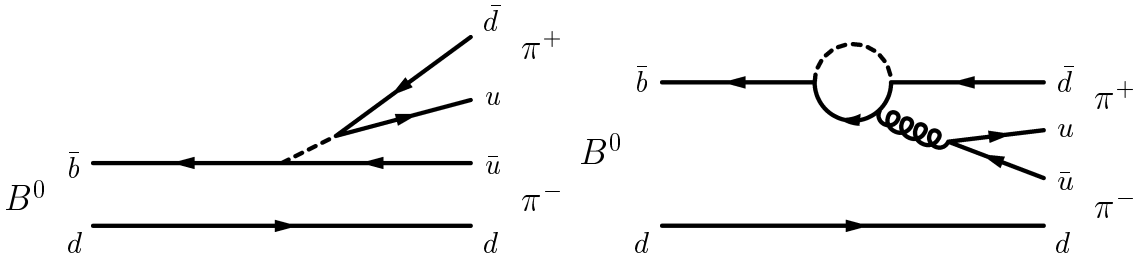

Figure 2.2: $B^0 \to \pi^+\pi^-$ Feynman diagrams

2.4 Standard Model CP Violation

CP violation arises within the Standard Model due to the single complex phase in $V_{\rm CKM}$. Applying CP to the charged current interaction of the electroweak Lagrangian

$$\mathcal{L}_{Wq} = \frac{g}{2\sqrt{2}} \left[\bar{u}_i \gamma^\mu W_\mu^+ (1-\gamma_5) V_{ij} d_j + V_{ij}^* \bar{d}_j \gamma^\mu W_\mu^- (1-\gamma_5) u_i \right] \tag{2.7}$$

effectively interchanges the left and right terms except for V_{ij} and V_{ij}^*. Thus if V contains a non-zero phase, $V \neq V^*$ and $\mathcal{L}_{Wq}$ is not CP invariant.

CP violation with neutral mesons manifests itself in three ways [23]:

- *Direct CP violation* in which the decay amplitude of a process is not equal to that of the CP conjugate process. This situation arises when several decay amplitudes and phases contribute to the same final state, *e.g.*, the two $B^0 \to \pi^+\pi^-$ Feynman diagrams of figure 2.2. If two or more contributions each have different weak phases (ϕ_k) and strong phases (δ_k) such that

$$A_f = \sum_k A_k e^{i(\delta_k + \phi_k)}, \qquad \bar{A}_{\bar{f}} = \sum_k A_k e^{i(\delta_k - \phi_k)}, \tag{2.8}$$

then

$$|A_f| \neq |\bar{A}_{\bar{f}}| \tag{2.9}$$

since

$$\left|\sum_k A_k e^{i(\delta_k+\phi_k)}\right| \neq \left|\sum_k A_k e^{i(\delta_k-\phi_k)}\right| \tag{2.10}$$

Direct CP violation has been observed in $K^0_{L,S} \to \pi\pi$ decays[5]. The strong phases in direct CP violation arise from long distance strong interactions and are difficult to calculate. The associated uncertainties limit the usefulness of direct CP violation for testing the Standard Model.

- *Indirect CP violation* in which the two neutral mass eigenstates are not the CP eigenstates. This has been observed in neutral kaons in the fact that K^0_L can decay to both $\pi\pi$ (CP-even) and $\pi\pi\pi$ (CP-odd). Defining the mass eigenstates as

$$|K^0_S\rangle = p|K^0\rangle + q|\bar{K}^0\rangle \tag{2.11}$$
$$|K^0_L\rangle = p|K^0\rangle - q|\bar{K}^0\rangle, \tag{2.12}$$

the condition $|q/p| \neq 1$ indicates indirect CP violation. This has been measured in neutral kaons [11] as

$$\delta(\ell) = \frac{\Gamma(K^0_L \to \pi^-\ell^+\nu_\ell) - \Gamma(K^0_L \to \pi^+\ell^-\bar{\nu}_\ell)}{\Gamma(K^0_L \to \pi^-\ell^+\nu_\ell) + \Gamma(K^0_L \to \pi^+\ell^-\bar{\nu}_\ell)} \tag{2.13}$$
$$= \frac{1-|q/p|^2}{1+|q/p|^2} \tag{2.14}$$
$$\delta(\mu) = (3.04 \pm 0.25) \times 10^{-3} \tag{2.15}$$
$$\delta(e) = (3.33 \pm 0.14) \times 10^{-3}. \tag{2.16}$$

Calculations of indirect CP violation also involve large hadronic uncertainties and thus any measurements are difficult to relate to fundamental CKM quantities.

- *CP violation due to interference between mixed and unmixed decays*: Neutral B, K, and D mesons can oscillate between their particle and anti-particle states due to flavor changing weak interactions such as the "box" diagram for $B^0 \leftrightarrow \bar{B}^0$ mixing shown in figure 2.3. When both states can decay to the same final state there is the possibility of a CP violating interference arising from different weak phases between the mixed and unmixed paths of decay. *E.g.*, both B^0 and $\bar{B}^0$ can decay to $J/\psi K^0_S$ with weak phases which are approximately zero. $B^0 \leftrightarrow \bar{B}^0$ mixing, however, introduces a weak phase of $\sim -2\beta$:

[5]Since all three types of CP violation contribute to $K^0_{L,S} \to \pi\pi$, the formalism to separate the direct contribution from the rest is not straightforward. For a pedagogical explanation, see reference [23].

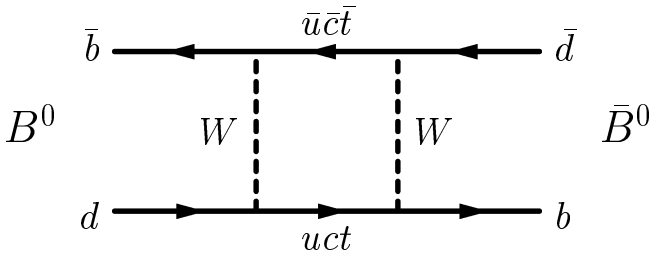

Figure 2.3: Box diagram for $B^0 \leftrightarrow \bar{B}^0$ mixing. Another diagram in which the internal W and uct quarks are exchanged contributes equally.

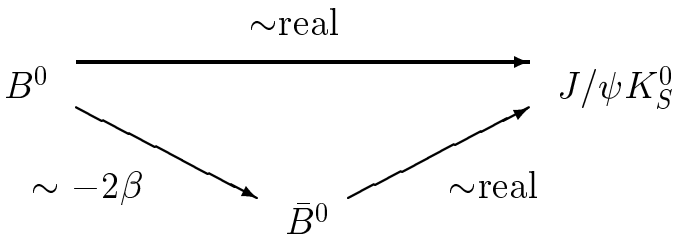

This leads to CP violation in the time dependent decay rates of B^0 and $\bar{B}^0$ which is proportional to $\sin(2\beta)$. This form of CP violation leads to the theoretically cleanest predictions and is generally the most useful form of CP violation for testing Standard Model predictions.

A given decay mode could have contributions from each of these three types of CP violation. The most useful decay modes for testing the Standard Model are those which have CP violation due to the interference between mixed and unmixed decays, but little or no direct or indirect CP violation since those contributions are difficult to calculate.

CP violation with kaons is a relatively small phenomena which has been observed primarily because of the copious number of kaons which have been produced and studied and the large lifetime difference between the mass eigenstates K_L^0 and K_S^0 which allows unambiguous separation of the two states. The Standard Model predicts much larger CP violation with B mesons but only recently have enough B mesons been produced to be able to begin to study these effects.

2.5 Baryogenesis

A common motivation for studying CP violation is the observed baryon/anti-baryon asymmetry in the universe. If the universe began with equal amounts of matter and anti-matter, there are three requirements for baryogenesis (the creation of a stable baryon/anti-baryon asymmetry) [13]:

- There must have been a time of non-thermal equilibrium.
- There must be baryon number violating processes.
- There must be CP violation, otherwise the CP conjugate baryon number violating processes would proceed at the same rate and no large asymmetry would result.

Most cosmological models of baryogenesis require much larger amounts of CP violation than are predicted with the $V_{\rm CKM}$ mechanism of the Standard Model [14], thus it is likely that the Standard Model explanation of CP violation is at best incomplete. The energy scales at which additional CP violation is necessary is still a subject of active debate and only some models require additional CP violation at energies accessible to current experiments. A detailed understanding of Standard Model CP violation and a search for additional non-Standard Model CP violation may provide useful input to current baryogenesis theories. Reference [15] provides a review of various models and their implications for CP violation and baryogenesis.

2.6 Non-Standard Model Effects

Non-Standard Model theories usually include additional couplings which in general have CP violating phases. *E.g.*, the minimal supersymmetric extension to the Standard Model (MSSM) introduces 43 new CP violating phases[6][17]. It is possible to tune the theory to have nearly the same predictions as the Standard Model, but in general these new phases lead to different CP violation predictions than those of the Standard Model. Reference [23] provides a pedagogical overview of the effects of several non-Standard Model theories on B physics; reference [24] considers the case of supersymmetric effects upon B physics in greater detail.

Since all Standard Model CP violation is tied to a single parameter (the phase in the $V_{\rm CKM}$ matrix), consistency tests between numerous manifestations of CP violation are sensitive tests of the Standard Model. *E.g.*, the decay $B^0 \to J/\psi K^0_S$ has CP violation proportional to $\sin(2\beta)$. New physics (*i.e.*, non-Standard Model) phases would generally enter via the box diagram of B^0 mixing but not in the tree diagram of the $B^0 \to J/\psi K^0_S$ decay. $B^0 \to \phi K^0_S$ (shown in figure 2.4) is another decay which within the Standard Model has CP violation proportional to $\sin(2\beta)$ due to the weak phases in B^0 mixing. In this case, however, new physics phases would contribute to both the box diagram of B^0 mixing and the loop diagram of the $B^0 \to \phi K^0_S$ decay, producing an observed CP violating phase different from that of $B^0 \to J/\psi K^0_S$. The Standard Model predicts these phases to be the same with a theoretical uncertainty

[6]Most of those phases are due to including the most general form of supersymmetry breaking. If the specific mechanism of supersymmetry breaking were known, the number of phases would be considerably reduced, but supersymmetric theories would still include non-Standard Model CP violating phases.

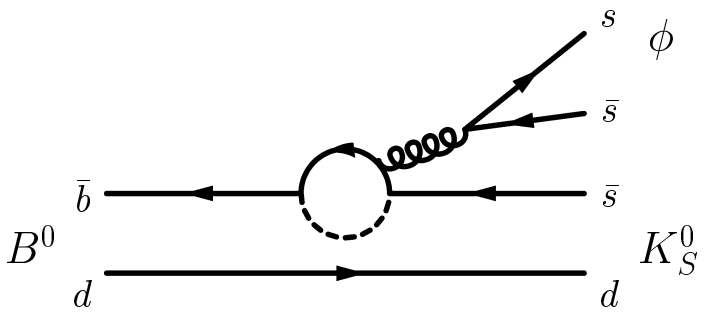

Figure 2.4: Feynman diagram for $B^0 \to \phi K^0_S$. Within the Standard Model this decay has CP violation proportional to $\sin(2\beta)$.

of less than 5%; new physics models generally predict different CP violating phases for these two decays. Thus measurements such as these are sensitive tests of the Standard Model *vs.* new physics models.

Additionally, new physics models usually include new particles which could participate in loops diagrams for processes such as $B^0 \to K^{*0}\gamma$ and $B^0 \leftrightarrow \bar{B}^0$ mixing. These additional particle contributions could increase the rate of these processes such that they would be inconsistent with Standard Model predictions. *E.g.*, CLEO's measurement of $\mathrm{BR}(B^0 \to K^{*0}\gamma) = (4.55^{+0.72}_{-0.68} \pm 0.34) \times 10^{-5}$ [16] provides one of the most stringent indirect constraints of supersymmetric models.

2.7 B_s Decays

The study of B_s decays forms an important compliment to the CKM related measurements possible with B^0 decays. In some cases, the ratios of B_s to B^0 measurements cancel theoretical uncertainties. In other cases, results from B_s modes could provide unambiguous evidence for new physics in a manner which is not possible with B^0 measurements.

2.7.1 B_s Mixing

As mentioned in section 2.3, the rate of $B^0 \leftrightarrow \bar{B}^0$ mixing Δm_d is proportional to the magnitude of V_{td} which is the least well known component of the right hand side of the unitarity triangle.

Unfortunately the extraction of V_{td} from Δm_d involves a number of theoretical uncertainties. Specifically, the mixing matrix element $\mathcal{M}$ is proportional to

$$\mathcal{M} \propto m_B f_B^2 B_B \eta_B V_{td} \tag{2.17}$$

where the various prefactors are

- m_B: the B_s or B^0 mass, both of which have less than 0.1% uncertainty.
- $f_B = 200 \pm 16$ MeV: the B decay constant.
- $B_B = 1.37 \pm 0.08$: the "Bag Parameter" which arises in the calculation of the matrix element

$$\begin{aligned} \langle B|(\bar{d}\gamma^\mu(1-\gamma_5)b)^2|\bar{B}\rangle &= \sum_n \langle B|\bar{d}\gamma^\mu(1-\gamma_5)b|n\rangle\langle n|\bar{d}\gamma^\mu(1-\gamma_5)b|\bar{B}\rangle & (2.18) \\ &\equiv B_B\langle B|\bar{d}\gamma^\mu(1-\gamma_5)b|0\rangle\langle 0|\bar{d}\gamma^\mu(1-\gamma_5)b|\bar{B}\rangle & (2.19) \\ &= B_B|\langle 0|(\bar{d}\gamma^\mu\gamma_5 b)^2|B\rangle|^2 & (2.20) \end{aligned}$$

  The bag parameter B_B absorbs the correction for the insertion of the vacuum $|0\rangle\langle 0|$ in place of the sum over all intermediate states n.
- $\eta_B = 0.55 \pm 0.01$ is a QCD correction factor for the effect of gluon exchanges in the B mixing diagrams.

The values and uncertainties for these terms are taken from the recent review [18].

Measuring the ratio of the B_s mixing parameter Δm_s and the B^0 mixing parameter Δm_d cancels many of the uncertainties:

$$\frac{\Delta m_s}{\Delta m_d} = \frac{m_{B_s} f_{B_s}^2 B_{B_s}}{m_{B_d} f_{B_d}^2 B_{B_d}} \left|\frac{V_{ts}}{V_{td}}\right|^2 \tag{2.21}$$

Although the uncertainty on $f_B^2 B_B$ is $\mathcal{O}(10\%)$, the uncertainty on the ratio between these parameters for the B_s and the B^0 is $\mathcal{O}(1\%)$ [18]. Thus the inclusion of B_s mixing information provides a much cleaner measurement of the $V_{\rm CKM}$ elements than the B^0 mixing result does alone.

2.7.2 CP Violation in B_s Decays

The $B^0 \leftrightarrow \bar{B}^0$ mixing diagram of figure 2.3 involves $V_{\rm CKM}$ terms of $V_{tb}^* V_{td}/V_{tb}V_{td}^*$. Since $V_{td} \sim e^{-i\beta}$, these terms involve a phase of -2β. Thus any B^0 decay to a CP eigenstate will have a CP violating phase from the box mixing diagram unless additional decay phases exactly cancel the mixing phase (no such cases are expected). Thus from a single measurement one cannot immediately disentangle a Standard Model contribution from a potential new physics phase contribution.

$B_s \leftrightarrow \bar{B}_s$ mixing replaces the d quark of figure 2.3 with an s quark, thus V_{td} is replaced with V_{ts}. Since V_{ts} (and all the other $V_{\rm CKM}$ elements of the mixing diagram) are approximately real in the Standard Model, B_s mixing does not introduce a significant phase to B_s decays to CP eigenstates. In the dominant $b \to c(\bar{c}s)$ decays, the CKM elements are V_{cb} and V_{cs}, both of which are also approximately real. Thus the Standard Model predicts only very small CP violation in the dominant B_s decay modes.

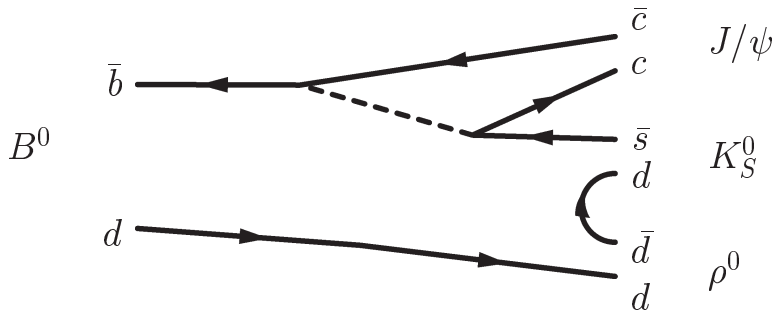

Figure 2.5: Feynman diagram for the quark popping decay mode $B^0 \to J/\psi K^0_S \rho^0$

The advantage of this situation is that any observation of large CP violation in $b \to c(\bar{c}s)$ decays of B_s mesons is evidence for non-Standard Model phase contributions, likely to the mixing diagram. In contrast, in B^0 decays large CP violation could be formed by a Standard Model contribution plus a non-Standard Model phase yet this would not be clear until several separate measurements of β had been made.

2.8 $B \to J/\psi X$ Decays

$B \to J/\psi X$ decays have been useful for a variety of B physics measurements including $\sin(2\beta)$ with $B^0 \to J/\psi K^0_S$ [19]; polarization with $B_s \to J/\psi\phi$ [20] and $B^0 \to J/\psi K^{*0}$ [20, 21]; and B masses and lifetimes with several $B \to J/\psi X$ decays [11]. In Run II CDF intends to use $B_s \to J/\psi\phi$ angular correlations to measure the lifetime difference between CP-even and -odd components of the B_s and search for non-Standard Model CP violation [22]. Belle and BaBar intend to use $B^0 \to J/\psi(K^{*0} \to K^0_S\pi^0)$ to measure $\sin(2\beta)$ and possibly $\cos(2\beta)$ as well [23]. These modes benefit from the $J/\psi \to \mu^+\mu^-$ decay which provides a convenient trigger which is especially important at a hadronic accelerator where the backgrounds are quite large.

The inclusive branching ratio for $B \to J/\psi X$ is $(1.16 \pm 0.10)\%$ [11], yet the branching ratios of the known exclusively reconstructed $B \to J/\psi X$ decays sum to only a small fraction of this. Typically the submodes have branching ratios $\mathcal{O}(10^{-3})$ and only a few are known [11]. This analysis explores a new class of $B \to J/\psi X$ decays which could account for many of the missing decay modes.

2.8.1 Quark Popping Decays

One possibility for $B \to J/\psi X$ decays is a class of decays which involve "quark popping" of an additional quark pair in addition to a $b \to c(\bar{c}s)$ decay. A Feynman diagram of one such decay ($B^0 \to J/\psi K^0_S \rho^0$) is shown in figure 2.5. CLEO recently

reported $B \to J/\psi\phi K$ [30] which is a similar decay which involves an $s\bar{s}$ pair. There are many possibilities for such decays depending on which quark pair is involved and whether the mesons hadronize into a scalar or vector state (*e.g.*, K^0 *vs.* K^{*0}). Some of the possibilities are listed in table 2.1.

	$B^+ \to J/\psi +$	$B^0 \to J/\psi +$	$B_s \to J/\psi +$
$u\bar{u}$	$(K^+\pi^0)$	$K^+\pi^-$	K^+K^-
	$(K^{*+}\pi^0)$	$K^{*+}\pi^-$	$K^{*+}K^-$
	$K^+\rho^0$	$(K^+\rho^-)$	K^+K^{*-}
	$K^{*+}\rho^0$	$(K^{*+}\rho^-)$	$K^{*+}K^{*-}$
dd	$K^0\pi^+$	$(K^0\pi^0)$	$K^0\bar{K}^0$
	$K^{*0}\pi^+$	$(K^{*0}\pi^0)$	$K^{*0}\bar{K}^0$
	$(K^0\rho^+)$	$K^0\rho^0$	$K^0\bar{K}^{*0}$
	$(K^{*0}\rho^+)$	$K^{*0}\rho^0$	$K^{*0}\bar{K}^{*0}$
$s\bar{s}$	ϕK^+	ϕK^0	$\phi\phi$
	ϕK^{*+}	ϕK^{*0}	

Table 2.1: Possible quark popping decays of the form $b \to c(\bar{c}s) + q\bar{q}$. Modes in parentheses have neutral final state particles which would be difficult to observe at CDF.

Some of the modes of table 2.1 are dominated by well established resonances such as $B_s \to J/\psi K^+K^-$ which is primarily $B_s \to J/\psi(\phi \to K^+K^-)$. Some of the other modes, however, have never been observed. We report here a study of $B^0 \to J/\psi K^0\pi^+\pi^-$ (with contributions from $B^0 \to J/\psi K^0\rho^0$ and $B^0 \to J/\psi K^{*+}\pi^-$); $B^0 \to J/\psi K^{*0}\pi^+\pi^-$ (with a possible contribution from $B^0 \to J/\psi K^{*0}\rho^0$); and $B_s \to J/\psi K^0\pi^\pm K^\mp$ (with possible contributions from $B_s \to J/\psi K^0\bar{K}^{*0}$, $B_s \to J/\psi\bar{K}^0K^{*0}$, and $B_s \to J/\psi K^{*\pm}K^\mp$).

As a brief example of the potential usefulness of these modes, we note that the final state $J/\psi K^0_S\rho^0$ is accessible from both B^0 and $\bar{B}^0$. This situation allows the possibility of CP violation due to the interference between mixed and unmixed decays. The final state is not a CP eigenstate so an angular analysis would be necessary to extract the CP-even *vs.* -odd amplitudes. If the factorization hypothesis is valid, the interference between CP-even and -odd terms in the angular distributions of the final state particles can be used to extract a value for $\cos(2\beta)$. Even the sign of $\cos(2\beta)$ would be useful for resolving two of the four trigonometric discreet ambiguities on β which arise from a $\sin(2\beta)$ measurement.

2.8.2 Standard Model Quark Popping Predictions

The QCD aspects of the creation of an extra quark pair internal to the Feynman diagram make specific branching ratio predictions for these modes difficult. A few

trends may be noted: After a B decays to a J/ψ and a K, there is $\sim$ 1.7 GeV of remaining energy which is easily sufficient for the creation of a quark pair. $u\bar{u}$ and $d\bar{d}$ pairs should be somewhat more common than $s\bar{s}$ pairs due to their lighter masses, but in comparision to the 1.7 GeV of energy available the $s\bar{s}$ supression should not be large. Finally, the quark popping modes should have branching ratios lower than BR($B \to J/\psi K$) which is $\mathcal{O}(10^{-3})$. CLEO has measured BR($B \to J/\psi \phi K$) = $(8.8^{+3.5}_{-3.0} \pm 1.3) \times 10^{-5}$ which involves an $s\bar{s}$ pair, so expected branching ratios for the $u\bar{u}$ and $d\bar{d}$ quark popping modes studied here are in the range 10^{-4} to 10^{-3}.

Chapter 3

Experimental Apparatus

This analysis studies the decay of B mesons which are created in $p\bar{p}$ collisions produced by the Tevatron accelerator at Fermilab. Upon production, the B mesons decay rapidly and their decay products are observed using the Collider Detector at Fermilab (CDF). This chapter provides an overview of the Tevatron and the portions of the CDF detector[1] which are used in this analysis.

3.1 The $p\bar{p}$ Accelerators

The Tevatron is the accelerator at Fermilab which produces the $p\bar{p}$ collisions which create the B mesons used in this study. In comparison to e^+e^- "B factories", the Tevatron has the advantage of a huge b-quark production cross section at its center of mass collision energy of $\sqrt{s} = 1.8$ TeV: $\sigma(p\bar{p} \to b\bar{b}) \approx \mathcal{O}(10\ \mu\text{b})$ within the CDF detector acceptance in comparison to $\sigma(e^+e^- \to b\bar{b}) \approx \mathcal{O}(1\ \text{nb})$ at the $\Upsilon(4S)$ resonance. An additional advantage is that the Tevatron can produce all forms of B mesons and hadrons instead of just B^0 and $B^\pm$ produced at the B factories. The disadvantage of the Tevatron is that the backgrounds from generic QCD interactions are much larger than the backgrounds at e^+e^- colliders.

Proton acceleration proceeds in several stages. It begins with H^- ions produced in an electric discharge in a hydrogen gas bottle. These ions are accelerated 150 m to an energy of 400 MeV where they are passed through a carbon foil which strips off the electrons, leaving protons which are injected into a 75 m radius Booster Ring and accelerated to 8 GeV. From the Booster Ring the protons are injected into the 1 km radius Main Ring which further accelerates the protons to 150 GeV in bunches of $\sim 2 \times 10^{11}$ protons each.

To create anti-protons, proton bunches from the Main Ring are removed and collided with a tungsten foil target which produces a spray of particles which include

[1] Colloquially, "CDF" has come to refer to the collaboration rather than the detector itself, thus the apparently redundant phrase "CDF detector" is common.

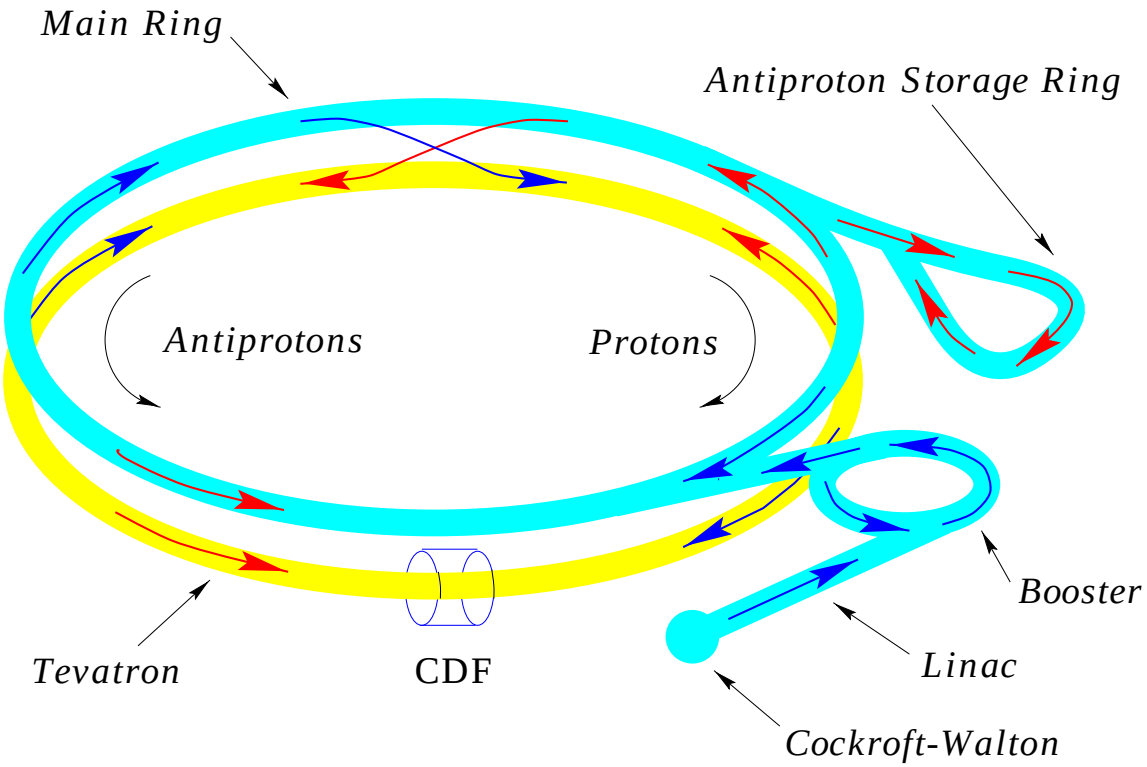

Figure 3.1: Diagram of the Fermilab $p\bar{p}$ accelerators

anti-protons. Approximately 1 out of every 10^5 protons produces an anti-proton. These anti-protons are collected at a rate of $\sim 4 \times 10^{10}$ per hour and are used to create anti-proton bunches in the main ring with $\sim 5 \times 10^{10}$ anti-protons per bunch.

The Tevatron performs the final acceleration of the protons and anti-protons in counter rotating bunches. After reaching 900 GeV the proton and anti-proton bunches are focused into narrow beams and passed through each other, producing $p\bar{p}$ collisions every 3.5 μs. Since each bunch contains 2×10^{11} protons (or 5×10^{10} anti-protons) multiple interactions can occur in a single crossing. There are an average of 2.7 $p\bar{p}$ interactions per crossing with a Gaussian shaped distribution along z with $\sigma = 30$ cm. Approximately 85% of the events have the primary interaction separated by more than 5 cm from the other interactions such that the tracks from the primary interaction can be distinguished from the others. Thus the dominant effect of multiple interactions is to increase the occupancy in the tracking chambers which slightly degrades the tracking performance as will be described in section 3.2.2. Events which have interactions within 5 cm of each other in z have higher backgrounds due to the combinatorics of additional tracks with which to form B candidates.

Many B physics analyses use the flight distance between the points of production and decay of the B, thus the exact position of the $p\bar{p}$ collision is important. During the course of Run I the actual beam intersection point varied by up to 3 mm radially from the nominal beam position about which the CDF detector is centered. This position can be determined offline for each data taking run[2] and used to adjust the coordinate system origin for tracking parameters. Of more importance is the radial beam profile which imparts an uncertainty on the location of the B production. The beam profile is approximately azimuthally symmetric about the beam axis with an RMS of 25 μm (35 μm at the start of Run I). This spread is similar in size to the uncertainty on the vertex position of a typical exclusively reconstructed B decay as measured by the CDF Silicon Vertex Detector.

This study uses 110 pb^{-1} of data taken during Run I of the Tevatron which lasted from 1992 to 1995. Approximately 20% of the data were taken during Run Ia between August 1992 and May 1993 during which the Tevatron luminosity averaged 5×10^{30} cm^{-2} s^{-1}; the majority of the data was taken during Run Ib between January 1994 and July 1995 when the Tevatron luminosity averaged 1.6×10^{31} cm^{-2} s^{-1} with a peak luminosity of 2.8×10^{31} cm^{-2} s^{-1}.

3.2 The Collider Detector at Fermilab

The CDF detector has been described in detail elsewhere [26, 27, 28, 29]. This section describes the portions of the detector which are most relevant for this analysis.

[2] "run" with a lower case "r" refers to an experimental data taking period typically lasting several hours; "Run I" with a capital "R" refers to the 3 year operation of the Tevatron between 1992 and 1995 during which many "runs" occurred.

Figure 3.2: Quarterview rz cross section of the CDF detector.

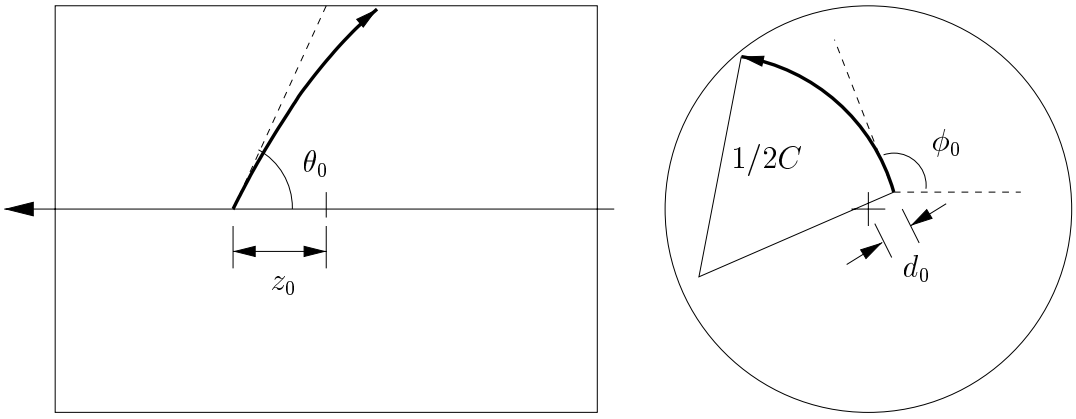

Figure 3.3: Diagram of the tracking parameters from a sideview and endview of the CTC.

Figure 3.2 shows an rz cross section of one quarter of the CDF detector; the other quarters are symmetric with the quarter shown. The z direction of the CDF coordinate system is along the proton direction of the beam and is defined by the cylindrical axis of the Central Tracking Chamber which is centered about the nominal beam position. The x direction is radially outward from the Tevatron ring and y is straight up. The azimuthal angle ϕ is measured from the x axis moving toward the y axis; the polar angle θ is measured with respect to the z axis.

Closest to the interaction point, the Silicon Vertex Detector (SVX) provides precise vertex information about the decay products which is used to determine the lifetime of the B candidates. The Vertex Tracking Chamber is a time projection chamber which surrounds the SVX and provides information to locate the z position of charged particle tracks. The Central Tracking Chamber (CTC) is an open cell gas filled tracking chamber used to measure the position and momentum of charged particle tracks. A 1.4 Tesla solenoid provides the magnetic field in which the charged particle trajectories bend which provides the ability to make a momentum measurement from the track curvature. The calorimeters located around the CTC are not used in this analysis other than to act as an absorber for particles. The muon chambers are located on the outside of the detector and are used to identify muon candidates which penetrate the calorimeters.

A charged particle track in a magnetic field follows a helical trajectory which can be described by 5 parameters as shown in figure 3.3:

- d_0: The radial distance of closest approach to the beam line.
- z_0: The z position at the point of closest approach.

- ϕ_0: The ϕ direction at the point of closest approach.

- C: The track curvature (the inverse of the diameter of the rz circle which the track follows).

- $\cot\theta_0$: The cotangent of the polar angle with respect to the beam line.

These parameters are measured by the Central Tracking Chamber. The Silicon Vertex Detector provides additional $r\phi$ position information to improve the d_0 and C resolution. The Vertex Tracking Chamber information is used in combination with the Central Tracking Chamber to find the z_0 location of particle tracks. Physics analyses frequently use the physically more pertinent quantities of the transverse momentum $p_T \propto 1/C$ and the pseudo-rapidity $\eta = -\ln\tan(\theta_0/2)$ since many physics distributions are approximately uniform in η.

3.2.1 Silicon Vertex Detector

The primary purpose of the Silicon Vertex Detector (SVX) is to make a precise measurement of the impact parameter d_0 of tracks. This information is crucial when combining tracks together to form decay vertices to distinguish particles with lifetime such as B^0 from the backgrounds which are produced at the primary vertex.

The SVX is based upon layers of silicon strip detectors. The strips are p-doped silicon in a lightly n-doped bulk substrate with a strongly n-doped layer applied on the opposite side for a total thickness of 300 μm. A positive bias voltage up to 80 volts is applied to the n-doped side, creating an electric field in the n-doped substrate and depleting the free electrons in it. As charged particles pass through the bulk silicon they ionize the silicon forming $\sim 30,000$ electron and hole pairs. The holes move in the electric field to the p-doped strips where they are read out using an integrated circuit attached at the end of the strip.

The strips have a pitch of 60 μm (55 μm for the outermost layer) and a typical track deposits charge across several strips. Combining the weighted charge information across several strips provides a 10 μm hit resolution. The strips are parallel to the beam and thus provide only $r\phi$ information.

The impact parameter resolution is measured to be $(13 \oplus 40/p_T)$ μm where p_T is measured in GeV/c. The limiting resolution of 13 μm is due approximately equally to a combination of alignment uncertainties and fundamental limitations of the SVX geometry (*e.g.* the number of layers, strip pitch, etc.). The resolution degradation at low p_T is due to multiple scattering of particles as they pass through the silicon. The impact parameter resolution is additionally convoluted with the ~ 25 μm RMS of the beam spot. When several tracks are combined into a vertex fit the typical resolution on the decay length of a B^0 is ~ 30 μm in comparison to the $c\tau = 464$ μm lifetime of the B^0.

Physically the SVX is comprised of two barrels arranged in twelve wedges with each wedge containing four layers of silicon strip detectors located from 3 to 8 cm radially from the beam. Each layer is formed by three 8.5 cm silicon wafers wirebonded into a 25.5 cm ladder. There is a 2.15 cm gap between the two barrels at $z = 0$. The total active length of 51 cm covers approximately 60% of the interaction region which is Gaussian shaped with $\sigma \approx 30$ cm. This lack of coverage is a major limitation of the SVX detector.

The geometry of an SVX barrel and one of its ladders is shown in figure 3.4. The material in the SVX was kept as low as possible in order to minimize conversions which cause background and multiple scattering which degrades the tracking resolution. Most radial tracks pass through 3% of a radiation length in the SVX.

Due to radiation damage, the SVX which was present in Run Ia was replaced with a very similar silicon tracking system (SVX′) with radiation hard technology for Run Ib. A comparison of the detectors is listed in table 3.1.

3.2.2 Central Tracking Chamber

While the SVX measures only a few tracking parameters (d_0 and ϕ), the Central Tracking Chamber (CTC) measures all of the track parameters. When possible, the information from both trackers is combined to form a global track fit.

Charged particles' momenta are determined from the curvature of their ionization tracks as they pass through the magnetic field in the Central Tracking Chamber. As charged particles pass through the CTC, they ionize the gas and the electrons drift toward the sense wires. As they approach the sense wires, the electric field becomes much stronger due to the $1/r$ potential and the accelerating electrons create an avalanche of other electrons from atoms in the gas. This avalanche of electrons provides the gain to make the ionization signal large enough to detect.

The electrons drift in a trajectory determined by the $\vec{E} \times \vec{B}$ of the electric and magnetic fields. The cells are arranged such that the electrons drift perpendicular to the sense wire plane in order to give the best resolution on the tracks. This produces the tilted cell geometry shown in figure 3.5. A high momentum track traveling radially passes through a maximum of 84 cells which provide the measurements for determining the track's curvature and thus momentum.

The cells are arranged into two kinds of superlayers: five axial superlayers have wires parallel to the beam and measure the track position in $r\phi$ while four stereo superlayers have wires tilted at a $\pm 3^\circ$ angle which introduces a z dependence to the $r\phi$ measurement. When combined with the axial layers, the stereo layers provide information to measure the z_0 and $\cot\theta_0$ of tracks. The z location of the primary vertex as determined by the Vertex Tracking Chamber is used as an input to the tracking algorithm to aid in the determination of z and $\cot\theta$. The CTC momentum resolution is $\delta p_T/p_T^2 \leq 0.002$ if a beam constraint is not required[3]. The CTC z

[3] Constraining particles in the track parameter fit to come from the interaction point improves the

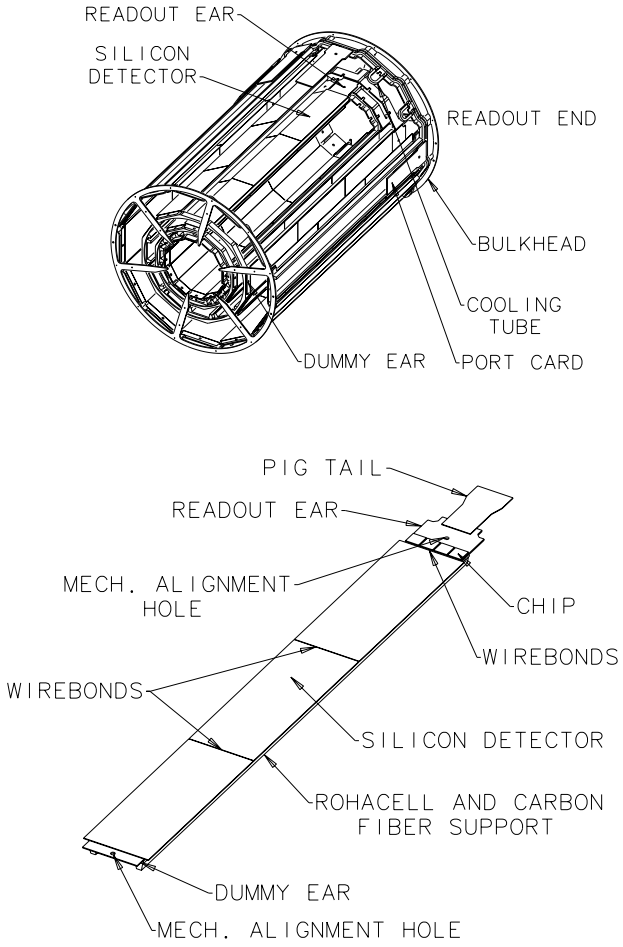

Figure 3.4: An isometric view of an SVX barrel (upper) with some of the ladders removed and one of the ladders (lower).

Feature	SVX	SVX′
Channels	46080	46080
z coverage	51.1 cm	51.1 cm
Gap at z=0	2.15 cm	2.15 cm
Radius of layer 0	3.0049 cm	2.8612 cm
Radius of layer 1	4.2560 cm	4.2560 cm
Radius of layer 2	5.6872 cm	5.6872 cm
Radius of layer 3	7.8658 cm	7.8658 cm
Overlap of layer 0	-1.26deg	0.17deg
Overlap of layer 1	0.32deg	0.32deg
Overlap of layer 2	0.30deg	0.30deg
Overlap of layer 3	0.04deg	0.04deg
Silicon	one-sided	one-sided
Power	DC	AC, FOXFET bias
Passivation	none	polyimide
Atmosphere	Argon/Ethane+H_2O	Dry Nitrogen
Readout chip	SVX IC Rev. D	SVX IC Rev.H3
Sampling	quadruple	double
Noise	2200 electrons	1300 electrons
Gain	15 mV/fc	21 mV/fc
Reset/Integrate	3.5 μs	3.5 μs
Readout time	2.7 μs	2.1μs
Radiation Limit	15-20 KRad	$>$ 1 MRad
Bad channels	2.93%	1.73%
Typical Occupancy	7-10%	5%
Max Occupancy	12-20%	25%

Table 3.1: A comparison of the SVX and SVX′ detectors.

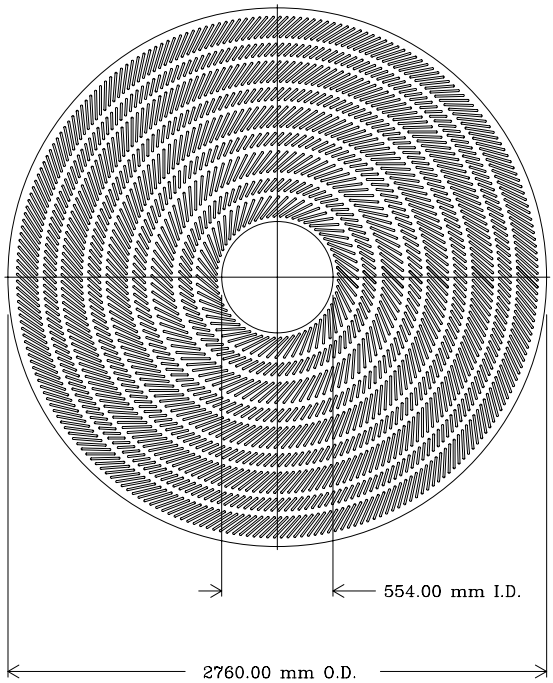

Figure 3.5: Diagram of the Central Tracking Chamber (CTC) endplate showing the location of the wire planes

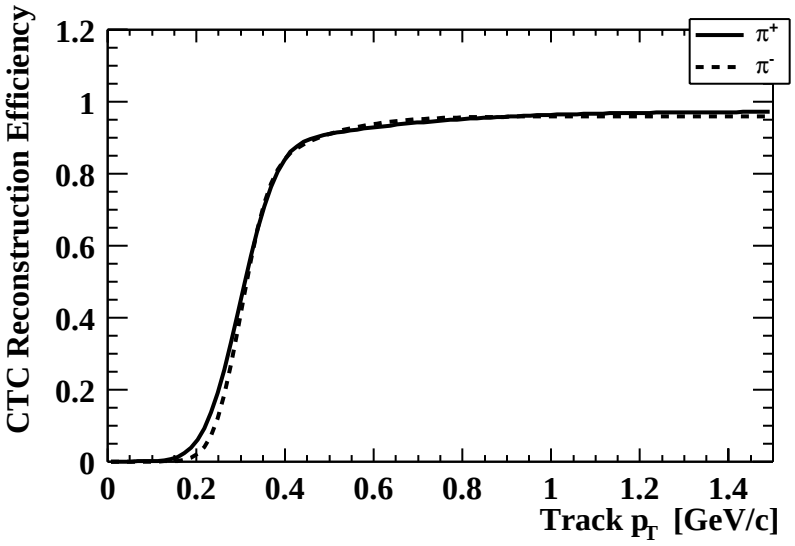

Figure 3.6: Parameterization of the CTC tracking efficiency for positive (solid curve) and negative (dashed curve) particles as a function of p_T, showing the p_T threshold for reconstruction.

resolution is 1 cm and is dominated by the $\cot\theta_0$ resolution of ~ 0.015. The ϕ resolution is better than 0.15 mrad.

After tracks are found in the CTC they are projected into the SVX to search for SVX clusters from the track. If 3 or 4 SVX layers have matching clusters a combined track fit is performed to take advantage of the accurate SVX impact parameter determination in conjunction with the other track parameters measured by the CTC. A combined fit with SVX information improves the momentum resolution to $\delta p_T/p_T^2 \leq 0.001$. These tracking parameter resolution improvements translate into improved physics quantity measurements. *E.g.*, the $J/\psi \rightarrow \mu^+\mu^-$ mass resolution improves from 22.5 MeV/c^2 to 16.6 MeV/c^2 by including SVX tracking information [27].

The average CTC tracking efficiency is shown in figure 3.6. The efficiency plateau is slightly less than 100% due to interference between the signals of overlapping tracks. This degradation is worse for high luminosity runs in which multiple interactions per beam crossing are more likely. The plateau value varies from 94% for the highest luminosity runs of Run Ib to 98% for the low luminosity runs of Run Ia. The p_T threshold for track reconstructability turns on between 200 and 400 MeV/c.

momentum resolution to $\delta p_T/p_T^2 \leq 0.001$, but this cannot be done for a B decay since the particle tracks of interest come from the B decay vertex which is separated from the primary interaction vertex.

3.2.3 Muon Detectors

Energy deposition of a charged particle in the electromagnetic calorimeter is due to bremstralung which is inversely proportional to the mass squared of the charged particle. Since muons are 200 times more massive than electrons they easily pass through the electromagnetic calorimeters. Since they do not interact hadronically they also pass through the hadronic calorimeters. The muon systems take advantage of this penetrating power of muons to identify them with scintillators and layers of drift tubes located outside of the calorimeters where few charged particles except muons are able to penetrate.

Two muon systems are located centrally covering $|\eta| < 0.6$, separated by a 60 cm layer of steel. Each muon system is comprised of four layers of rectangular drift tubes with a single sense wire aligned along the z direction. The first and third layers are offset in ϕ from the second and fourth. The ambiguity in which side of the sense wires a track passes is resolved by measuring which two sense wires receive the drift electrons first. The outer muon system additionally has a layer of scintillation counters. The momentum of a muon candidate is estimated by the angle at which it passes through the muon chambers.

An extension to the central muon systems is located in conical arches covering $0.6 < |\eta| < 1.0$ to complement the tracking coverage of the CTC. This extension is comprised of eight layers of drift tubes with scintillation counters on both sides.

The muon drift tubes have a spatial resolution of ~ 280 μm in the ϕ direction and 1.2 mm in z. This spatial resolution allows track "stubs" in the muon chambers to be matched to tracks in the CTC to identify them as muon candidates. The muon systems are nearly 100% efficient[4] for recording a muon stub for muons with transverse momentum above 3 GeV/c.

This analysis uses all muon systems described here for the $J/\psi \to \mu^+\mu^-$ trigger. For the final $J/\psi \to \mu^+\mu^-$ reconstruction, only muon candidates which pass through both of the central ($|\eta| < 0.6$) muon systems are used.

3.2.4 Decay Reconstruction Efficiency

The reconstruction efficiency for a given decay topology is dominated by the p_T acceptance of the Central Tracking Chamber. The more final state particles there are in a decay, the lower the probability will be that all of them will be above the minimum reconstructable p_T. While all final state particles must also be within $|\eta| < 1.0$ to be reconstructable, the differences in the η distributions between various decay modes is negligible and contributes less than 2% to the reconstruction efficiency differences between the various decay modes studied in this analysis.

[4] *N.B.* the muon triggers are only $\sim$ 90% efficient at finding a muon with $p_T > 3.0$ GeV/c, but the chambers themselves are nearly 100% efficient for recording a muon stub from muons with $p_T > 3.0$ GeV/c.

The difference in efficiencies due to lower p_T spectra for many-particle final states is dramatic: *e.g.* the six particle final state modes studied here typically have reconstruction efficiencies which are a factor of 5 lower than the similar four body final state decays of $B^0 \to J/\psi K^{*0}$ and $B^0 \to J/\psi K^0_S$. This difference is dominated by the p_T threshold (*i.e.*, the efficiency turn on curve shown in figure 3.6): if a decay has all final state particles within the p_T and η acceptance of the CTC, its reconstruction efficiency is similar to other decays within the acceptance.

Chapter 4

Analysis Method

The decay modes considered in this study are all similar, involving a J/ψ and a neutral kaon, thus the techniques used to search for and analyze these decays are also similar. This chapter describes the common elements of the analysis applied to each of the decay modes.

4.1 Use of a Reference Decay Mode

In order to determine a branching fraction from some number of observed B decays, one needs to know how many B mesons were produced (*i.e.* the integrated luminosity times the B meson production cross section) and the absolute efficiency for detecting them. Many of the uncertainties involved can be eliminated by measuring the ratio of branching ratios with some well established reference mode such as $B^0 \to J/\psi K^0_S$ or $B^0 \to J/\psi K^{*0}$. Both of these modes have hundreds of events in the CDF Run I data and their branching ratios are known to better than 15%. By measuring the ratio of branching ratios, the uncertainties on the luminosity and B production cross section completely cancel as do many of the effects which lead to a difference in reconstruction efficiencies. The remaining task of determining the ratio of reconstruction efficiencies between the signal and reference modes is simpler and involves less uncertainty than trying to determine these efficiencies absolutely.

Specifically,

$$\frac{N_{sig}}{N_{ref}} = \frac{\mathrm{BR}_{sig}}{\mathrm{BR}_{ref}} \cdot \frac{\epsilon_{sig}}{\epsilon_{ref}} \tag{4.1}$$

$$\mathrm{BR}_{sig} = \frac{N_{sig}}{N_{ref}} \cdot \frac{\epsilon_{ref}}{\epsilon_{sig}} \cdot \mathrm{BR}_{ref} \tag{4.2}$$

This method still requires a Monte Carlo simulation to model the ratio of the efficiencies but this procedure involves less uncertainty than trying to determine them absolutely. *E.g.*, if the Monte Carlo simulation has an incorrect $p_T(B)$ spectrum such that the signal efficiency is overestimated by 10%, the reference mode efficiency will

also be overestimated by approximately the same 10% and the effect mostly cancels rather than producing a 10% error in the measurement.

The Monte Carlo data were generated and decayed using the CLEO Monte Carlo package (QQ/Bgen). The CDF version of this program uses adjusted b-quark p_T and η distributions to match those found in hadronic $b\bar{b}$ production at the Tevatron. The CDF detector was simulated to create datasets which were then reconstructed using the same code as applied to the data. The resulting fitted numbers of events were used to estimate the relative decay reconstruction efficiencies between the signal and reference modes. Section 4.3 discusses the cuts whose efficiencies cancel in the ratio and how well the Monte Carlo models the efficiencies which do not exactly cancel. Section 4.4 describes corrections to the ratio of efficiencies to account for Monte Carlo mis-modeling of the tracking efficiency and the efficiency of the isolation cut (this cut will be described in section 4.2.4).

The detector simulation, known as QFL′,is a parametric simulation which models the reconstruction resolutions for various parts of the detector based upon measured resolution functions rather than trying to model the detector performance from fundamental physics interactions. *E.g.*, the position of a Monte Carlo particle track in the Central Tracking Chamber is smeared as a function of its p_T and η based upon measured resolutions rather than individually modeling its interactions with the gas and chamber material as it passes through. Silicon Vertex Detector clusters are individually modeled since the vertex resolution is sensitive to cluster details and a simple resolution smearing is insufficient to describe the data well.

4.2 Signal Sample Selection

Although B mesons are copiously produced in hadronic collisions, they are accompanied by large backgrounds from generic QCD events. The first step in selecting out the signal events from the large backgrounds involves the trigger selection of the data while it is being recorded. These analyses use the dimuon trigger, described in section 4.2.1, which looks for two oppositely charged muons coming from the $J/\psi \to \mu^+\mu^-$ decay. We then search the dimuon data for events which satisfy the basic topology of the decays of interest. This reconstruction procedure is described in section 4.2.2. A significant amount of background (described in section 4.2.3) still survives these basic cuts and we must place harder cuts on certain discriminating variables such as the apparent lifetime of the B candidates to further reduce the level of background. This cut optimization procedure is described in general in section 4.2.4 with the specific variables and results for each mode being described in chapters 5, 6, and 7.

4.2.1 Dimuon Trigger

The dimuon trigger[1], which selects events with $J/\psi \to \mu^+\mu^-$ candidates, is split into three levels with increasingly sophisticated and stringent selection criteria. The first trigger level requires two muon track segments in the muon chambers ($|\eta| < 1.0$) with $p_T > 3.0$ GeV/c. These must be in two different muon trigger wedges in ϕ. These wedges are 10° each so this requirement is approximately that the two muons must be separated by at least 10° in ϕ. The second level trigger requires oppositely charged tracks from the CTC with $p_T > 2.2$ GeV/c which extrapolate to the track stubs in the muon chambers with a matching $\chi^2 < 16$. The third level trigger forms an invariant mass of the two muons and keeps events with a J/ψ candidate mass between 2.8 and 3.4 GeV/c^2. This sample also includes some events ($\sim 10\%$) which pass a single muon trigger[2] at levels 1 and 2 and pass the dimuon trigger at level 3. This sample contains $\sim 300,000$ J/ψ candidates which are used as the starting point to search for $B \to J/\psi K^{(*)0} X$.

The efficiency for a muon with $p_T > 3.0$ GeV/c to be found by both the level one and level two triggers is $\sim 90\%$. This efficiency drops to $\sim 10\%$ at $p_T = 1.5$ GeV/c. Thus the efficiency plateau for finding a $J/\psi \to \mu^+\mu^-$ decay is $\sim (90\%)^2 = 81\%$ when both muons have $p_T > 3.0$ GeV/c. The measured efficiency curves for each trigger level are parameterized and used in a trigger simulation[3] which models the trigger efficiency for the Monte Carlo data.

4.2.2 Decay Reconstruction

In order to reconstruct the specific B decays of interest, we begin by applying quality cuts to the particle tracks and their matches to muon chamber hits. The dimuon trigger requires that each event has two muon stubs with matching CTC tracks that form an invariant mass near the J/ψ mass. The trigger level matching requirement is loose; we tighten the matching χ^2 to be less than 9 in the ϕ direction and less than 12 in the z direction These cuts correspond to approximately 3σ significance cuts on the track to muon matching in the ϕ and z directions.

The triggers used in this analysis use all muon systems described in section 3.2.3. The final $J/\psi \to \mu^+\mu^-$ candidate reconstruction only uses muons which intersect both of the muon systems which cover $|\eta| < 0.6$.

[1] There are actually several dimuon triggers which differ by which combination of the central ($|\eta| < 1.0$) muon chambers have the muon stubs. These triggers and their efficiencies are documented in detail in the CDF internal notes 1999 and 4076. This section describes their collective properties and efficiencies.

[2] There were two single muon triggers: one required the CTC track to have $p_T > 7.5$ GeV/c with muon stubs in both muon systems covering $|\eta| < 0.6$; the other required $p_T > 12$ GeV/c with a hit in any muon system covering $|\eta| < 1.0$.

[3] This trigger simulation, DIMUTG, was written by Steve Pappas and is documented in the CDF internal note 3537.

The CTC track quality cuts require a full 3D fit, hits in at least two axial superlayers and two stereo superlayers, and a CTC exit radius of more than 130 cm (*i.e.*, the track must intersect at least a portion of all CTC superlayers). Information from the SVX is included in the fit if the track has hits in three or four SVX layers.

Provided that at least 6 tracks pass the quality cuts (4 in the case of $B_s^0 \to J/\psi \bar{K}^{*0}$) we proceed by searching for the following decays of the B daughters: $J/\psi \to \mu^+\mu^-$; and $K^0 \to K_S^0 \to \pi^+\pi^-$ or $K^{*0} \to K^+\pi^-$.

For $J/\psi \to \mu^+\mu^-$, we loop over all pairs of oppositely charged muons that pass within 5 cm of each other in z. The z resolution of CTC tracks is approximately 1 cm so this z requirement simply cuts out tracks which obviously come from a different interaction. Using the fitted track parameters and their covariance matrices, we fit for the best (highest probability) tracking parameters solution with the additional constraint that the two tracks intersect each other at some common decay vertex.[4] We require the probability of the χ^2 of this vertex fit to be greater than 0.1% in order to reject candidates which clearly do not come from a common vertex. Muon combinations other than the two trigger muons are allowed provided that they pass these cuts. Usually the trigger muons pass these requirements and we continue by searching for the neutral kaon, either a K_S^0 or a K^{*0}.

To form a neutral kaon candidate, we consider all oppositely charged track pairs within 5 cm of the muons in z, $p_T > 0.5$ GeV/c, and within a $\Delta R \equiv \sqrt{\Delta\phi^2 + \Delta\eta^2} < 1.0$ cone about the direction of the J/ψ candidate momentum and each other. Monte Carlo simulations of B decays indicate that $\sim 95\%$ of signal events pass these ΔR cuts which remove tracks which point in the wrong direction to have come from the same decay vertex as the other tracks being considered. The ΔR and Δz distributions are shown in figure 4.1.

These track pairs are vertexed together and required to have an invariant mass $0.485 < m_{K_S^0} < 0.510$ GeV/c^2 for K_S^0 candidate or $0.820 < m_{K^{*0}} < 0.970$ GeV/c^2 for K^{*0} candidates. K_S^0 candidates are additionally required to have $L_{xy}/\sigma_{L_{xy}} > 5$ in order to separate genuine K_S^0 particles from the short-lived background by taking advantage of their lifetime.

Figure 4.2 shows the reconstructed masses of $J/\psi \to \mu^+\mu^-$, $K^{*0} \to K^+\pi^-$, and $K_S^0 \to \pi^+\pi^-$ from a $B_s \to J/\psi K^{*0} K_S^0$ Monte Carlo sample. The widths of the J/ψ and the K_S^0 are completely dominated by the reconstruction resolution and thus the invariant mass of their decay products is constrainted to the Particle Data Group (PDG) determined mass [11] in the final B vertex fit. The K^{*0} resonance has a Breit-Wigner width $\Gamma = 50.7$ MeV/c^2 which is additionally convoluted with the reconstructed mass resolution. Since the kaon and pion assignments in $K^{*0} \to K\pi$ are not known, both combinations are tried and thus the K^{*0} mass in the upper right of figure 4.2 has two entries per event. The effect of swapping the kaon and pion assignments is evident as the broad Gaussian shaped background underlying the K^{*0} signal peak.

[4] This procedure is referred to as "vertexing" the tracks together.

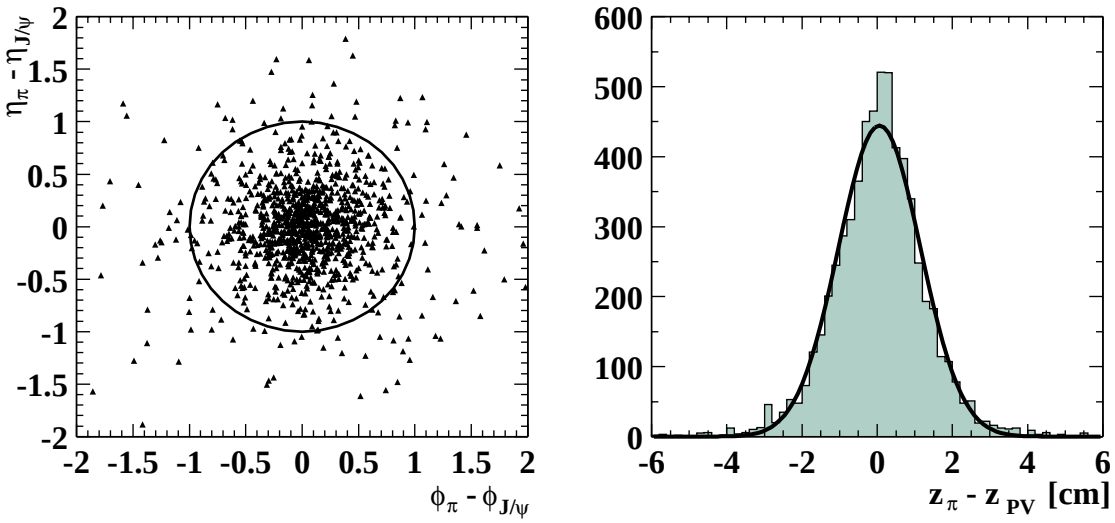

Figure 4.1: $\Delta\eta$ *vs.* $\Delta\phi$ distribution for a pion with respect to the J/ψ in $B^0 \to J/\psi K^0_S \pi^+\pi^-$ Monte Carlo (left). The circle shows the $\Delta R < 1.0$ cut. The right plot shows the reconstructed pion z_0 with respect to the primary vertex in $J/\psi K^0_S \pi^+\pi^-$ data. The σ of the fitted Gaussian is 1.1 cm.

In all modes except $B^0_s \to J/\psi \bar{K}^{*0}$, two additional tracks are required with similar cuts to the previous pairs: opposite charge, $p_T > 0.5$ GeV/c, within $\Delta R < 1.0$ of the J/ψ direction and each other, within 5 cm of the other tracks in z, and a vertex fit probability of greater than 0.1%.

If any combination of tracks in an event passes these requirements, they are vertexed together while additionally constraining the J/ψ and K^0_S masses to their PDG value. In the case of a K^0_S, the two daughter pions are constrained to come from a common vertex and their combined momentum must point back to the decay vertex of the remaining particles. The K^{*0} mass is not constrained since it is a resonance whose width is wider than the mass resolution. The adjusted track parameters from fitting with these additional constraints are used to form the B candidate mass and momentum. Events with a B candidate mass between $4.8 < m_B < 5.8$ GeV/c^2 and a combined vertex fit probability greater than 0.1% are kept.

It is possible that several combinations of tracks in a single event will pass all of the above requirements. In this case each candidate combination is saved. In practice this produces a narrow B mass peak with the correct assignments which is superimposed upon a much broader peak from the other combinations. We model the ratios of areas and widths using a Monte Carlo simulation and use this when fitting the data.

In summary, each of the dimuon events is searched for the B decays of interest by forming track combinations with the correct vertex topology which pass the following cuts:

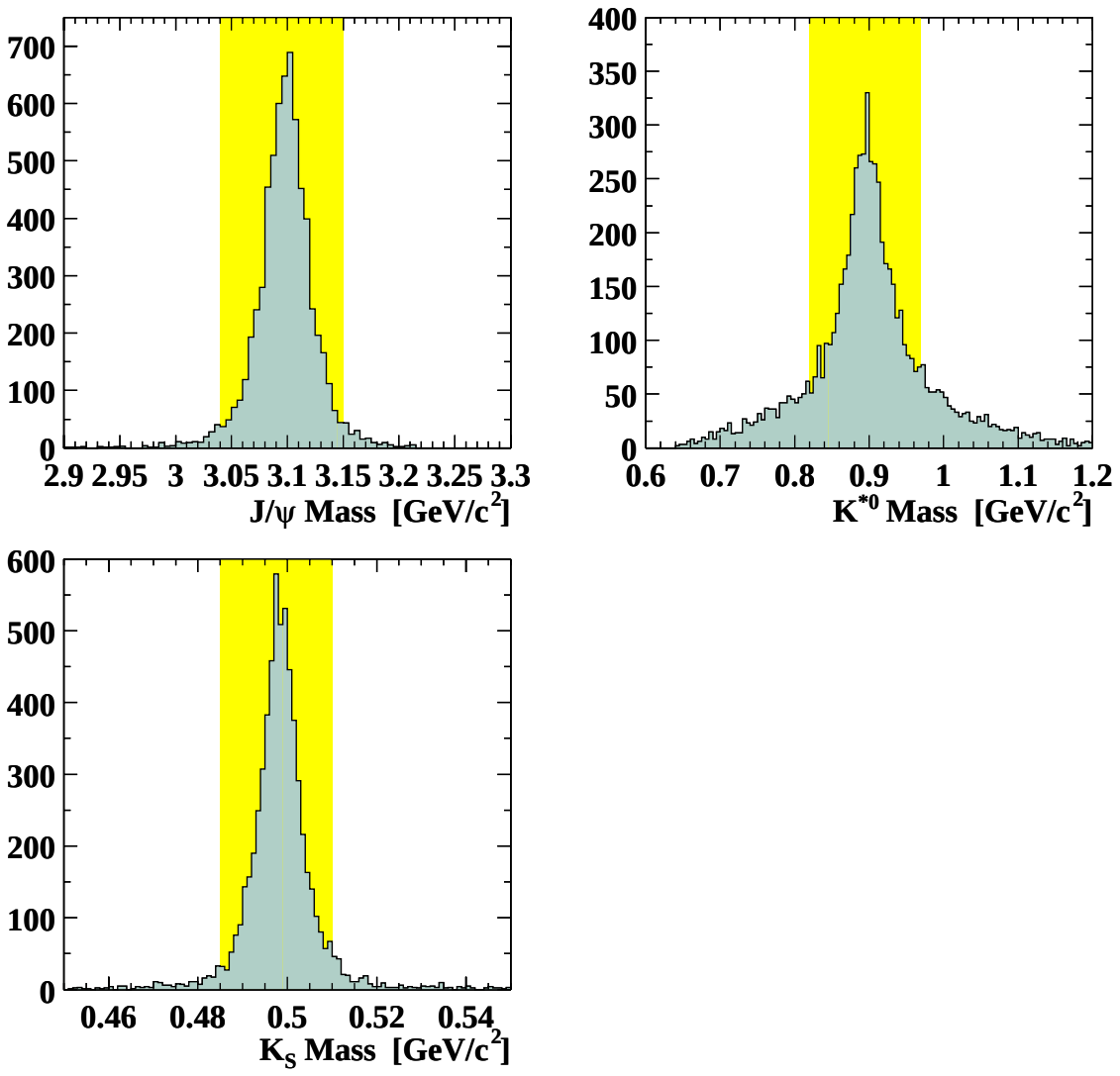

Figure 4.2: Reconstructed Monte Carlo mass peaks for $J/\psi \to \mu^+\mu^-$, $K^{*0} \to K^+\pi^-$, and $K^0_S \to \pi^+\pi^-$. The highlighted region shows the cut values used during reconstruction. The K^{*0} mass plot has two entries per event for the two possible K *vs.* π assignments. The effect of mis-identifying the kaon *vs.* the pion in K^{*0} reconstruction is evident as the broad Gaussian shaped background beneath the K^{*0} peak.

- Track to muon matching within 3σ ($\chi^2_\phi < 9$ and $\chi^2_z < 12$)
- $3.04 < m_{J/\psi} < 3.15$ GeV/c^2 before constraining the J/ψ mass in the B fit
- $0.820 < m_{K^{*0}} < 0.970$ GeV/c^2
- $0.485 < m_{K^0_S} < 0.510$ GeV/c^2 before constraining the K^0_S mass in the B fit
- $|\Delta z| < 5$ cm for decay products
- Vertex fit probability $> 0.1\%$ for J/ψ, K^0_S, K^{*0}, and B.
- $L_{xy}/\sigma_{L_{xy}} > 5$ for K^0_S candidates
- $p_T > 0.5$ GeV/c for all final state particles
- $\Delta R = \sqrt{\Delta\phi^2 + \Delta\eta^2} < 1.0$ for kaons and pions with respect to the J/ψ axis.
- $\Delta R < 1.0$ for kaons and pions with respect to the other kaon or pion coming from the same parent particle (K^{*0}, K^0_S).

4.2.3 Sources of Background

Events which pass the above cuts have the correct decay topology but the dataset still contains a considerable amount of background. This background arises from several sources:

- In the CDF data, there are approximately twice as many J/ψ's from non-B production as there are from B decays [32]. These J/ψ decays may be combined with other tracks to form a fake $B \to J/\psi X$ candidate.
- Random combinations of tracks from QCD production of u, d, and s quarks can form a plausible B candidate.
- Mismeasured tracks can lead to a vertex with apparent lifetime which can mimic a B decay. These mismeasurements can arise from fitting a track with a noise hit or a hit from another track within the Silicon Vertex Detector.
- Combining some of the tracks from a B decay with other tracks from fragmentation, the underlying QCD event, or multiple interactions can produce a B candidate.
- D decays also have lifetime, and in combination with other random tracks they produce B candidates.

We do not have a Monte Carlo simulation or model which correctly describes the details of these backgrounds. Specifically, we do not know their relative fractions. Instead of painstakingly modeling these many complicated processes, we use the "sidebands" of the B mass distribution to model the backgrounds. *I.e.*, we take reconstructed B candidate events with masses slightly above or below the known B mass and use those to model the background. When fitting the background and B signal peak simultaneously, we use a B mass region from 4.8 to 5.8 GeV/c^2. When estimating the expected background for distributions such as the $\pi^+\pi^-$ invariant mass, we use sidebands from 5.0 to 5.6 GeV/c^2 while excluding $\pm 2\sigma$ around the B mass.

4.2.4 Background Reduction

In order to reduce backgrounds we make use of several discriminating variables which have different distributions between the signal and background. We studied several possible cut variables using Monte Carlo simulations and $B^0 \to J/\psi K^0_S$ and $B^0 \to J/\psi K^{*0}$ data to model the signal, while using events in the sidebands of the B mass peak to model the background. The following variables have the best discriminating power between signal and background:

- $p_T(K^{*0})$ or $p_T(K^0_S)$: The signal decay products tend to have higher momenta than average background particles due to the boost from the mass of the decaying B as well as the production momentum of the B. The muons already have high p_T requirements due to trigger requirements. In principle we could make p_T cuts on the individual K^0_S or K^{*0} daughters, but cutting on the p_T of the parent neutral kaon accomplishes the same effect.

- $ct(B)$: Since the background is predominantly from the point of the $p\bar{p}$ collision while the B has a lifetime allowing for a displaced secondary vertex, a ct cut can powerfully reduce backgrounds. The B lifetime τ is 1.55 ps which corresponds to a $c\tau$ of 464 μm. Since this is an exponentially falling distribution, typical ct cuts are between 0 and 300 μm so as to not lose too much signal. While this cut is powerful for reducing QCD backgrounds, it cannot reduce backgrounds with genuine lifetime such as those arising from other B decays.

- Iso(B) : In a genuine B event, the B daughter tracks carry the majority of the momentum in a ΔR cut about the B momentum direction. Fake B candidates from background events tend to carry a smaller fraction of the total momentum within a ΔR cut about the B candidate momentum. A measure of this effect is the isolation, defined as

$$\mathrm{Iso}(B) \equiv \frac{p_T(B)}{p_T(B) + \sum_i p_T(t_i)} \tag{4.3}$$

  where $\{t_i\}$ are the tracks with $\Delta R < 1.0$ with respect to the candidate B momentum, excluding the candidate B daughter tracks. A cut requiring high

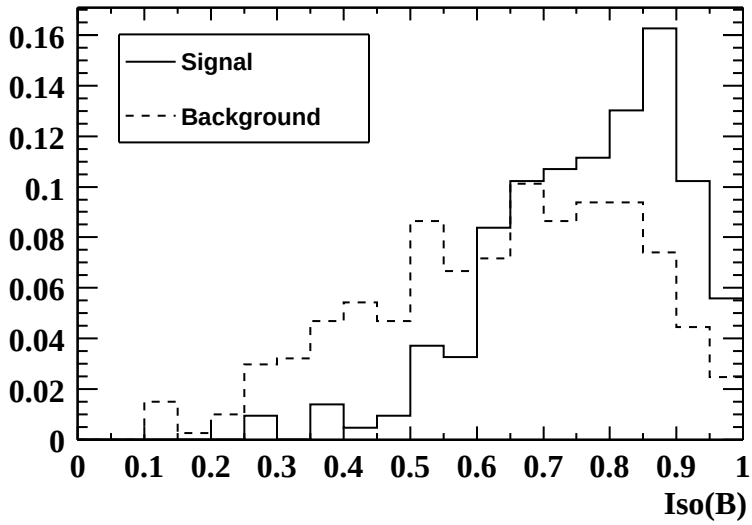

Figure 4.3: B candidate isolation, Iso(B), for $B^0 \to J/\psi K^{*0}$ signal (solid histogram) and sideband background (dashed histogram) events.

isolation is preferential toward genuine B events. Figure 4.3 shows Iso(B) for $B^0 \to J/\psi K^{*0}$ signal (solid histogram) and background (dashed histogram) events.

The goal is to optimize these cuts to maximize the expected $S^2/(S+B)$ while not simply optimizing on a statistical fluctuation in the data. In order to accomplish this we systematically vary the cuts while applying them to both the signal (*e.g.*, $B^0 \to J/\psi K^0_S \pi^+\pi^-$) and reference (*e.g.*, $B^0 \to J/\psi K^0_S$) datasets. For a given set of cuts we estimate the background size (B) using the signal data sidebands and estimate the signal size (S) using the number of events in the reference mode times a scaling factor[5]. Using this procedure to estimate S and B, we select the cut combination which maximizes the expected $S^2/(S+B)$.

The scaling factor between the signal size and the reference size depends upon the branching fraction which we are trying to measure. To estimate this scaling factor, we first optimize for the search sensitivity (approximately S^2/B) which does not require knowing a scale factor but tends to produce harder cuts which are optimized for observing a small signal but not for the statistical power of measuring a branching ratio. While optimizing the cuts for search sensitivity, we also track the average scale factor between the signal and reference. We find that the final cuts and result are mostly insensitive to the exact choice of the scaling factor and variations within 50% produce similar results without biasing the final answer toward the exact scale

[5]The scaling factor includes a cut-specific correction based upon the different $p_T(K)$ spectra between the signal and reference datasets as determined with Monte Carlo.

factor we are using. Thus although this procedure is not strictly "black box"[6], it accomplishes the goal of optimizing a set of cuts while avoiding significant bias.

As a cross check of the method, we also tried using a Monte Carlo sample as the reference signal and found similar results. In the end we chose to use the data reference rather than a Monte Carlo reference based on the principle that it is generally better to use data instead of Monte Carlo when possible.

Since we use the data sidebands to estimate the background both during the cut optimization procedure and during the final measurement, we must take care to avoid the bias of simply optimizing on a low fluctuation of the sidebands. In order to accomplish this we use two independent interleaved regions of the sidebands: one region for estimating the background while optimizing the cuts and the other for estimating the background while making the final signal measurement. Specifically, we bin the sidebands in 10 MeV/c^2 bins and use the odd numbered bins while optimizing the cuts and the even numbered bins while making the final measurement.

4.3 Cancellation of Efficiencies

Many cut efficiencies (such as that of the ct cut) simply cancel in the ratio of efficiencies. Others do not cancel, generally leading to higher efficiency for the reference mode than for the signal mode. As long as the difference in the efficiencies is modeled by the Monte Carlo, it is not a problem that they do not exactly cancel.

The dominant effect that causes different cut efficiencies is simply the kinematic acceptance. The existence of extra decay products makes it less likely that the entire signal event will end up within the detector acceptance as well as slightly softening the p_T spectra of all final state particles.

The extra decay products also allow more angular momentum degrees of freedom which allow the decay helicities to be different between the signal and reference modes resulting in different p_T spectra. This effect is most important for the muons which have a high p_T cut due to the dimuon trigger threshold. To a lesser degree this also affects the $p_T(K^{*0})$ and $p_T(K^0_S)$ spectra. In calculating the ratio of efficiencies, we use an equal amount of transverse and longitudinal polarization in the signal Monte Carlo. Deviations from this assumption are treated as a systematic uncertainty and are discussed in section 4.5.

Section 4.4 discusses corrections to the ratio of efficiencies for two reconstruction aspects that the Monte Carlo does not model well: the tracking efficiency of particles within the kinematic acceptance of the CTC and the efficiency of the isolation cut.

The remaining cuts whose efficiencies cleanly cancel are:

- Masses: Cuts on the J/ψ, K^{*0}, and K^0_S masses completely cancel between signal and reference.

[6] *I.e.*, it does not rigorously avoid looking at the signal data until the final measurement in order to avoid all possible human bias.

- $|\Delta z| < 5$ cm is considerably larger than the z vertex resolution of approximately 1 cm and should be equally efficient for both reference and signal even though the signal has two extra tracks.

- Fit probability: A 0.1% probability cut should be 99.9% efficient regardless of decay topology, but to check this requirement, we studied the vertex fit probability cut efficiency for cuts of 0.1%, 1%, and 5% for data samples of $B^+ \to J/\psi K^+$ (3 tracks), $B^0 \to J/\psi K^{*0}$ (4 tracks), and $B^0 \to J/\psi K^0_S$ (4 tracks from two different vertices) with and without mass constraints on the J/ψ and K^0_S. For a given cut, the efficiencies were the same for all modes within the statistical error. We also tried the same procedure on much larger MC datasets (with appropriately better statistical power) and found the same results. Thus we conclude that although the signal and reference modes have different decay topologies, the fit probability cuts have equal efficiency.

- L_{xy} of the K^0_S: The K^0_S L_{xy} distributions are nearly identical between the signal and reference modes, thus these efficiencies cancel.

- SVX hit requirements: We only require SVX hits on tracks which have equivalents between the signal and the reference thus their efficiencies cleanly cancel. *e.g.* in $B^0 \to J/\psi K^0_S \pi^+ \pi^-$ we do not require the two extra pions to have SVX hits.

- $ct(B)$: Since this is not a function of the decay mode, its distribution should be the same for signal and reference. The only possible observable difference comes from the ct resolution difference from having two extra tracks in the signal mode. In the Monte Carlo simulation, this potential effect is not evident to within 1% for any given ct cut.

4.4 Efficiency Corrections

Many efficiencies cancel in the ratio of efficiencies in equation 4.2. Those which do not are dominated by kinematic effects which are generally well modeled in the Monte Carlo simulation.

Two effects which the Monte Carlo does not properly model are the efficiency of the isolation cut and the tracking efficiency of particles within the kinematic acceptance of the CTC. For particles within the kinematic acceptance of the CTC, the primary source of inefficiency is interference from other particle tracks, *e.g.*, those from the underlying event. Since the Monte Carlo simulation only models the B decay daughters, it does not include these other tracks and thus its tracking efficiency is too high. Likewise, since the Monte Carlo does not include fragmentation tracks or the underlying event, it does not have a meaningful Iso(B) upon which to find the

efficiency of the isolation cut. Both of these effects must be explicitly modeled and corrected for in the ratio of efficiencies.

4.4.1 Tracking Efficiency Corrections

The CTC tracking efficiency correction is estimated by embedding Monte Carlo tracks into real data events and finding the efficiency for reconstructing them[7]. Figure 4.4 (top) shows the resulting efficiency curve for positive pions with a plateau value of 97%. For each final state particle, this curve (or the very similar one for negative particles) is multiplied by the p_T spectrum histogram. Figure 4.4 (bottom) shows an example of the p_T spectrum for the two extra pions in $B^0 \to J/\psi K^0_S \pi^+\pi^-$. The ratio of areas between the corrected and uncorrected histograms gives the tracking efficiency correction. In general the p_T spectra for the J/ψ and K^0_S or K^{*0} daughters are similar enough between the signal and reference modes that their efficiency corrections cancel and this correction effectively only matters for the extra particles in the signal modes.

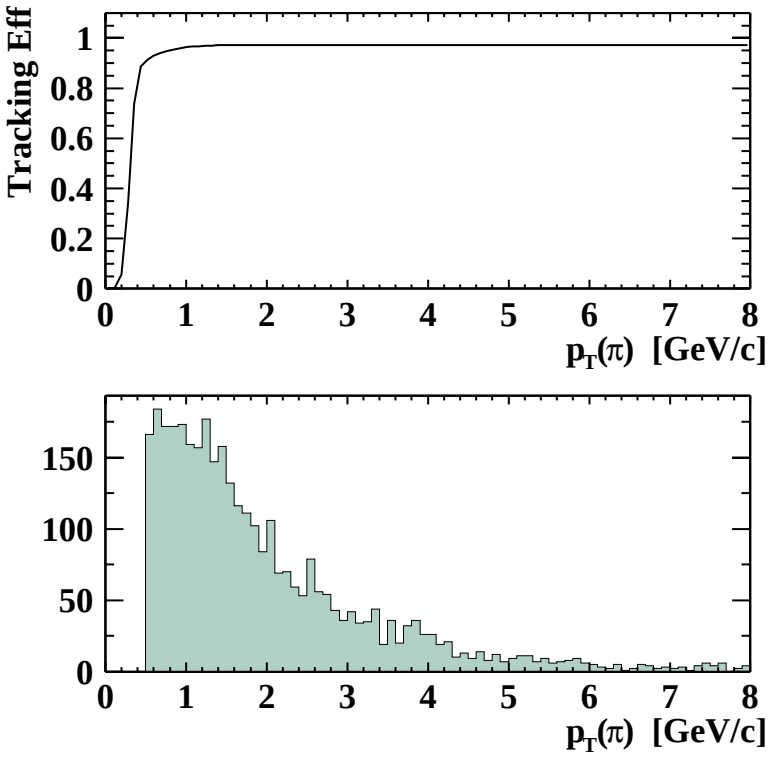

Figure 4.4: Positive pion tracking efficiency (top) and the $p_T(\pi)$ spectrum for the two extra pions in $B^0 \to J/\psi K^0_S \pi^+\pi^-$ Monte Carlo with loose cuts (bottom).

[7] This study was performed by Andreas Warburton and is documented in the internal CDF note number 4423.

If all particles had high enough p_T to be on the efficiency plateau, the correction would be $(97\%)^2 = 94\%$, but since some particles have lower p_T with lower efficiencies, the correction is typically $\sim 92\%$.

4.4.2 Isolation Cut Efficiency Corrections

The isolation variable $\mathrm{Iso}(B) = p_T(B)/(p_T(B) + \sum_i p_T(t_i))$ depends upon both $p_T(B)$ and $p_T(x) \equiv \sum_i p_T(t_i)$ where the $\{t_i\}$ represent all non-B daughter tracks within $\Delta R < 1.0$ about the B direction. $p_T(x)$ is a result of the underlying event and the fragmentation tracks produced during the hadronization of the B and thus should be independent of the B decay mode. It possibly could have a dependence upon $p_T(B)$; figure 4.5 (left) shows $p_T(B)$ *vs.* $p_T(x)$ for $B^0 \to J/\psi K^{*0}$ data. The profile histogram on the right of figure 4.5 indicates that $p_T(x)$ and $p_T(B)$ are essentially uncorrelated[8]. Thus to model $\mathrm{Iso}(B)$, we take the $p_T(x)$ distribution as measured in the data (figure 4.6 upper right) and combine it with $p_T(B)$ as determined from the Monte Carlo (figure 4.6 left) to form the $\mathrm{Iso}(B) = p_T(B)/(p_T(B) + p_T(x))$ distributions. The resulting $\mathrm{Iso}(B)$ distributions for the signal and reference modes are compared to find the ratio of efficiencies for a given $\mathrm{Iso}(B)$ cut and used to correct the Monte Carlo ratio of efficiencies.

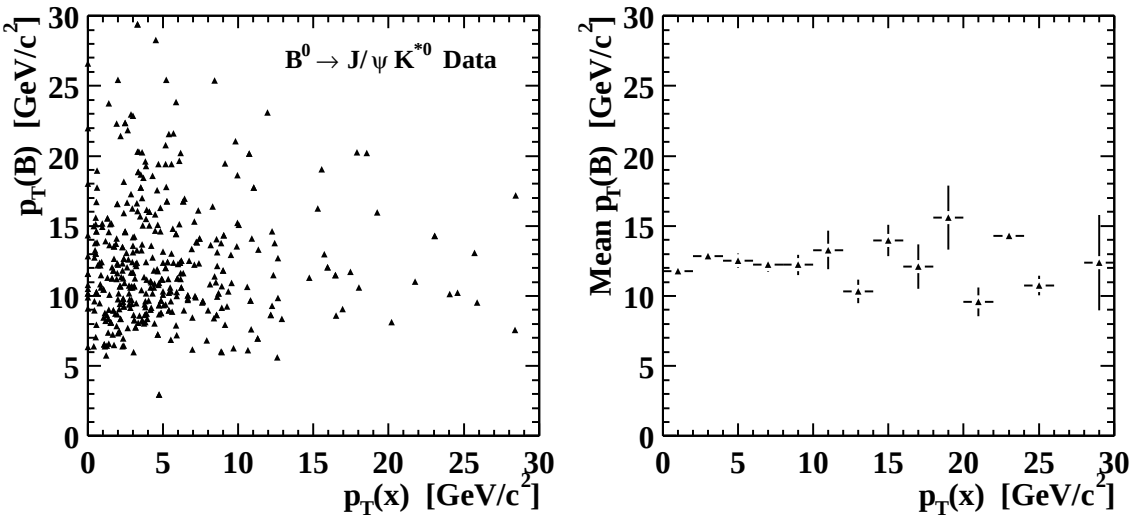

Figure 4.5: $p_T(B)$ *vs.* $p_T(x) \equiv \sum_i p_T(t_i)$ for $B^0 \to J/\psi K^{*0}$ data (left). The profile histogram on the right shows that these quantities are essentially uncorrelated.

Varying the $p_T(B)$ spectra (*e.g.*, by varying the $p_T(K^{*0})$ cut) affects the absolute efficiency of a given $\mathrm{Iso}(B)$ cut, but this effect cancels to better than 2% in the ratio

[8]See also CDF internal notes 3684 and 3523 regarding the lack of correlation between these two variables.

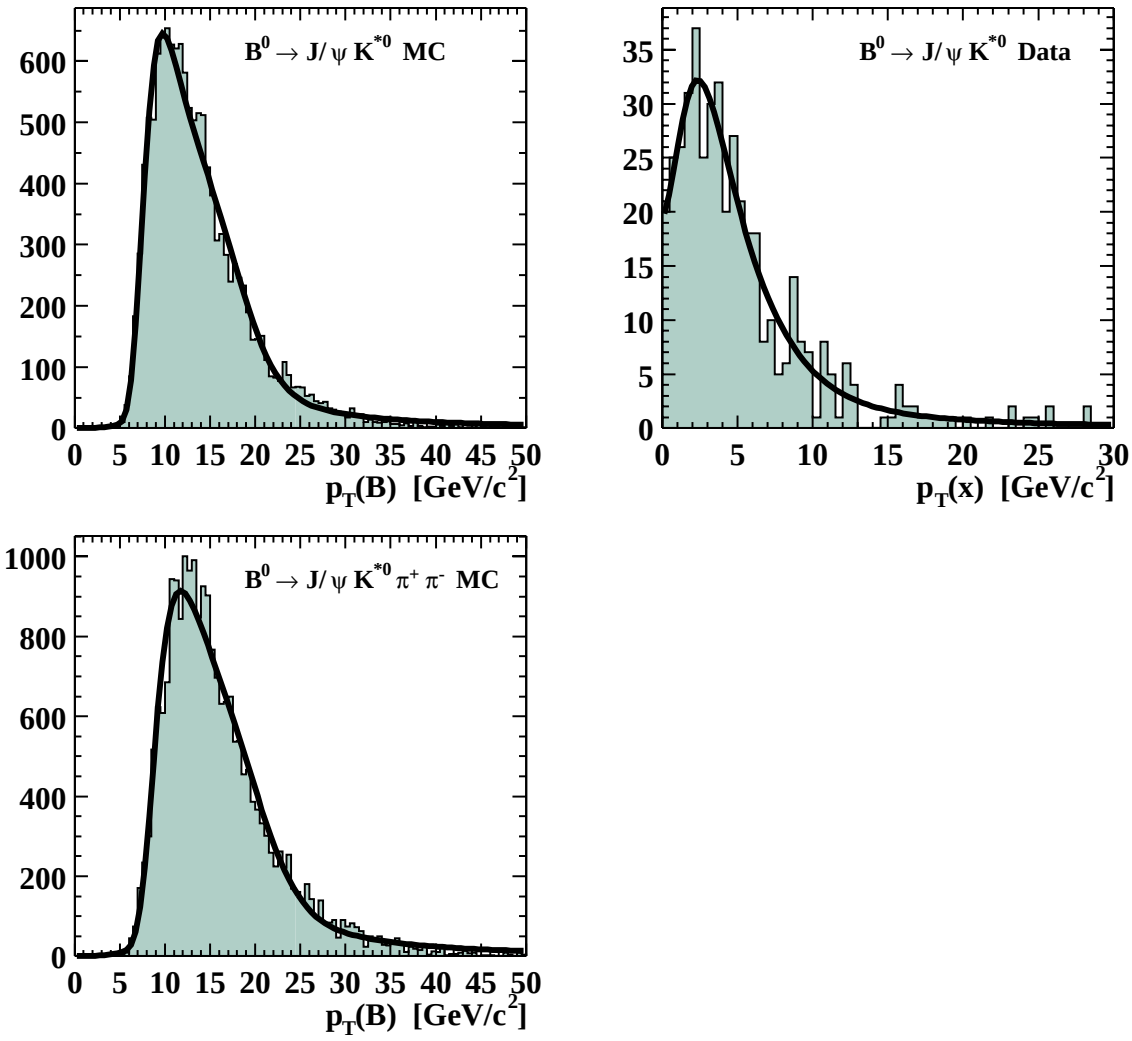

Figure 4.6: $p_T(x) \equiv \sum_i p_T(t_i)$ projection (upper right) from $B^0 \to J/\psi K^{*0}$ data. $p_T(B)$ for $B^0 \to J/\psi K^{*0}$ and $B^0 \to J/\psi K^{*0}\pi^+\pi^-$ (upper and lower left, respectively) from Monte Carlo with the reconstruction cuts listed in section 4.2.2.

of efficiencies. Similarly, varying the parameters of the $p_T(x)$ parameterization by $\pm 1\sigma$ has less than a 2% effect on the ratio of efficiencies.

4.5 Common Systematic Uncertainties

The dominant uncertainty in all of the modes studied comes from the statistical uncertainty associated with the small signal size. There are additional systematic uncertainties in the efficiency calculations but most of these cleanly cancel in the ratio with the reference signal. Uncertainties below 2% are neglected. *E.g.*, the

tracking efficiency corrections applied to the Monte Carlo are known to better than 2% and thus their uncertainties are not included as a systematic uncertainty. The source of systematic uncertainties which do not cleanly cancel are:

- Reference mode branching ratio: This uncertainty does not enter in the measurement of the ratio of branching ratios, but it is the dominant systematic uncertainty in the absolute measurement of the signal branching fractions.

- Decay helicity model: All of the signal modes except $B_s \to J/\psi \bar{K}^{*0}$ have angular momentum degrees of freedom which are not present in the reference modes. Thus the helicity composition of the signal modes could be different than for the reference modes, leading to different p_T spectra of the final state particles. This is particularly important for the J/ψ daughters which have a high minimum p_T cut due to the dimuon trigger. To model this effect, we generated Monte Carlo samples that were completely longitudinally or transversely polarized and compared their efficiencies. We used the RMS of the efficiency distribution as the polarization is varied from completely transverse to completely longitudinal, treating all values as equally likely.[9] Since the efficiency is linear with the longitudinal (or transverse) polarization fraction, the RMS is simply the maximum difference divided by $\sqrt{12}$.

- B production model: Varying parameters of the MRSD0 parton distribution function produces different $p_T(B)$ spectra in the Monte Carlo data. This effect mostly cancels in the ratio of efficiencies but there is a small systematic due to uncertainties of the B production model. We varied the renormalization scale and the mass of the b quark and took half of the maximum spread of efficiencies as a conservative estimate of this uncertainty.

- Trigger model: The Monte Carlo simulation models the level 1 and 2 dimuon triggers on the muon daughters of the J/ψ. In the data about 20% of the events pass this trigger with one of the muons coming from a fake or a muon from the other B in the event. Additionally, about 10% of the events are from a single muon trigger at level 1 and 2 which passes a dimuon trigger at level 3. Our Monte Carlo modeling of these scenarios is less sophisticated than for the dimuon trigger of the J/ψ muon daughters, but fortunately these cases only apply to a minority of the events. To account for these scenarios we include a 5% systematic uncertainty on the trigger model.

[9] This is a simplified version of total helicity phase space available to a 3 body decay, but it encompasses the full range of the most important effect of the J/ψ polarization and thus is a good representation of the issue at hand.

Chapter 5

$B^0 \to J/\psi K^{(*)0}\pi^+\pi^-$

5.1 $B^0 \to J/\psi K^*(892)^0\pi^+\pi^-$

5.1.1 Overview

In general, B decays to $K^{*0}X$ occur somewhat more frequently than the equivalent K^0X modes. *E.g.*, $\mathrm{BR}(B^0 \to J/\psi K^{*0}) = 1.5 \times 10^{-3}$ is larger than $\mathrm{BR}(B^0 \to J/\psi K^0) = 8.9 \times 10^{-4}$. Additionally, K^{*0} modes are more easily reconstructed since $\mathrm{BR}(K^{*0} \to K^+\pi^-) = 2/3$ whereas $\mathrm{BR}(K^0 \to K^0_S \to \pi^+\pi^-) = 1/2 \cdot 2/3 = 1/3$. Thus even for the same branching ratio to $K^{*0}X$ *vs.* K^0X, twice as many $K^{*0}X$ events would be observed than K^0_SX events. Thus we begin by searching for the quark popping mode $B^0 \to J/\psi K^{*0}\rho^0$ as shown in figure 5.1.

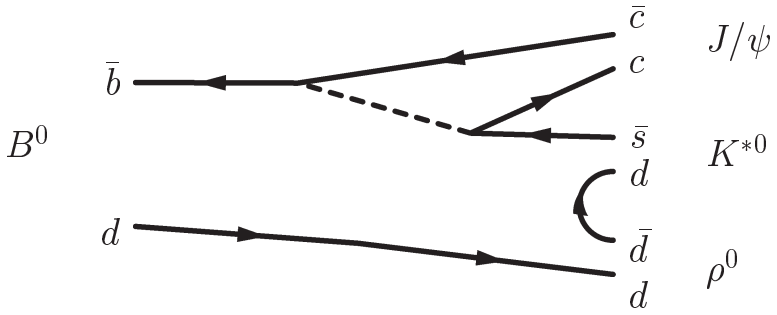

Figure 5.1: Feynman diagram for $B^0 \to J/\psi K^{*0}\rho^0$.

There are several decays in addition to $B^0 \to J/\psi K^{*0}\rho^0$ which could contribute to the observed final state $B^0 \to J/\psi K^{*0}\pi^+\pi^-$. Other possible contributors include $B^0 \to \psi(2S)K^{*0}$ and $B^0 \to J/\psi K^*(1270)^+\pi^-$ with $K^*(1270)^+ \to K^{*0}\pi^+$. Since the ρ^0 resonance is so wide (the full width at half max is 150 MeV, centered at 770 MeV), it is impossible to make a $\pi^+\pi^-$ mass cut to select out only the ρ^0 contribution. Thus we initially search for $B^0 \to J/\psi K^{*0}\pi^+\pi^-$ and then

inspect the invariant mass distribution $m(J/\psi\pi^+\pi^-)$ for $\psi(2S) \to J/\psi\pi^+\pi^-$ contributions and the $K^{*0}\pi^+\pi^-$ Dalitz plot and its projections for $\rho^0 \to \pi^+\pi^-$ and $K^*(1270)^\pm \to K^{*0}\pi^\pm$. We also look at the $m(K^{*0}\pi^+\pi^-)$ distribution to look for contributions such as $B^0 \to J/\psi(K_2^*(1430) \to K^{*0}\pi^+\pi^-)$.

5.1.2 Reconstruction and Cut Optimization

Figure 5.2 shows the background $m^2(\pi^+\pi^-)$ distribution[1] taken from the sidebands[2] of the B mass distribution. The backgrounds peak at low $m^2(\pi^+\pi^-)$. To reduce these backgrounds while optimizing the cuts for $B^0 \to J/\psi K^{*0}\pi^+\pi^-$ we require $m^2(\pi^+\pi^-) > 0.3$ (GeV/c^2)^2.

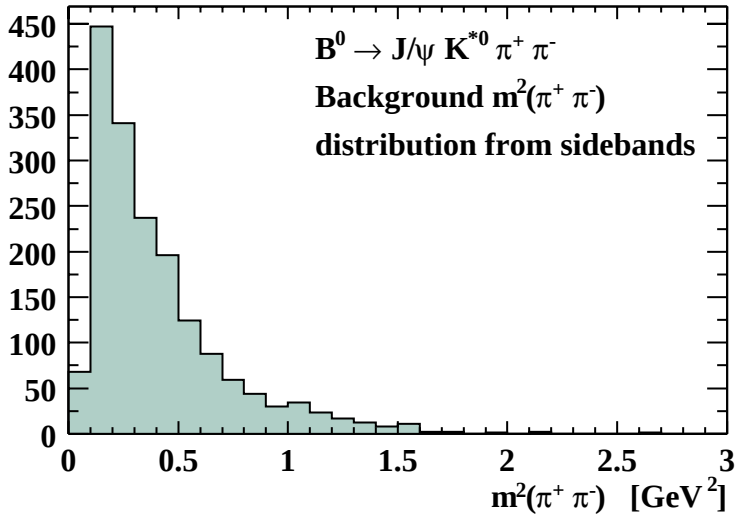

Figure 5.2: Background $m^2(\pi^+\pi^-)$ distribution from the $B^0 \to J/\psi K^{*0}\pi^+\pi^-$ data sidebands. A $B^0 \to J/\psi K^{*0}\rho^0$ quark popping decay would have a $m^2(\pi^+\pi^-)$ distribution centered at the ρ^0 mass squared, *i.e.*, 0.6 (GeV/c^2)^2. Non-resonant $B^0 \to J/\psi K^{*0}\pi^+\pi^-$ also peaks at low $m^2(\pi^+\pi^-)$ but has a slightly higher mass distribution than the background.

As described in section 4.2.4, we scanned cut values for $ct(B)$, $p_T(K^{*0})$, and Iso(B) to optimize the expected $S^2/(S+B)$. In order to have sufficient precision to make a meaningful $ct(B)$ cut, at least two of the four J/ψ and K^{*0} daughters are required to have SVX information. The resulting optimized cuts are shown in table 5.1.

[1]For projections of Dalitz plots we show the mass squared so that they may be directly related to the Dalitz plots shown. For other mass quantities such as $m(J/\psi\pi^+\pi^-)$ we plot the mass (not squared) for easier identification of the location of potential resonances.

[2]The sidebands used to estimate the backgrounds in this chapter are for $m(B)$ between 5.0 and 5.6 GeV/c^2 while excluding $\pm 2\sigma$ about the nominal B mass of 5.28 GeV/c^2.

Cut	Minimum	Maximum	Step Size	Optimized
$p_T(K^{*0})$	1.6 GeV/c	3.0 GeV/c	0.1 GeV/c	2.4 GeV/c
$ct(B)$	100 μm	300 μm	10 μm	170 μm
Iso(B)	0.40	0.80	0.05	0.60

Table 5.1: Optimized cuts for $B^0 \to J/\psi K^{*0}\pi^+\pi^-$.

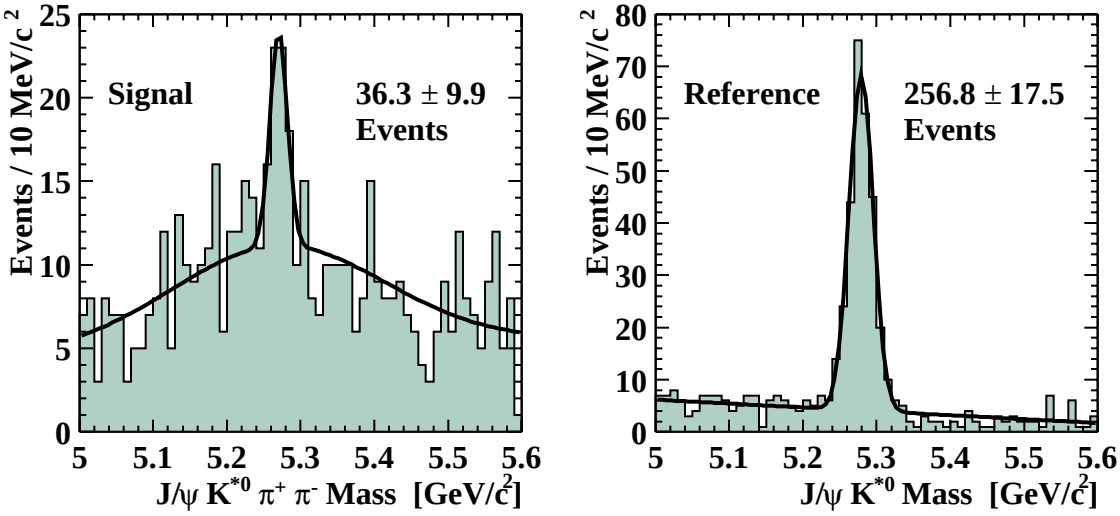

Figure 5.3: Mass of $B^0 \to J/\psi K^{*0}\pi^+\pi^-$ candidates (left) with optimized cuts. The background includes a broad Gaussian due to K *vs.* π particle mis-identification as discussed in the text and shown for the Monte Carlo in figure 5.4. The mass peak of the reference mode $B^0 \to J/\psi K^{*0}$ with the same cuts is shown on the right.

Figure 5.3 (left) shows the resulting mass peak with 36.3 ± 9.9 fitted signal events. With the same cuts, the reference mode $B^0 \to J/\psi K^{*0}$ has 256.8 ± 17.5 events, shown on the right of figure 5.3. The signal has three pions and a kaon coming from the same decay vertex; frequently several different combinations of these particles can form a good K^{*0} candidate. We model this effect in the Monte Carlo simulation and find a narrow peak from the correct assignments superimposed upon a much broader peak of various other combinations as shown in figure 5.4 (left). The number of candidates per events for both data and Monte Carlo are shown on the right of figure 5.4. Although the data have a slightly larger average number of candidates per event, the Monte Carlo reproduces the distribution well. Thus we fit the data with two Gaussians plus a linear background to account for this $K \leftrightarrow \pi$ swapping effect. We fix the widths of the two Gaussians but allow their areas to float in the fit since fragmentation and other background tracks in the data provide additional

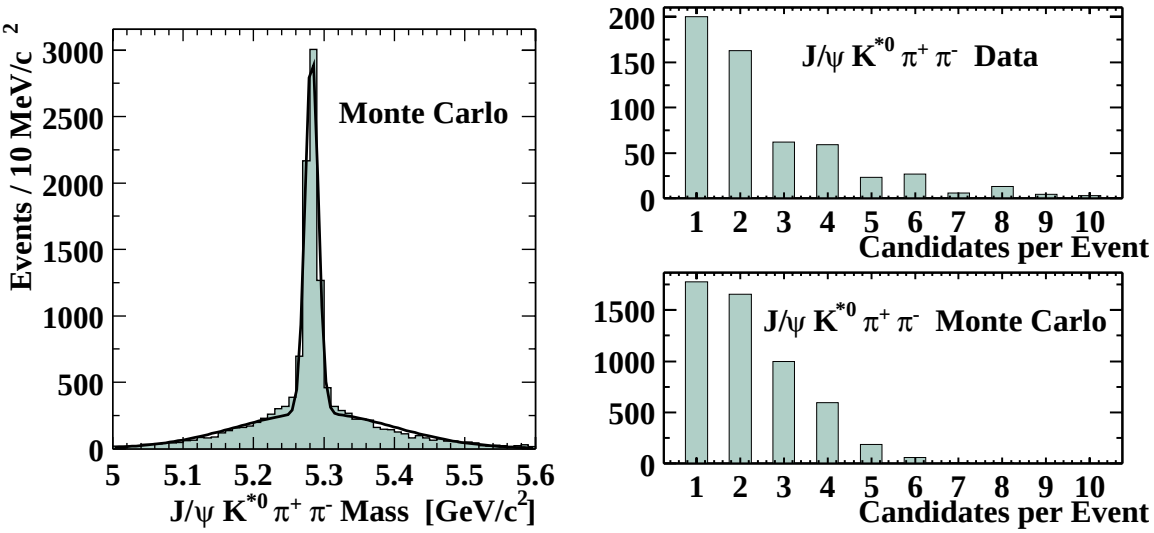

Figure 5.4: Effects of $K \leftrightarrow \pi$ swapping in $B^0 \to J/\psi K^{*0}\pi^+\pi^-$. The left plot shows the broad Gaussian-shaped background of incorrect assignments underneath the signal peak of correct assignments. The right plots show the number of candidates per event in data (top) and the Monte Carlo simulation (bottom).

combinations for K^{*0} candidates.

5.1.3 Ratio of Efficiencies

In order to extract branching ratios from the observed number of events, the ratio of efficiencies between the signal and reference modes must be determined. These efficiencies must include all efficiencies of trigger, geometric/kinematic acceptance, reconstruction, and final cuts. We estimate these using a Monte Carlo dataset as described in chapter 4. For this mode the Monte Carlo simulation includes 5.5 million $B^0 \to J/\psi K^{*0}\pi^+\pi^-$ (non-resonant $\pi^+\pi^-$) events; 4 million $B^0 \to J/\psi K^{*0}\rho^0$ events; and 0.3 million $B^0 \to J/\psi(K^*(1430)^+ \to K^{*0}\pi^+)\pi^-$ events. All modes have similar reconstruction efficiencies so the exact composition is not crucial and any deviation will be included as a systematic uncertainty.

Table 5.2 lists the efficiencies for each step of the trigger, reconstruction, and cut optimization. The efficiencies listed (except the total efficiency) are for each step individually, *i.e.* they represent the efficiency of an event passing a step given that it has passed all previous steps.

The steps listed are:

- Basic Acceptance: This is a filter module which passes events at the Monte Carlo generator level only if all final state particles are within $|\eta| < 1.1$ and $p_T > 0.4$ GeV/c. Muons are additionally required to have $p_T > 1.5$ GeV/c.

Step	$B^0 \to J/\psi K^{*0}\pi^+\pi^-$	$\epsilon(\%)$	$B^0 \to J/\psi K^{*0}$	$\epsilon(\%)$
Events Generated	9,800,000	—	3,500,000	—
Basic Acceptance	417,061	4.3	473,127	14
Dimuon Trigger	61,587	15	52,895	11
Track Quality	58,209	95	49,503	94
Decay Reconstruction	19,942	34	15,964	32
Final Cuts	6271 ± 93	31	8410 ± 122	53
Tracking Efficiency Corr.	—	92	—	—
Isolation Efficiency Corr.	—	—	—	92
Total Efficiency		0.0589		0.221

Table 5.2: $B^0 \to J/\psi K^{*0}\pi^+\pi^-$ reconstruction efficiencies

This cut is primarily intended to save time by preventing detailed detector simulation of events which will fail later cuts.

- Dimuon Trigger: This filter simulates the muon finding and trigger efficiencies. The higher efficiency for the signal over the reference is an artifact of running the Basic Acceptance module first. Since the signal has six particles which must be above a minimum p_T threshold and the reference mode only has four, the signal events which pass the Basic Acceptance module have a higher $p_T(B)$ spectrum than the reference events. This higher $p_T(B)$ spectrum leads to a higher $p_T(\mu)$ spectrum and thus a greater trigger efficiency for $J/\psi K^{*0}\pi^+\pi^-$ events which have all final state particles above the minimum p_T threshold.

- Track Quality: This filter applies track quality cuts and ensures that enough tracks have been reconstructed to be able to proceed with reconstruction of the decay.

- Decay Reconstruction: This filter applies vertexing, mass constraints, etc. and passes events which are B candidates in the selected mode. The events which pass this step form the dataset upon which the remaining cut optimizations are performed.

- Final Cuts: The number of reconstructed events with the final optimized cuts of table 5.1.

- Tracking Efficiency Correction: The Monte Carlo simulation of the event is unrealistically clean since it does not include fragmentation tracks, the underlying event, or multiple interactions per event. This term corrects for the efficiency of reconstructing CTC tracks as described in section 4.4.1. Since the efficiency correction on the J/ψ and K^0_S daughters cancel, the correction is listed only for the two extra pions of the signal.

- Isolation Efficiency Correction: The Monte Carlo does not model Iso(B) because it does not include fragmentation particles or those from the underlying event. This term corrects for the isolation cut efficiency difference between signal and reference as described in section 4.4.2.

The resulting ratio of efficiencies is $\epsilon_{ref}/\epsilon_{sig} = 0.221\%/0.0589\% = 3.75$.

5.1.4 Uncertainties

The dominant source of uncertainty is the statistical uncertainty associated with the small signal size: $9.9/36.3 = 27.3\%$. Combining this with the statistical uncertainty on the reference sample size of $17.5/256.8 = 6.8\%$ results in a total statistical uncertainty of 27.8%.

The systematic uncertainties as described in section 4.5 are dominated by the reference mode branching ratio and the decay helicity model. We estimate the uncertainty due to the decay helicity model by separately modeling longitudinally and transversely polarized components of $B^0 \to J/\psi K^{*0}\rho^0$. We find the RMS of the efficiency spread to be 9.9%.

There is also some uncertainty associated with the signal width and the width of the $K \leftrightarrow \pi$ swapped background width. The Monte Carlo estimates the signal width to be 9.3 MeV/c^2 and the swapped background to be 12.3 times wider. The Monte Carlo underestimates the $J/\psi K^{*0}$ signal width by 27% so we scale the widths used in the fit up by this amount and fix the signal width to 11.8 MeV/c^2 and the swapped width to be $11.8 \times 12.3 = 145$ MeV/c^2. Allowing the signal width to float in the fit reduces it by 10% with a 6.9% reduction in the fitted signal size. Varying the ratio of widths by $\pm 10\%$ results in a $\pm 3\%$ change in the signal. Thus we include a 7.5% systematic for our uncertainty in the widths used in the fit.

We estimate the effect of sample composition uncertainty by comparing the efficiencies of a pure $B^0 \to J/\psi K^{*0}\rho^0$ Monte Carlo sample with that of a $B^0 \to J/\psi K^{*0}\pi^+\pi^-$ (non-resonant) sample. The RMS of this efficiency spread is 5%.

As mentioned in section 4.5, our trigger model of "volunteer" events adds an overall systematic uncertainty of 5%.

The effect of various B production models mostly cancels in the ratio between signal and reference mode efficiencies and results in an uncertainty of 2.5%.

The uncertainty on the tracking efficiency correction is less than 2% and is neglected here.

Table 5.3 summarizes the uncertainties in measuring BR($B^0 \to J/\psi K^{*0}\pi^+\pi^-$).

5.1.5 BR($B^0 \to J/\psi K^{*0}\pi^+\pi^-$)

Combining these results produces the ratio of branching ratios:

$$\frac{\mathrm{BR}(B^0 \to J/\psi K^{*0}\pi^+\pi^-)}{\mathrm{BR}(B^0 \to J/\psi K^{*0})} = \frac{N_{sig}}{N_{ref}} \cdot \frac{\epsilon_{ref}}{\epsilon_{sig}} \tag{5.1}$$

Statistical Uncertainty	%	Systematic Uncertainty	%
Signal Size	27	Reference BR	11.3
Reference Size	6.8	Helicity Model	9.9
		Signal Width	7.5
		Trigger Model	5.0
		Sample Composition	5.0
		B Production Model	2.5
Combined Statistical	**27.8**	Combined Systematics	**18.4**
Uncertainties		Without ref. BR uncer.	**16.8**

Table 5.3: BR($B^0 \to J/\psi K^{*0}\pi^+\pi^-$) uncertainties

$$= \frac{36.3}{256.8} \cdot \frac{0.221}{0.0589} \tag{5.2}$$

$$= 0.53 \pm 0.15 \pm 0.09 \tag{5.3}$$

where the first uncertainty is statistical and the second is systematic.

Using the reference mode branching ratio of BR($B^0 \to J/\psi K^{*0}$) $= (1.50 \pm 0.17) \times 10^{-3}$ [11], we obtain

$$\mathrm{BR}(B^0 \to J/\psi K^{*0}\pi^+\pi^-) = (8.0 \pm 2.2 \pm 1.5) \times 10^{-4} \tag{5.4}$$

5.1.6 $B^0 \to J/\psi K^{*0}\pi^+\pi^-$ Submodes

As mentioned in section 5.1.1, several decay modes could contribute to $B^0 \to J/\psi K^{*0}\pi^+\pi^-$. Figure 5.5 shows the $J/\psi\pi^+\pi^-$ invariant mass distribution with 9 $\psi(2S)$ candidates on an expected background of 3 events. In comparison to the signal of 36 candidates, this is a $\sim 20\%$ contribution. The background shown in figure 5.5 is estimated by normalizing the $m(J/\psi\pi^+\pi^-)$ distribution of the sidebands.

Figure 5.6 shows the $K^{*0}\pi^+\pi^-$ mass distribution to search for resonant contributions such as $B^0 \to J/\psi(K_2^*(1430) \to K^{*0}\pi^+\pi^-)$. There is no evidence for a $K_2^*(1430)$ contribution. There is a small peak near 1.3 GeV but there is no known resonance at that mass which decays to $K^{*0}\pi^+\pi^-$. The probability of a fluctuation of that size occurring somewhere within this plot is $\sim 1.5\%$. Although this excess could be a new K^* resonance, it would be surprising if such a resonance had not been found by previous experiments. We conclude that we find no distinctly identifiable $K^{*0}\pi^+\pi^-$ resonant structure.

Figures 5.7, 5.8, and 5.9 show the $K^{*0}\pi^+\pi^-$ Dalitz plot and its projections. Without tagging the B flavor, there is an inherent ambiguity in which pion should be associated with the K^{*0}; in these Dalitz plots both $K^{*0}\pi^\pm$ combinations are shown.

The peak in figure 5.8 near $m^2(\pi^+\pi^-) = 0.9$ is an artifact of a few events which each have multiple K^{*0} candidates with the same $\pi^+\pi^-$ combination. The Dalitz

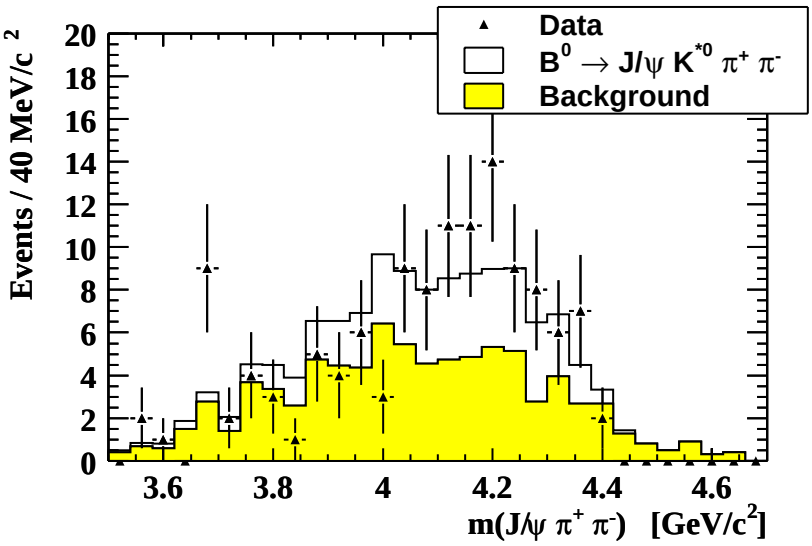

Figure 5.5: $m(J/\psi\pi^+\pi^-)$ for $B^0 \to J/\psi K^{*0}\pi^+\pi^-$ candidates showing a $\psi(2S)$ contribution plus contributions from higher $J/\psi\pi^+\pi^-$ invariant masses. The points represent the data; the filled histogram shows the expected background from normalizing the sideband distribution. The open histogram shows the background plus the expected $B^0 \to J/\psi K^{*0}\pi^+\pi^-$ signal (taken from Monte Carlo, normalized to the measured signal size), excluding the $\psi(2S)$ contribution. There are nine $\psi(2S) \to J/\psi\pi^+\pi^-$ candidates on an expected background of approximately three.

projections show the excess of the signal over background but the shape of the distributions is consistent with $B^0 \to J/\psi K^{*0}\pi^+\pi^-$ non-resonant Monte Carlo which have distributions of similar shape to the backgrounds shown. Specifically, figure 5.8 does not show evidence for a large contribution of $B^0 \to J/\psi K^{*0}\rho^0$ to $B^0 \to J/\psi K^{*0}\pi^+\pi^-$. Figure 5.9 shows a possible $K_1(1270)^+ \to K^{*0}\pi^+$ contribution although the excess is lower in mass and narrower than would be expected from $K_1(1270)^+$. The excess is around 1.45 ± 0.05 GeV/c^2 while a $K_1(1270)^+$ would contribute around 1.6 ± 0.1 GeV/c^2.

From these plots we conclude that we see no evidence for identifiable substructure in $B^0 \to J/\psi K^{*0}\pi^+\pi^-$ other than a few $B^0 \to \psi(2S)K^{*0}$ candidates. The data are consistent with coming dominantly from non-resonant $B^0 \to J/\psi K^{*0}\pi^+\pi^-$ decays.

5.2 $B^0 \to J/\psi K^0_S\pi^+\pi^-$

5.2.1 Overview

Like $B^0, \bar{B}^0 \to J/\psi K^0_S$, both B^0 and $\bar{B}^0$ can decay to the final state $J/\psi K^0_S\rho^0$, allowing CP violation due to interference between mixed and unmixed decays. The

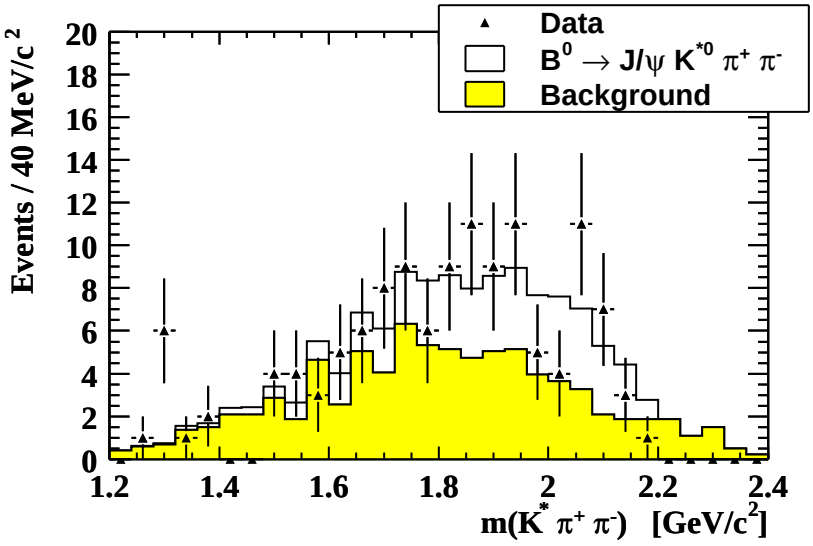

Figure 5.6: $m(K^{*0}\pi^+\pi^-)$ for $B^0 \to J/\psi K^{*0}\pi^+\pi^-$ candidates. The points represent the data; the filled histogram shows the expected background from normalizing the sideband distribution. The open histogram shows the background plus the expected $B^0 \to J/\psi K^{*0}\pi^+\pi^-$ signal (taken from Monte Carlo, normalized to the measured signal size). There is a small peak near 1.3 GeV/c^2 but there are no known $K^{*0}\pi^+\pi^-$ resonances near that mass. The probability of a fluctuation of that size occurring in at least one bin of this plot is $\sim 1.5\%$.

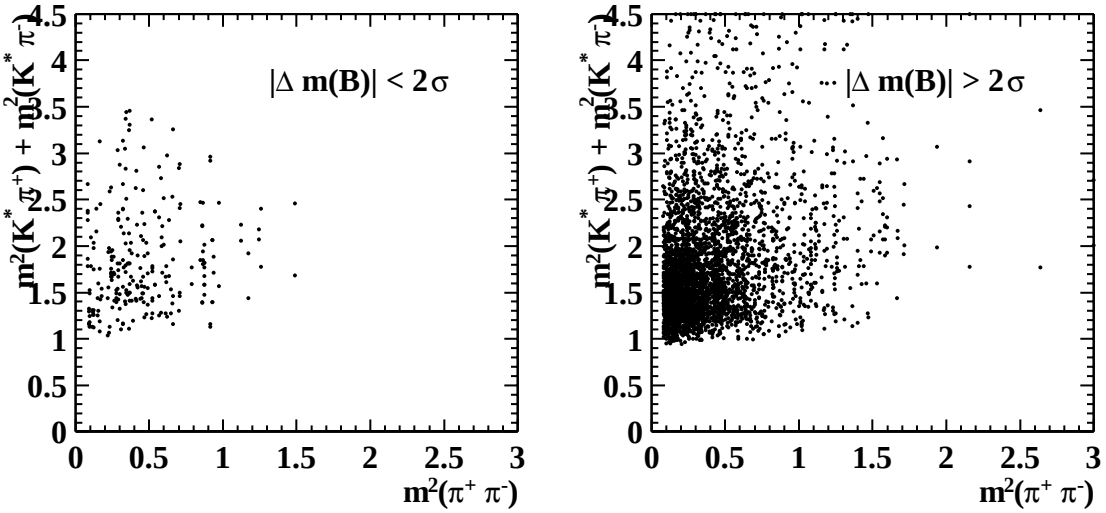

Figure 5.7: $K^{*0}\pi^+\pi^-$ Dalitz plot for $B^0 \to J/\psi K^{*0}\pi^+\pi^-$ candidates. The signal events within $\pm 2\sigma$ of the B mass are shown on the left; the background events from the sidebands are shown on the right.

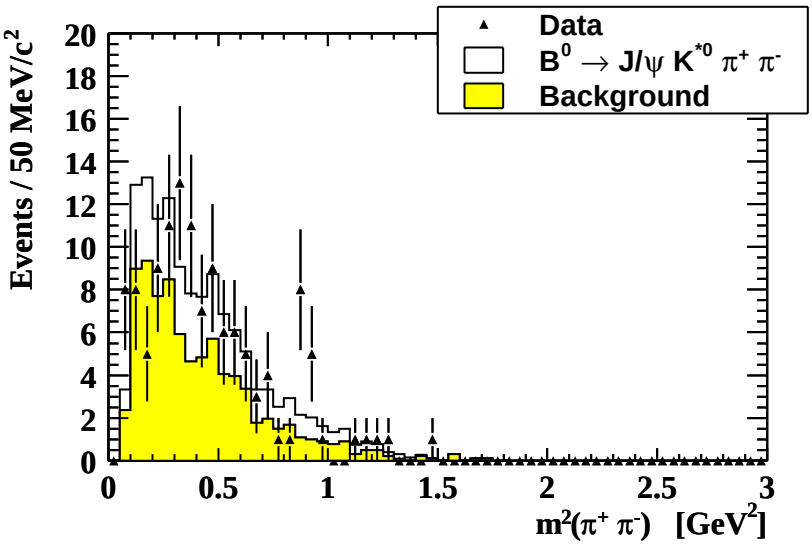

Figure 5.8: $m^2(\pi^+\pi^-)$ for $B^0 \to J/\psi K^{*0}\pi^+\pi^-$ candidates. The points represent the data; the filled histogram shows the expected background from normalizing the sideband distribution. The open histogram shows the background plus the expected $B^0 \to J/\psi K^{*0}\pi^+\pi^-$ signal taken from Monte Carlo, normalized to the measured signal size. The bump at $m^2 \approx 0.9$ is an artifact of two events which have multiple K^{*0} candidates with the same $\pi^+\pi^-$ combination. Although the signal has a slightly higher $m^2(\pi^+\pi^-)$ distribution than the background, it does not show evidence of any known $\pi^+\pi^-$ resonant structure. The data are consistent with non-resonant $B^0 \to J/\psi K^{*0}\pi^+\pi^-$ decays.

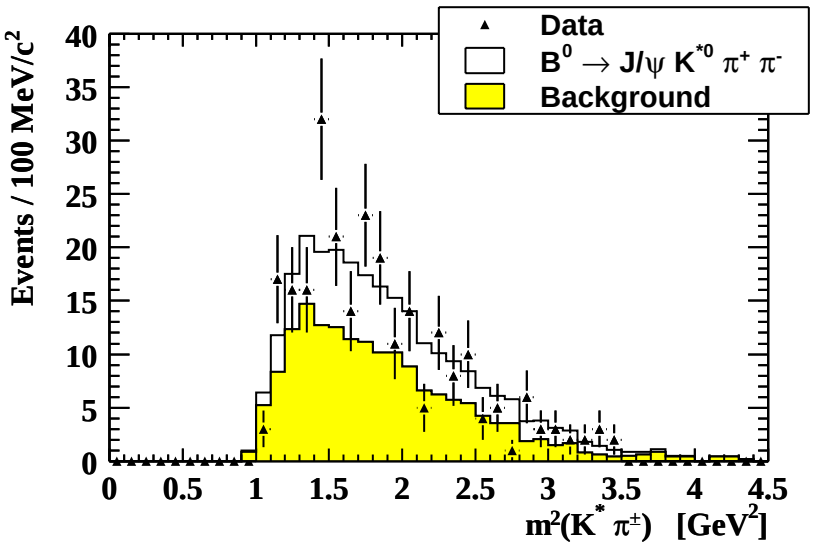

Figure 5.9: $m^2(K^{*0}\pi)$ for $B^0 \to J/\psi K^{*0}\pi^+\pi^-$ candidates. The points represent the data; the filled histogram shows the expected background from normalizing the sideband distribution. The open histogram shows the background plus the expected $B^0 \to J/\psi K^{*0}\pi^+\pi^-$ signal taken from Monte Carlo, normalized to the measured signal size. The excess at 1.45 possibly comes from $K_1(1270)^+$, but is too low in mass and narrower than would be expected from $K_1(1270)^+$. The data are consistent with non-resonant $B^0 \to J/\psi K^{*0}\pi^+\pi^-$ decays.

$V_{\rm CKM}$ elements of $B^0 \to J/\psi K^0_S \rho^0$ and $B^0 \to J/\psi K^0_S$ are the same, with both modes having a weak phase of -2β due to $B^0 \leftrightarrow \bar{B}^0$ mixing. Unlike $B^0 \to J/\psi K^0_S$, however, $J/\psi K^0_S \rho^0$ is not a CP eigenstate and thus both CP-even and CP-odd terms contribute.

Reference [33] describes how to use an angular analysis of the decay products to separate the CP-even and CP-odd contributions to make a measurement of the CP violating weak phase. Of particular importance are the cross terms between the CP-even and -odd contributions to the angular distributions of the final state particles. In this case, the cross terms are proportional to $\cos(2\beta)$. The value of $\sin(2\beta)$ will be well measured with $B^0 \to J/\psi K^0_S$. Unfortunately, a measurement of $\sin(2\beta)$ involves a four-fold trigonometric discreet ambiguity on the value of β which is the parameter of interest for testing the Standard Model. A measurement of $\cos(2\beta)$ would allow a resolution of two of the four discreet ambiguities. Even the sign of $\cos(2\beta)$ would be sufficient to resolve these, thus a precise measurement of $\cos(2\beta)$ is not necessary.

An additional complication is that the terms proportional to $\cos(2\beta)$ also have a factor of $\cos\delta$ where δ is a strong phase arising from final state interactions. In the factorization hypothesis, this phase is 0 and the sign of $\cos(2\beta)$ can be determined from a $\cos\delta\cos(2\beta)$ measurement. But if factorization is not a valid hypothesis, $\cos\delta$ could be either positive or negative and the sign of $\cos(2\beta)$ would remain unknown.

Before any conclusions may be drawn about $\cos(2\beta)$ from a measurement such as this, an independent confirmation of the factorization hypothesis will be necessary. The factorization hypothesis may be tested in other color-suppressed decay modes such as $B^0 \to J/\psi K^{*0}$ and $B_s \to J/\psi\phi$ [34] or in non-CP-violating iso-spin related modes such as $B^+ \to J/\psi K^{*+}\rho^0$.

A Feynman diagram for $B^0 \to J/\psi K^0_S \rho^0$ is shown in at the top of figure 5.10. Experimentally, $J/\psi \to \mu^+\mu^-$ and $K^0_S \to \pi^+\pi^-$ are readily identified since the J/ψ has a narrow mass peak with high p_T muons and the K^0_S produces a narrow mass peak with a displaced vertex due to the K^0_S lifetime ($c\tau = 2.68$ cm). $\rho^0 \to \pi^+\pi^-$ is harder to uniquely identify due to the broad width of the resonance: the full width at half max is 150 MeV/c^2, centered at 770 MeV/c^2. Table 5.4 lists other resonances which also decay to $\pi^+\pi^-$ although their higher masses and spin states could suppress their contribution.

Resonance	Mass [MeV/c^2]	Γ [MeV/c^2]	BR($\to \pi^+\pi^-$) [%]
$\rho(770)$	769.3	150.2	~ 100
$f_0(980)$	980	40 – 100	~ 66
$f_2(1270)$	1275.4	185.1	56.5

Table 5.4: Resonant decay modes to $\pi^+\pi^-$.

Figure 5.10 (bottom) shows the Feynman diagram for another decay which pro-

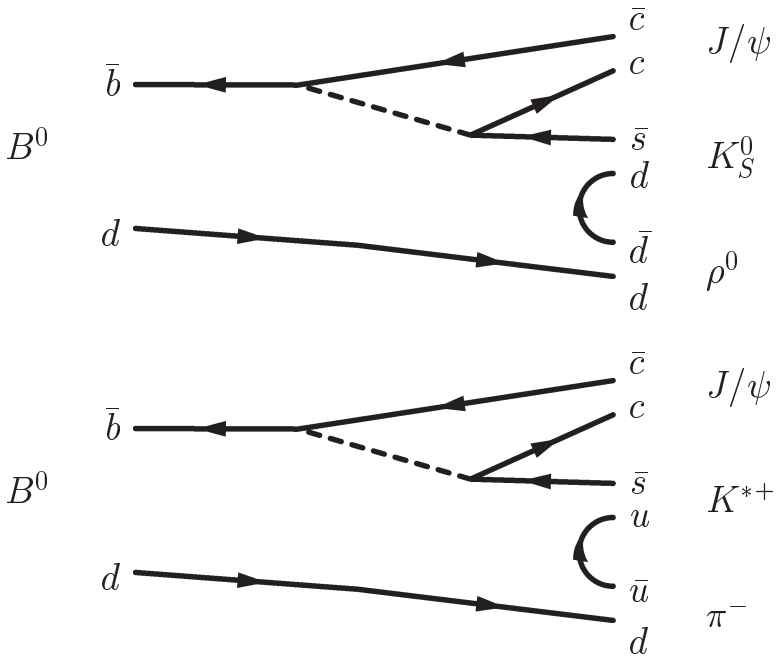

Figure 5.10: Feynman diagrams for $B^0 \to J/\psi K^0_S \rho^0$ (top) and $B^0 \to J/\psi K^{*+}\pi^-$ (bottom). Both produce $J/\psi K^0_S \pi^+\pi^-$.

duces $J/\psi K^0_S \pi^+\pi^-$: $B^0 \to J/\psi K^{*+}\pi^-$, with $K^{*+} \to K^0_S\pi^+$. Although the $K^0_S\pi^+$ forms a resonance in this case, the $\pi^+\pi^-$ mass has considerable overlap with the ρ^0 mass region. Figure 5.11 shows the $K^0_S\pi^+\pi^-$ Dalitz plots of $m^2(K^0_S\pi)$ *vs.* $m^2(\pi^+\pi^-)$ for a Monte Carlo simulation of $B^0 \to J/\psi K^{*+}\pi^-$ (left) and $B^0 \to J/\psi K^0_S\rho^0$ (right). Without knowing the B flavor one cannot know which pion to combine with the K^0_S, thus both $K^0_S\pi^\pm$ assignments are shown in the Dalitz plots. The effect of using both $K^0_S\pi^\pm$ assignments is evident in the left plot: the correct assignment produces an enhancement along the $K^{*\pm}$ mass region while the incorrect assignment is evenly distributed throughout the rest of the Dalitz plot.

Table 5.5 lists other possible kaon resonances which decay to $K^0_S\pi^\pm$. As with the higher $\pi^+\pi^-$ resonances, the higher masses and spin states of these resonances would tend to suppress their contribution.

In addition to the Feynman diagrams shown above for $B^0 \to J/\psi K^{*+}\pi^-$ and $B^0 \to J/\psi K^0_S\rho^0$, both $K^{*+}\pi^-$ and $K^0_S\rho^0$ could be produced from the decay of a higher kaon resonance such as $B^0 \to J/\psi K_1(1270)$. Possibilities such as this are listed in table 5.6. The Belle experiment has reported a preliminary observation of $B \to J/\psi K_1(1270)$ [35] but the other modes have not been observed.

Additionally, the decays $K_1(1270)^0 \to K^*_0(1430)^+\pi^-$, $K^*_0(1430)^+ \to K^0_S\pi^+$ and $K_2(1770)^0 \to K^*_2(1430)^+\pi^-$, $K^*_2(1430)^+ \to K^0_S\pi^+$ could produce $K^0_S\pi^+\pi^-$. Finally, the decay $B^0 \to \psi(2S)K^0_S$, $\psi(2S) \to J/\psi\pi^+\pi^-$ also produces the final state

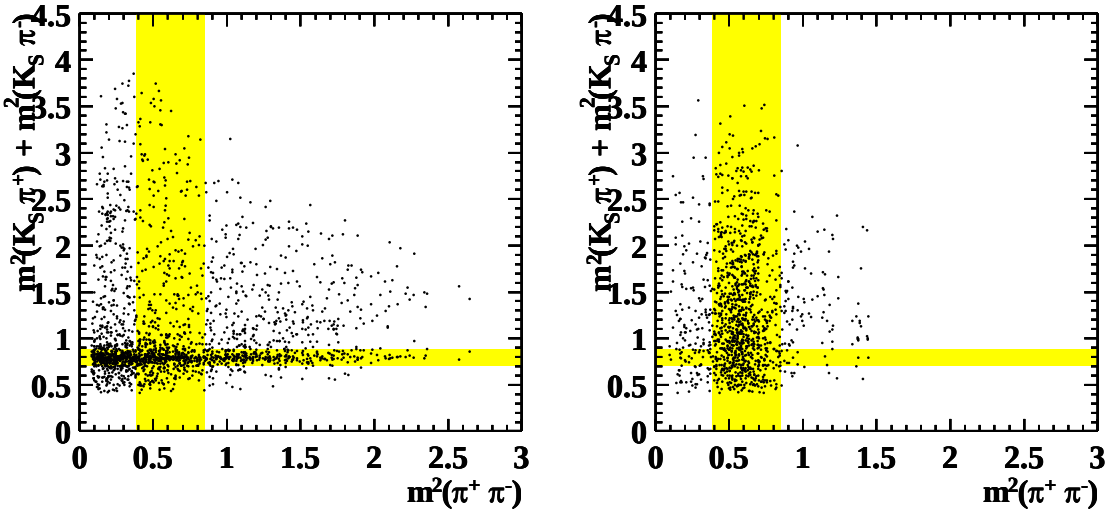

Figure 5.11: Dalitz plots for Monte Carlo $B^0 \to J/\psi K^{*+}\pi^-$ (left) and $B^0 \to J/\psi K^0_S \rho^0$ (right) signals.

Resonance	Mass [MeV/c^2]	Γ [MeV/c^2]	BR($\to K^0_S\pi^+$) [%]
$K^*(892)$	891.66	50.8	~ 33
$K^*(1410)$	1414	232	22
$K^*_0(1430)$	1412	294	31
$K^*_2(1430)$	1425.6	98.5	16.6
$K^*(1680)$	1717	322	12.9
$K^*_3(1780)$	1776	159	6.3
$K^*_4(2045)$	2045	198	3.3

Table 5.5: Resonant kaon decay modes to $K^0_S\pi^+$.

$J/\psi K^0_S\pi^+\pi^-$.

Thus there are a considerable number of possibilities for a B^0 decay to produce a J/ψ, a K^0_S, and two pions. The $\psi(2S)$ contribution is a narrow resonance at 3.686 GeV/c^2 which is easily identified by looking at $m(J/\psi\pi^+\pi^-)$. $m(K^0_S\pi^+\pi^-)$ provides some information about the kaon resonances of table 5.6, although a full Dalitz plot analysis would be necessary to differentiate different spin states at similiar masses. A Dalitz plot of $m^2(K^0_S\pi^\pm)$ *vs.* $m^2(\pi^+\pi^-)$ provides information to differentiate the $K^* \to K^0_S\pi$ contributions of table 5.5 from the $\rho, f \to \pi^+\pi^-$ resonances of table 5.4, with $K^*(892)^+$ and $\rho(770)^0$ being the expected largest contributions. Fully separating

Resonance	Mass [MeV/c^2]	Γ [MeV/c^2]	BR($\to K^{*+}\pi^-$) $\times$ BR($K^{*+} \to K^0_S\pi^+$) [%]	BR($\to K^0_S\rho^0$) [%]
$K_1(1270)$	1273	90	3.6	7
$K_1(1400)$	1402	174	21	0.5
$K^*(1410)$	1414	232	> 8.9	< 1
$K^*_2(1430)$	1425.6	98.5	5.49	1.5
$K^*(1680)$	1717	322	6.64	5.23
$K^*_3(1780)$	1776	159	4.4	5.2

Table 5.6: Resonant kaon decay modes to $K^0_S\pi^+\pi^-$ via $K^{*+}\pi^-$ or $K^0_S\rho^0$.

all of these possible contributions would require a considerable amount of data,[3] but even with a small number of events these various mass projections and Dalitz plots provide hints of the situation.

In order to search for these decays, we reconstruct $B^0 \to J/\psi K^0_S\pi^+\pi^-$ candidates and optimize cuts on this sample and then consider regions of the $K^0_S\pi^+\pi^-$ Dalitz plot to extract submode contributions.

5.2.2 Reconstruction and Cut Optimization

We search for $B^0 \to J/\psi K^0_S\pi^+\pi^-$ in a manner similar to that used for $B^0 \to J/\psi K^{*0}\pi^+\pi^-$. To reduce backgrounds, we require $m^2(\pi^+\pi^-) > 0.3$ (GeV/c^2)^2 while optimizing the cuts $ct(B)$, $p_T(K^0_S)$, and Iso(B) using $B^0 \to J/\psi K^0_S$ as the reference signal.

The $J/\psi K^0_S\pi^+\pi^-$ dataset has inherently less background than $J/\psi K^{*0}\pi^+\pi^-$ since the K^0_S has a much narrower mass and an additionally displaced vertex in comparison to the K^{*0}. To take advantage of this smaller background, events which do not have enough SVX information to make a precise ct determination are included in a separate optimization which does not make the ct cut. Events which have SVX information for both muons[4] are optimized using a ct cut; the remaining events are optimized separately using only the $p_T(K^0_S)$ and Iso(B) cuts. The resulting optimized cuts for each sample are shown in table 5.7.

Figure 5.12 shows the resulting B^0 candidates' invariant mass peak. Fitting with a Gaussian of fixed width plus a linear background using a binned likelihood technique gives a signal of 21.0 ± 6.3 events with a $S/B = 1.0$ within $\pm 2\sigma$ of the B mass. The Monte Carlo signal width is $\sigma = 10.2$ MeV/c^2, however the reference mode ($J/\psi K^0_S$) data has a width that is 10.7% larger than its Monte Carlo width. Thus we scale the expected signal width in the data to $10.2 \cdot 1.107 = 11.3$ MeV/c^2 and use this value

[3] Hundreds of signal events would be required for a Dalitz plot fit of $K^*(892)^+$ and $\rho(770)^0$ including phase interference; thousands of signal events would be necessary to fit all possible contributions.

[4] Both muons are required to have SVX information since at least two tracks from the B decay vertex must have SVX information in order to precisely locate the decay vertex.

Cut	Minimum	Maximum	Step Size	Optimized Value SVX	Optimized Value non-SVX
$p_T(K^0_S)$	0.6 GeV/c	2.0 GeV/c	0.1 GeV/c	0.8 GeV/c	1.9 GeV/c
$ct(B)$	0 μm	200 μm	10 μm	30 μm	—
Iso(B)	0.40	0.80	0.05	0.60	0.70

Table 5.7: Optimized cuts for $B^0 \to J/\psi K^0_S \pi^+\pi^-$. The "SVX" column is for events which have enough SVX information to make a meaningful ct cut; the "non-SVX" column shows the optimized cuts for a separate optimization on the remaining $B^0 \to J/\psi K^0_S \pi^+\pi^-$ candidate events.

when fitting the data. Varying this width by $\pm 20\%$ produces less than a 2% change in the fitted signal size so the exact choice is relatively unimportant. When the same cuts are applied to the reference signal of $B^0 \to J/\psi K^0_S$ there are 84.1 ± 9.9 signal events.

Within $\pm 2\sigma$ there are 39 events on an expected background of 21.05 events, corresponding to a Feldman Cousins[5] 95% confidence interval of $[7.1, 31.8]$ signal events.

5.2.3 Signal Peak Cross Checks

The signal peak in figure 5.12 is approximately a factor of 2 more narrow than expected. The events in the signal region were not used in the optimization of the cuts so it is unlikely that these events are simply an artifact of cut bias, but none-the-less we explore some other cuts to check if the signal peak is real.

Figure 5.13 shows the normalized mass $(m_B - 5.28)/\sigma_{m_B}$. An unbinned likelihood fit to the normalized mass data produces a width of 0.67 and a bias of -0.64. The fitted number of events 16.2 ± 5.6 is smaller than but consistent with the fit to the non-normalized mass.

Figure 5.14 shows the mass peak with the looser cuts of $p_T(K^0_S) > 1.0$ GeV/c, Iso(B) > 0.5, and $ct > 0$ μm for events in the SVX sample while requiring either a K^{*+} or ρ^0 candidate[6] in order to control the backgrounds. Varying the cuts consistently results in a Gaussian-like excess of events around the B^0 mass although the peak is usually narrower by a few MeV/c^2 than expected from Monte Carlo.

Figure 5.15 shows the mass distribution of events within the four central signal bins between 5.26 and 5.30 GeV/c^2.

The excess of events in the signal region is robust over a wide range of cuts and

[5]The Feldman Cousins method [37] of setting confidence limits is a classical (*i.e.*, non-Bayesian) approach to setting confidence intervals which has the primary benefit of providing a smooth transition from the case of an upper limit to that of a confidence interval which excludes 0.

[6]A K^{*+} candidate has an invariant mass within 892 ± 51 MeV/c^2; a ρ^0 candidate has invariant mass within 770 ± 150 MeV/c^2.

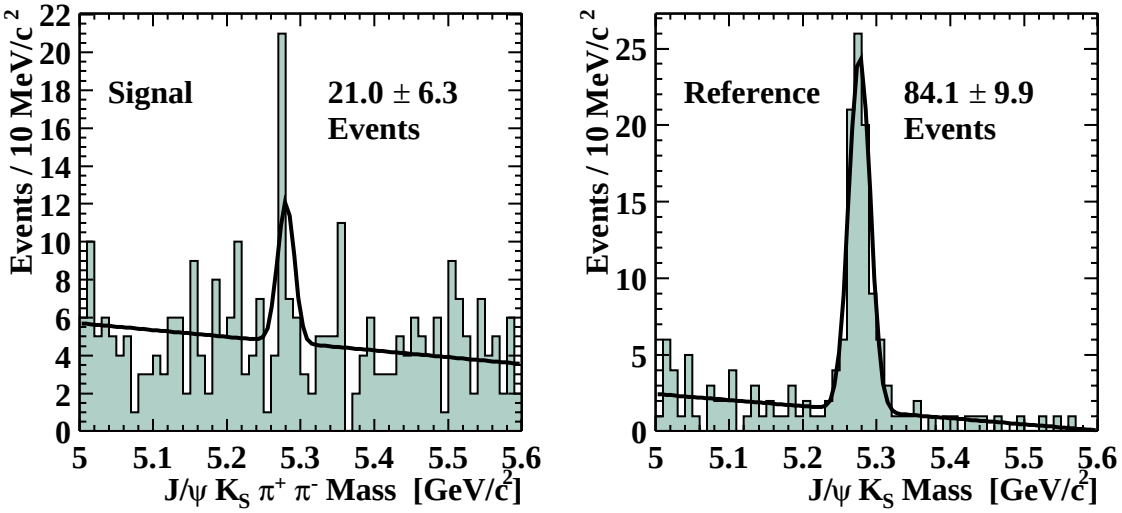

Figure 5.12: Mass distribution of $B^0 \to J/\psi K^0_S \pi^+\pi^-$ candidates (left) with optimized cuts. The mass peak of the reference mode $B^0 \to J/\psi K^0_S$ with the same cuts is shown on the right.

appears to be free of pathologies other than the unexpectedly narrow width. *E.g.*, the events are distributed about the $K^0_S\pi^+\pi^-$ Dalitz plot and have expected distributions of $p_T(K^0_S)$, $ct(B)$, and Iso(B). Thus we conclude that the signal peak is real and that its narrowness is likely simply due to a statistical fluctuation.

Another possibility we checked is that of obtaining a fake peak via a reflection from another mode with similar topology: *e.g.* reconstructing $B_s \to J/\psi K^0_S K^{*0}$ as $B^0 \to J/\psi K^0_S \rho^0$ by misidentifying the K^+ from the K^{*0} as a π^+ and having the resulting $\pi^+\pi^-$ mass end up within the large ρ^0 mass window. To check this possibility, we generated Monte Carlo samples for various modes and tried mis-reconstructing them as $B^0 \to J/\psi K^0_S \rho^0$. Figure 5.16 shows the results. Although the reflected peak is on top of the B^0 mass region, it is considerably wider than the expected B^0 peak and has a lower reconstruction efficiency than the genuine signal. If the $B_s \to J/\psi K^0_S K^{*0}$ signal was observed to be quite large, this could be an important contribution to the background. But for all of the modes studied, their observed signal size is small enough that they form a negligible contribution to the backgrounds of the other modes when mis-reconstructed as a reflection.

5.2.4 Ratio of Efficiencies

In order to extract branching ratios from the observed number of events, the ratio of efficiencies between the signal and reference modes must be determined. These efficiencies must include all efficiencies of trigger, geometric/kinematic acceptance,

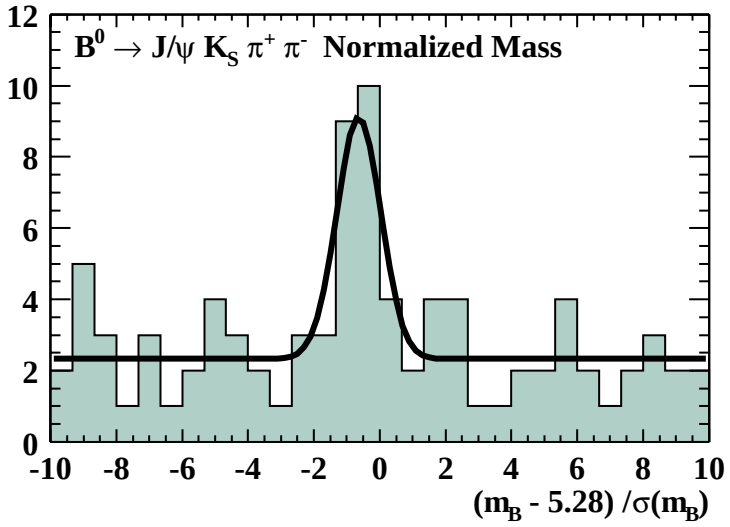

Figure 5.13: Normalized $B^0 \to J/\psi K^0_S \pi^+\pi^-$ mass. An unbinned likelihood fit indicates a width of 0.67.

reconstruction, and final cuts. We estimate these using a Monte Carlo dataset as described in chapter 4. For the signal Monte Carlo dataset we use a combination of 8 million $B^0 \to J/\psi K^0_S \rho^0$ decays, 7 million $B^0 \to J/\psi K^{*+}\pi^-$ decays, and 2.3 million $B^0 \to J/\psi K^*(1430)^+\pi^-$ decays. All of the modes have similar reconstruction efficiencies so the exact composition is not crucial and any deviation will be included as a systematic uncertainty.

The efficiencies for each step of the reconstruction (discussed in detail in section 5.1.3) are listed in table 5.8. The resulting ratio of efficiencies is $\epsilon_{ref}/\epsilon_{sig} = 0.436\%/0.0876\% = 4.98$.

Step	$B^0 \to J/\psi K^0_S \pi^+\pi^-$	$\epsilon(\%)$	$B^0 \to J/\psi K^0_S$	$\epsilon(\%)$
Events Generated	17,300,000	—	1,000,000	—
Basic Acceptance	595,716	3.4	158,746	16
Dimuon Trigger	87,341	15	16,815	11
Track Quality	82,102	94	15,405	92
Decay Reconstruction	23,310	28	5791	38
Final Cuts	$16,530 \pm 129$	71	5068 ± 71	88
Isolation Efficiency Corr.	—	—	—	86
Tracking Efficiency Corr.	—	92	—	—
Total Efficiency		0.0876		0.436

Table 5.8: $B^0 \to J/\psi K^0_S \pi^+\pi^-$ reconstruction efficiencies

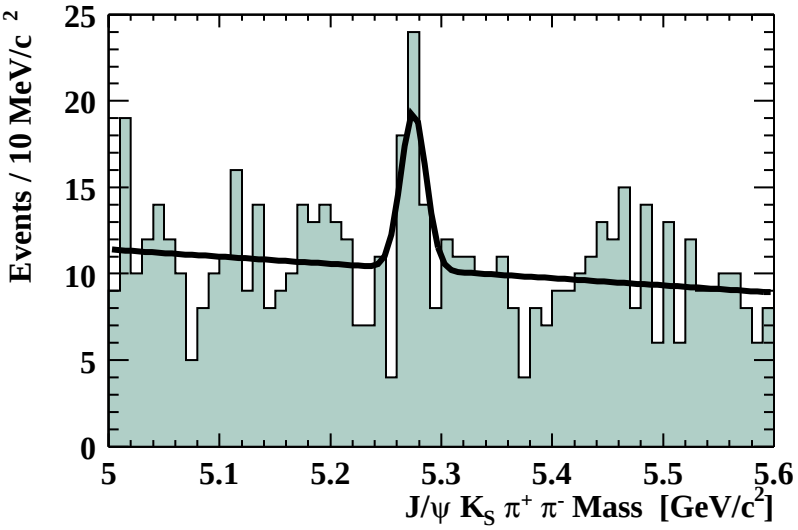

Figure 5.14: The B^0 candidate mass distribution for events with a K^{*+} or ρ^0 candidate with the loose cuts of $p_T(K^0_S) > 1.0$ GeV/c, Iso$(B) > 0.5$, and $ct > 0$ μm for events in the SVX sample.

5.2.5 Uncertainties

The dominant source of uncertainty is the statistical uncertainty on the signal data: $6.3/21.0 = 30\%$. Combining this with the statistical uncertainty on the reference sample size of $9.9/84.1 = 11.8\%$, the total statistical uncertainty is 32.2%.

The systematic uncertainties as described in section 4.5 are dominated by the reference mode branching ratio and the decay helicity model. We estimate the uncertainty due to the decay helicity model by separately modeling longitudinally and transversely polarized components of $B^0 \to J/\psi K^0_S \rho^0$. We find a 33% maximum spread in their efficiencies which when divided by $\sqrt{12}$ to get the RMS produces an uncertainty of 9.4%.

We estimate the effect of sample composition uncertainty by comparing the efficiencies of a pure $B^0 \to J/\psi K^0_S \rho^0$ Monte Carlo sample with that of a pure $B^0 \to J/\psi K^{*+}\pi^-$ sample. The RMS of this efficiency spread is 5%.

As mentioned in section 4.5, our trigger model of "volunteer" events adds an overall systematic uncertainty of 5%.

The effect of various B production models mostly cancels in the ratio between signal and reference mode efficiencies with a small uncertainty of 2.5%.

The uncertainty on the tracking efficiency correction is less than 2% and is neglected here. Likewise, even though there is some uncertainty on the signal width based upon the width discrepancy between the data and Monte Carlo for the reference modes, varying the width by $\pm 20\%$ affects the fitted signal size by less than 2%

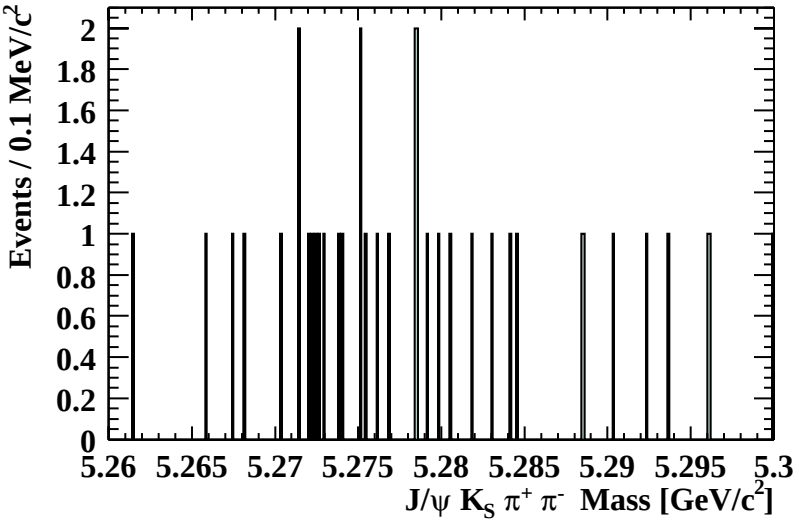

Figure 5.15: Mass distribution of $J/\psi K^0_S \pi^+\pi^-$ events between 5.26 and 5.30 GeV/c^2.

and thus this is neglected as a systematic uncertainty.

In summary, the uncertainties for measuring BR($B^0 \to J/\psi K^0_S \pi^+\pi^-$) are listed in table 5.9.

Statistical Uncertainty	%	Systematic Uncertainty	%
Signal Size	30.0	Reference BR	13.5
Reference Size	11.8	Helicity Model	9.4
		Trigger Model	5.0
		Sample Composition	5.0
		B Production Model	2.5
Combined Statistical Uncertainties	**32.2**	Combined Systematics	**18.1**
		Without ref. BR uncer.	**12.0**

Table 5.9: BR($B^0 \to J/\psi K^0 \pi^+\pi^-$) uncertainties

5.2.6 BR($B^0 \to J/\psi K^0 \pi^+\pi^-$)

Combining these results we obtain the ratio of branching ratios:

$$\frac{\mathrm{BR}(B^0 \to J/\psi K^0 \pi^+\pi^-)}{\mathrm{BR}(B^0 \to J/\psi K^0)} = \frac{N_{sig}}{N_{ref}} \cdot \frac{\epsilon_{ref}}{\epsilon_{sig}} \quad (5.5)$$

$$= \frac{21.0}{84.1} \cdot \frac{0.436}{0.0876} \quad (5.6)$$

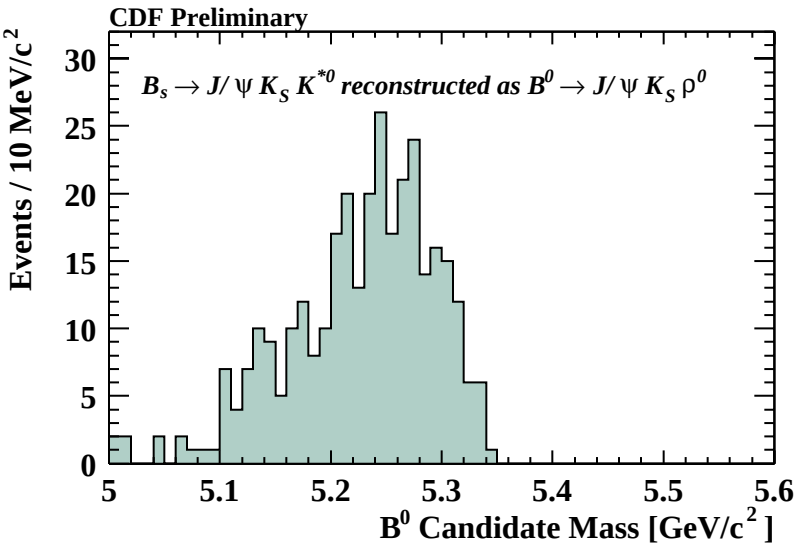

Figure 5.16: The B^0 candidate mass distribution when $B_s \to J/\psi K_S^0 K^{*0}$ is reconstructed as $B^0 \to J/\psi K_S^0 \pi^+\pi^-$.

$$= \quad 1.24 \pm 0.40 \pm 0.15 \tag{5.7}$$

where the first uncertainty is statistical and the second is systematic.

Using the reference mode branching ratio of $\mathrm{BR}(B^0 \to J/\psi K_S^0) = (8.9 \pm 1.2) \times 10^{-4}$ [11], we obtain:

$$\mathrm{BR}(B^0 \to J/\psi K^0 \pi^+\pi^-) = (1.1 \pm 0.4 \pm 0.2) \times 10^{-3} \tag{5.8}$$

5.2.7 Submode Contributions

As mentioned in section 5.2.1 there are many submodes which could contribute to $B^0 \to J/\psi K_S^0 \pi^+\pi^-$ with $B^0 \to J/\psi K_S^0 \rho^0$ and $B^0 \to J/\psi K^{*+}\pi^-$ as the largest expected contributors.

Figure 5.17 shows the $J/\psi\pi^+\pi^-$ mass distribution for events within $\pm 2\sigma$ of the B mass, *i.e.* $5.28 - 2 \cdot 0.0113 < m_{B^0} < 5.28 + 2 \cdot 0.0113$ GeV/c^2. There are a five $\psi(2S)$ candidates but the majority of the events come from a higher $J/\psi\pi^+\pi^-$ mass.

Figure 5.18 shows the $K_S^0\pi^+\pi^-$ mass distribution to search for $K_1(1270)$ or other higher resonant kaon contributions. There is a small excess at the $K_1(1270)$ mass but many of the candidate events are at a higher $K_S^0\pi^+\pi^-$ mass.

Dalitz plots of the data are shown in figure 5.19. The left plot shows the events within $\pm 2\sigma$ of the B mass while the right plot shows events from the sideband regions. The shaded regions highlight the ρ^0 mass region (770 ± 150 MeV/c^2) and the K^{*+} mass region (892 ± 51 MeV/c^2). The Dalitz plots do not have a sharp phase space boundary because of the variable J/ψ momentum. Without tagging the B^0 flavor,

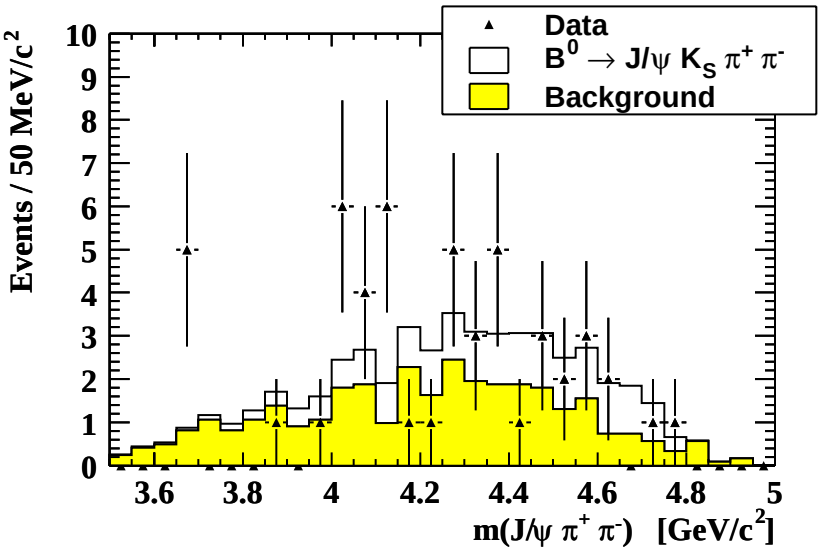

Figure 5.17: $m(J/\psi\pi^+\pi^-)$ for $B^0 \to J/\psi K^0_S\pi^+\pi^-$ candidates. The points represent the data; the filled histogram shows the expected background from normalizing the sideband distribution. The open histogram shows expected background plus the $B^0 \to J/\psi K^0_S\pi^+\pi^-$ signal (without the $\psi(2S)$ contribution) taken from Monte Carlo normalized to the measured signal size. There are five $\psi(2S) \to J/\psi\pi^+\pi^-$ candidates.

there is an inherent ambiguity in which of the pions should be combined with the K^0_S to form the $K^{*\pm}$ candidate and thus both combinations are shown in these plots.

Figures 5.20 and 5.21 show projections of the Dalitz plots. Figure 5.20 (top) shows the $m^2(\pi^+\pi^-)$ projection. The points represent the data within the B mass region and include both signal and background; the histogram shows the expected background shape and size taken from normalizing the $m^2(\pi^+\pi^-)$ distribution of the sidebands. The bottom histogram shows the shape of the $m^2(\pi^+\pi^-)$ distribution from a $B^0 \to J/\psi K^{*+}\pi^-$ Monte Carlo simulation while the curve shows the location of the ρ^0 Breit-Wigner resonance. The histogram and curve are *not* fits to the data; they have equal area and are shown only for qualitative shape and location comparison to the data. There is an excess of events over the background in the data within the ρ^0 mass region which likely indicates a $B^0 \to J/\psi K^0_S\rho^0$ contribution.

Figure 5.21 shows the equivalent plots for the $K^0_S\pi^\pm$ projection with an excess of events at the K^{*+} resonance. Since the background is strongly peaked at low $m^2(\pi^+\pi^-)$, this plot is only a partial projection, excluding events with $m^2(\pi^+\pi^-) < 0.3$ (GeV/c^2)^2. If this cut is not made, the excess at the K^{*+} mass is still present but the backgrounds are much larger making the excess less evident.

The $K^0_S\pi^+\pi^-$ Dalitz plot projections show evidence of $B^0 \to J/\psi K^0_S\rho^0$ and $B^0 \to J/\psi K^{*+}\pi^-$ contributions while the other plots indicate that the other possible contributions (*e.g.*, $\psi(2S)K^0_S$) are small. The Dalitz plot does not contain enough

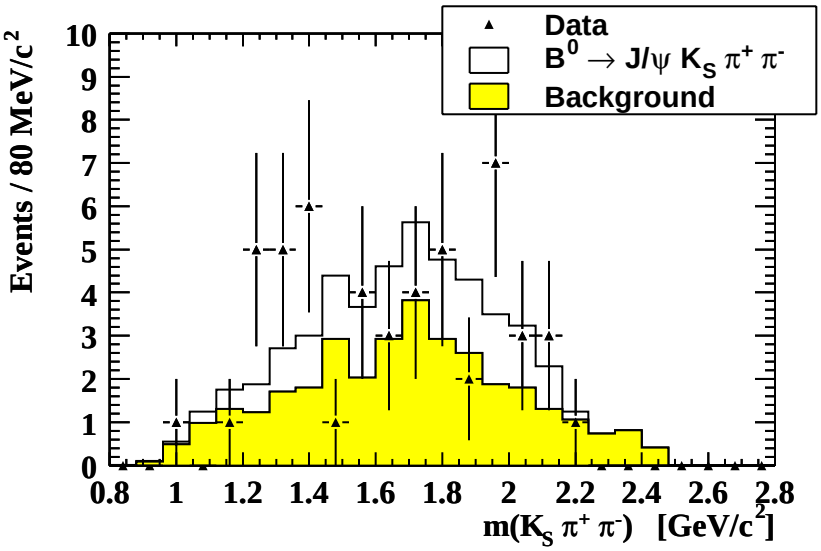

Figure 5.18: $m(K^0_S\pi^+\pi^-)$ for $B^0 \to J/\psi K^0_S\pi^+\pi^-$ candidates. The points represent the data; the filled histogram shows the expected background from normalizing the sideband distribution. The open histogram shows the expected background plus the $B^0 \to J/\psi K^0_S\pi^+\pi^-$ signal taken from Monte Carlo normalized to the measured signal size. There is an excess near the $K_1(1270)$ mass, but much of the excess appears at higher masses.

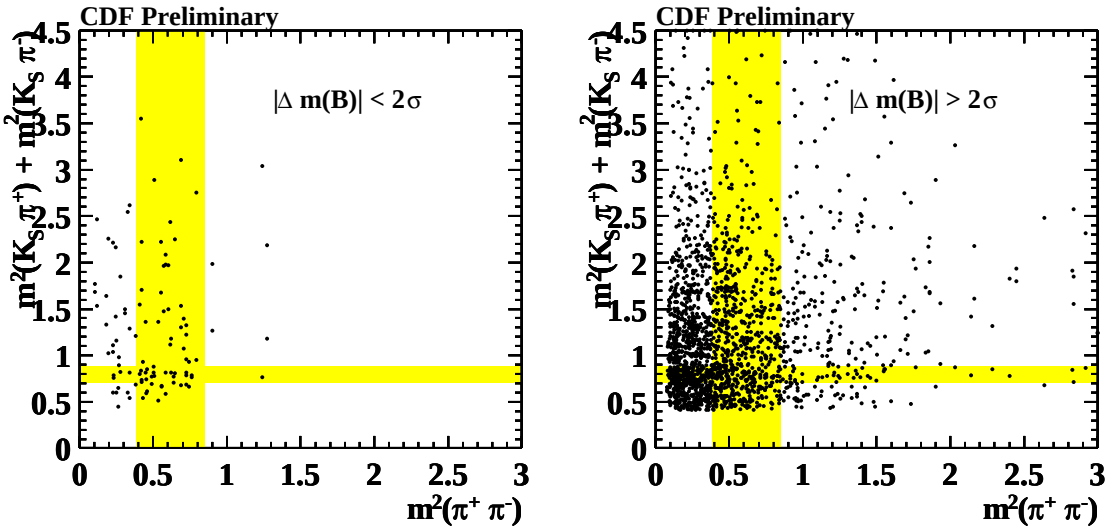

Figure 5.19: Combined Dalitz plots for $K^0_S\pi^+\pi^-$ with both $K^0_S\pi^\pm$ combinations. The left plot shows events within the B mass region while the right plot shows events from the B mass sidebands.

events to fit all possible contributions with all their degrees of freedom. None-the-less, some information may be extracted with a few assumptions. After vetoing the small number of $B^0 \to \psi(2S)K^0_S$ candidates, if we assume that the remaining contributions to the Dalitz plot are predominantly from $B^0 \to J/\psi K^0_S\rho^0$ and $B^0 \to J/\psi K^{*+}\pi^-$ and that they do not have any interference in their overlap region, the individual branching ratios may be extracted by considering the number of events in various subregions of the Dalitz plot and the efficiencies for the two signals in those regions.

A relatively pure $B^0 \to J/\psi K^0_S\rho^0$ sample may be obtained by considering the ρ^0 band of $m(\pi^+\pi^-)$ within 770 ± 150 MeV/c^2 while vetoing K^{*+} candidates with $m(K^0_S\pi)$ within 892 ± 51 MeV/c^2. Unfortunately a similar method does not work to produce a pure K^{*+} sample since vetoing ρ^0 candidates within the K^{*+} band would eliminate most of the K^{*+} signal as well.

Thus we consider two regions:

- Region X: $m(K^0_S\pi)$ within 892 ± 51 MeV/c^2 with no $m(\pi^+\pi^-)$ cuts.
- Region Y: $m(\pi^+\pi^-)$ within 770 ± 150 MeV/c^2 while vetoing events within region X.

Placing these cuts upon the Dalitz plot and fitting for the B mass peak in each region, we find the number of events in each region $N_X = 12.5\pm4.6$ and $N_Y = 8.5\pm3.8$ as shown in figure 5.22. Since these signals are small, we also consider the Feldman-Cousins 95% confidence intervals: For region X there are 21 events within $\pm2\sigma$

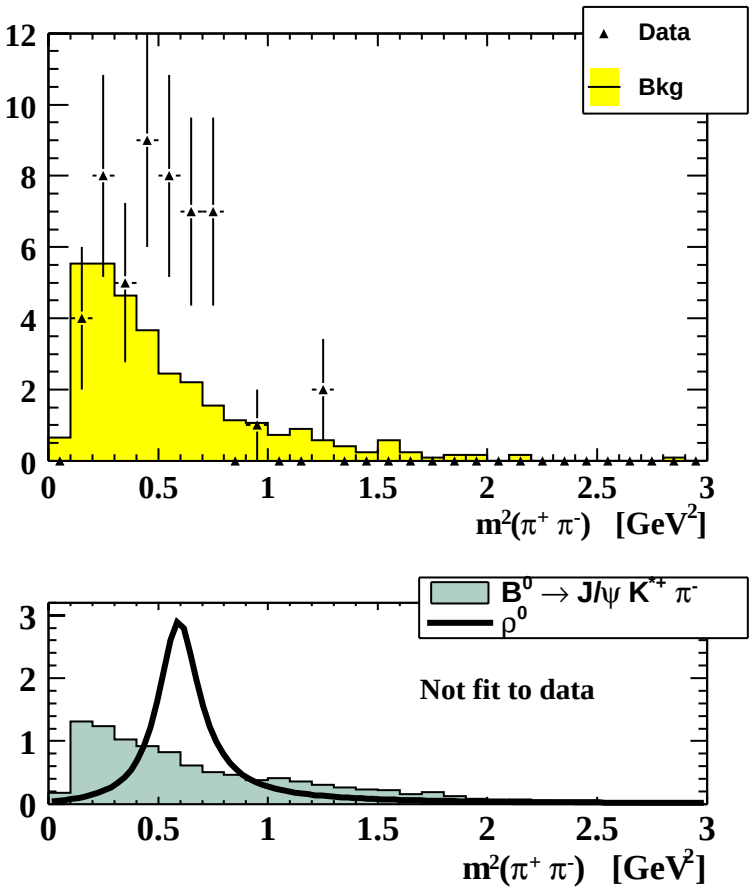

Figure 5.20: $m^2(\pi^+\pi^-)$ for $B^0 \to J/\psi K^0_S \pi^+\pi^-$ candidates (top). The points represent the data; the filled histogram shows the expected background from normalizing the sideband distribution. The bottom plot shows the shape of the $B^0 \to J/\psi K^{*+}\pi^-$ contribution to $m^2(\pi^+\pi^-)$ (histogram) and the location and width of the ρ^0 Breit-Wigner resonance (curve). The histogram and curve have equal area but they are *not* fits to the data. There is an excess of events at the ρ^0 mass indicating a possible $B^0 \to J/\psi K^0_S \rho^0$ contribution.

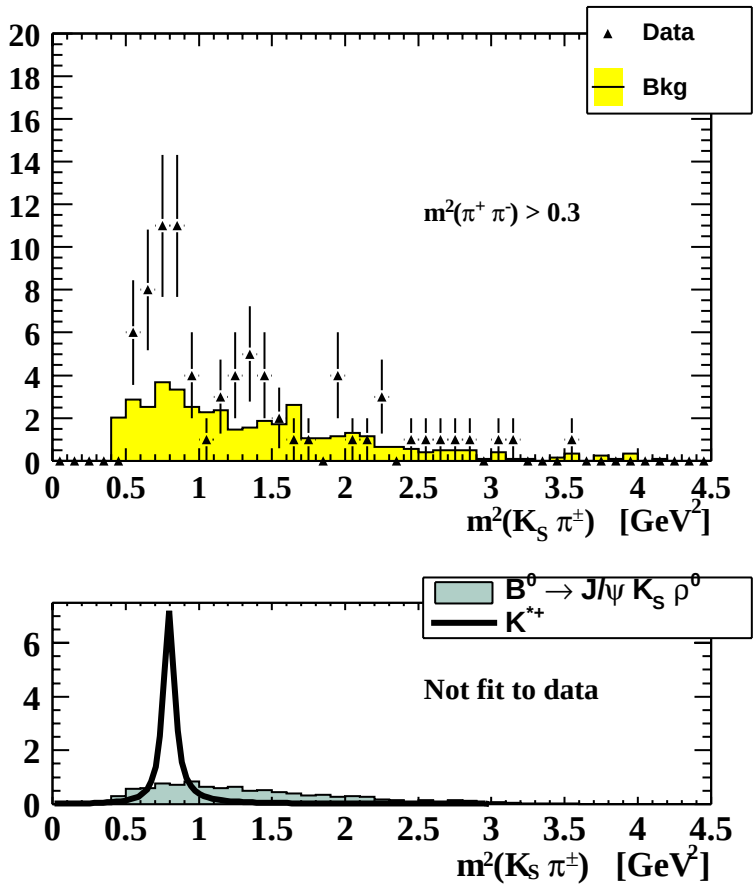

Figure 5.21: $m^2(K^0_S\pi^\pm)$ for $B^0 \to J/\psi K^0_S\pi^+\pi^-$ candidates (top). The points represent the data; the filled histogram shows the expected background from normalizing the sideband distribution. $m^2(\pi^+\pi^-) > 0.3$ $(\mathrm{GeV}/c^2)^2$ is required to reduce combinatoric backgrounds. The bottom plot shows the shape of the $B^0 \to J/\psi K^0_S\rho^0$ contribution to $m^2(K^0_S\pi^\pm)$ (histogram) and the location and width of the K^{*+} Breit-Wigner resonance (curve). The histogram and curve have equal area but they are *not* fits to the data. An excess of events from K^{*+} is evident.

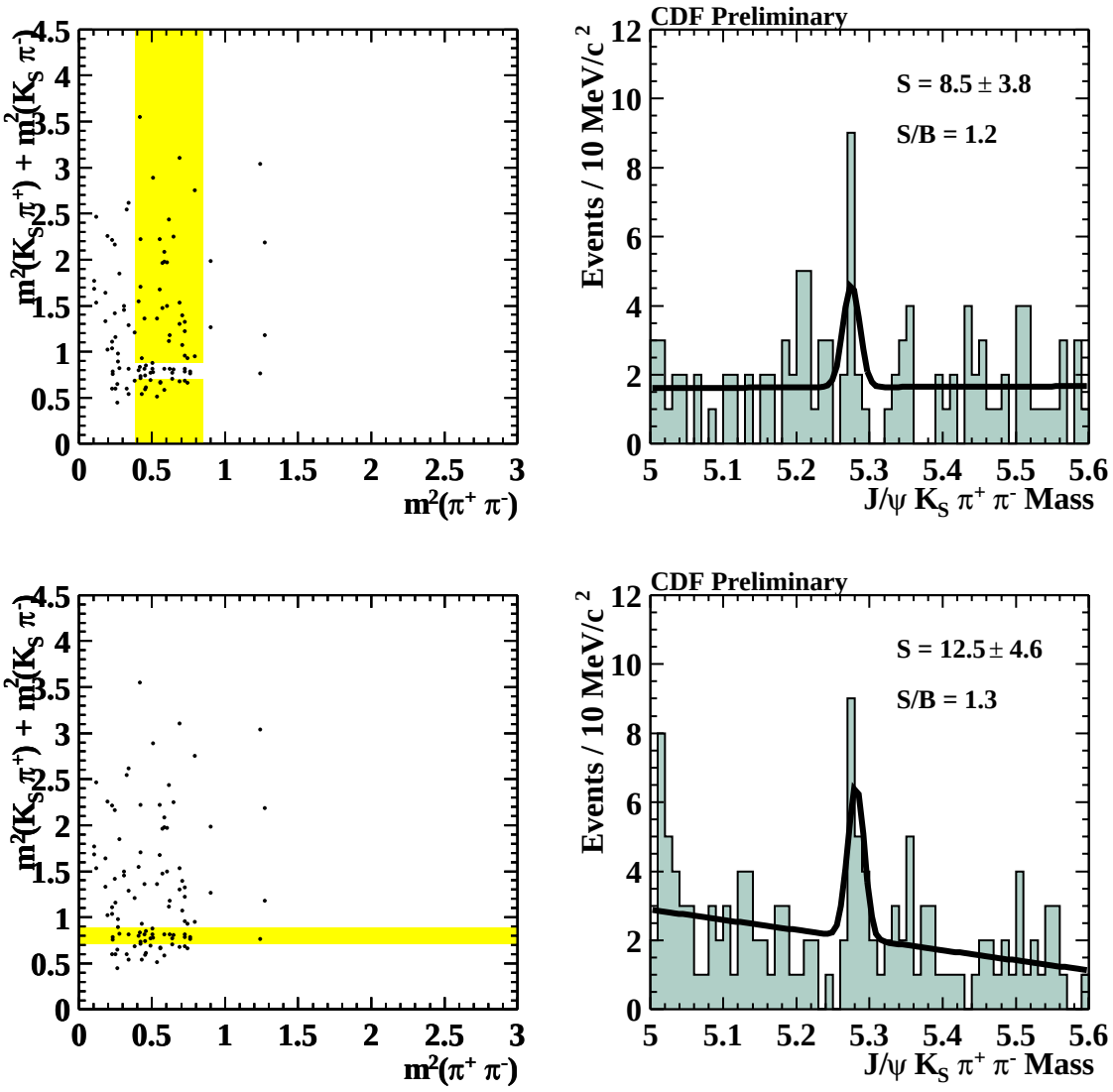

Figure 5.22: Mass peaks for $B^0 \to J/\psi K^0_S \rho^0$ candidates (upper right) and $B^0 \to J/\psi K^{*+}\pi^-$ candidates (lower right). The Dalitz plots on the left highlight the region selected for the corresponding mass plots.

($\pm 2 \cdot 11.3$ MeV/c^2) of the nominal B mass (5.28 GeV/c^2) with an expected background of 9.22 events. This corresponds to a 95% confidence interval on the signal size of $[4.09, 22.58]$. In region Y there are 14 events on a background of 7.32 for a 95% confidence interval of $[1.14, 15.62]$ signal events. Thus although these are small signals, they do exclude 0 at better than a 95% confidence level.

These numbers of events and the branching ratios and efficiencies of interest are related by:

$$\begin{pmatrix} N_X \\ N_Y \end{pmatrix} = \frac{N_{ref}}{\mathrm{BR}_{ref} \cdot \epsilon_{ref}} \begin{pmatrix} \epsilon_X^{\rho} & \epsilon_X^{K^*} \\ \epsilon_Y^{\rho} & \epsilon_Y^{K^*} \end{pmatrix} \begin{pmatrix} \mathrm{BR}(\rho) \\ \mathrm{BR}(K^*) \end{pmatrix} \tag{5.9}$$

where ϵ_X^{ρ} is the total efficiency for reconstructing $B^0 \to J/\psi K_S^0 \rho^0$ in region X; $\epsilon_Y^{K^*}$ is the total efficiency for reconstructing $B^0 \to J/\psi K^{*+} \pi^-$ in region Y, etc.; $\mathrm{BR}(\rho) = \mathrm{BR}(B^0 \to J/\psi K^0 \rho^0)$; and $\mathrm{BR}(K^*) = \mathrm{BR}(B^0 \to J/\psi K^{*+} \pi^-) \cdot \mathrm{BR}(K^{*+} \to K^0 \pi^+)$.

Using the Monte Carlo and $B^0 \to J/\psi K_S^0$ reference mode as before, we obtain:

- $N_{ref}/(\mathrm{BR}_{ref} \cdot \epsilon_{ref}) = 2.17 \times 10^7$
- $\epsilon_X^{\rho} = 2.42 \times 10^{-4}$
- $\epsilon_X^{K^*} = 7.89 \times 10^{-4}$
- $\epsilon_Y^{\rho} = 6.00 \times 10^{-4}$
- $\epsilon_Y^{K^*} = 0.795 \times 10^{-4}$

Solving this set of linear equations produces: $\mathrm{BR}(B^0 \to J/\psi K^0 \rho^0) = 5.81 \times 10^{-4}$ and $\mathrm{BR}(B^0 \to J/\psi K^{*+} \pi^-) = 8.30 \times 10^{-4}$. The systematic uncertainties are the same as described for $B^0 \to J/\psi K_S^0 \pi^+ \pi^-$ plus an additional 10% for the no interference assumption. Combining this with the uncertainties produces the results:

$$\mathrm{BR}(B^0 \to J/\psi K^0 \rho^0) = (5.8 \pm 3.1 \pm 1.2) \times 10^{-4} \tag{5.10}$$

$$\mathrm{BR}(B^0 \to J/\psi K^{*+} \pi^-) = (8.3 \pm 4.4 \pm 1.7) \times 10^{-4} \tag{5.11}$$

Although the number of signal events observed in each region are independent quantities, these branching ratios are correlated via the efficiency matrix of equation 5.9. This leads to a covariance matrix on the statistical uncertainties of the branching ratios:

$$\begin{pmatrix} \sigma_{11}^2 & \sigma_{12}^2 \\ \sigma_{12}^2 & \sigma_{22}^2 \end{pmatrix} = \begin{pmatrix} 9.42 \times 10^{-8} & -5.84 \times 10^{-8} \\ -5.84 \times 10^{-8} & 1.97 \times 10^{-7} \end{pmatrix} \tag{5.12}$$

where the subscript 1 refers to $\mathrm{BR}(B^0 \to J/\psi K^0 \rho^0)$ and subscript 2 refers to $\mathrm{BR}(B^0 \to J/\psi K^{*+} \pi^-)$. The correlation coefficient $\rho = \sigma_{12}^2/(\sigma_{11}\sigma_{22})$ is -0.43.

Figure 5.23 shows the resulting $m^2(\pi^+\pi^-)$ and $m^2(K_S^0\pi^\pm)$ distributions for the signal plus background (open histogram). The backgrounds are estimated from normalizing the sideband distributions. The signal shapes are taken from Monte Carlo and normalized to the measured $B^0 \to J/\psi K_S^0 \rho^0$ and $B^0 \to J/\psi K^{*+} \pi^-$ branching

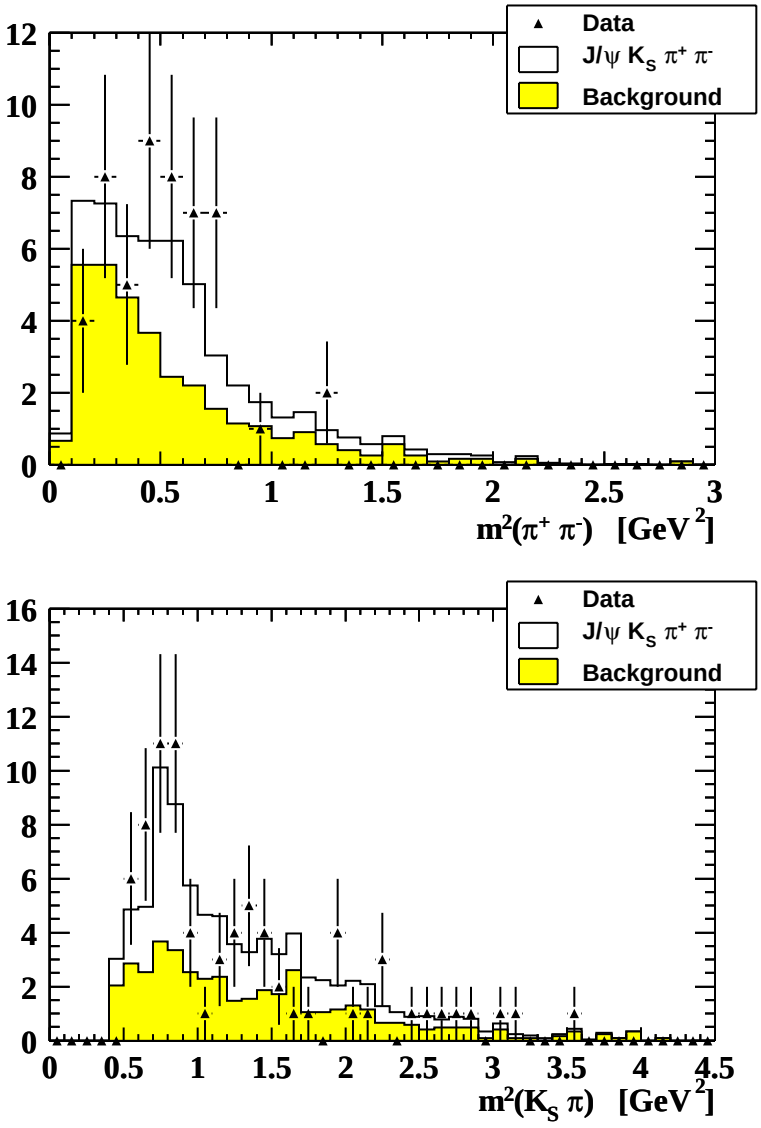

Figure 5.23: $m^2(\pi^+\pi^-)$ (top) and $m^2(K^0_S\pi^\pm)$ (bottom). The points show the data; the filled histogram shows the expected background from normalizing the sideband distribution. The open histogram shows the expected background plus the $B^0 \to J/\psi K^0_S\rho^0$ and $B^0 \to J/\psi K^{*+}\pi^-$ signals from Monte Carlo normalized to the measured signal sizes.

ratios. The points show the data in good agreement with the expected signal plus background shapes and sizes.

Comparing these submode branching ratios to the inclusive $B^0 \to J/\psi K^0_S \pi^+\pi^-$ branching ratio of 1.1×10^{-3} gives:

$$\begin{aligned} &\mathrm{BR}(B^0 \to J/\psi K^0 \rho^0) + \mathrm{BR}(B^0 \to J/\psi K^{*+}\pi^-) \times \mathrm{BR}(K^{*+} \to K^0\pi^+) && (5.13)\\ &= \; 5.8 \times 10^{-4} + 8.3 \times 10^{-4} \cdot 2/3 && (5.14)\\ &= \; 1.1 \times 10^{-3} && (5.15) \end{aligned}$$

Due to the $B^0 \to \psi(2S)K^0_S$ contribution, these submodes should sum to slightly less than the inclusive branching ratio, but these results are consistent with the inclusive branching ratio when considering the large statistical uncertainties on these measurements.

5.3 $B^0 \to J/\psi K^{(*)0}\pi^+\pi^-$ Conclusions

The most statistically significant signal, $B^0 \to J/\psi K^{*0}\pi^+\pi^-$, is a 3.7σ effect. It has an approximately 20% contribution from $B^0 \to \psi(2S)K^{*0}$ but other submode contributions are not identifiable with the current data. Specifically, we see no evidence for the quark popping mode $B^0 \to J/\psi K^{*0}\rho^0$.

$B^0 \to J/\psi K^0_S \pi^+\pi^-$ is a 3.3σ effect, however its unexpected narrowness warrants caution in interpreting the results. There is also an approximately 20% contribution from $\psi(2S)K^0_S$. The $\pi^+\pi^-$ and $K^0_S\pi^\pm$ mass distributions of figures 5.20 and 5.21 indicate contributions from $B^0 \to J/\psi K^0_S\rho^0$ and $B^0 \to J/\psi K^{*+}\pi^-$. With the current data we cannot distinguish whether these are genuine quark popping decays of table 2.1 or whether they proceed via a combination of the resonances listed in table 5.6, *e.g.* $B^0 \to J/\psi K_1(1270)$ with $K_1(1270) \to K^0_S\rho^0$ or $K^{*+}\pi^-$. We note, however, that the physics motivations for studying these final states are largely unchanged regardless of whether they are genuine quark popping decay modes or not.

Chapter 6

$B_s^0 \to J/\psi K^0 \pi^{\mp} K^{\pm}$

6.1 Overview

As discussed in section 2.7, B_s decay modes provide complementary information to the results obtained with B^0 decays. Of particular importance are B_s decays which are useful for measuring $B_s \leftrightarrow \bar{B}_s$ mixing and those which should have little or no CP violation within the Standard Model but could have CP violation in other models. Section 6.1.1 lists several quark popping modes which may be useful for such measurements. The details for extracting these measurements from the time dependent decay rates are given in section 6.1.2. The search results using the CDF Run I data are given in section 6.2, indicating that the branching ratios for these modes are likely too small to be very useful.

6.1.1 B_s Quark Popping Modes

Four B_s quark popping modes from table 2.1 which are potentially useful for B_s mixing or CP violation measurements are those which decay to $J/\psi K_S^0 \pi K$:

- $B_s \to J/\psi K^{*0} K_S^0$
  $\hookrightarrow K^+ \pi^-$
- $B_s \to J/\psi K_S^0 \bar{K}^{*0}$
  $\hookrightarrow K^- \pi^+$
- $B_s \to J/\psi K^{*+} K^-$
  $\hookrightarrow K_S^0 \pi^+$
- $B_s \to J/\psi K^+ K^{*-}$
  $\hookrightarrow K_S^0 \pi^-$

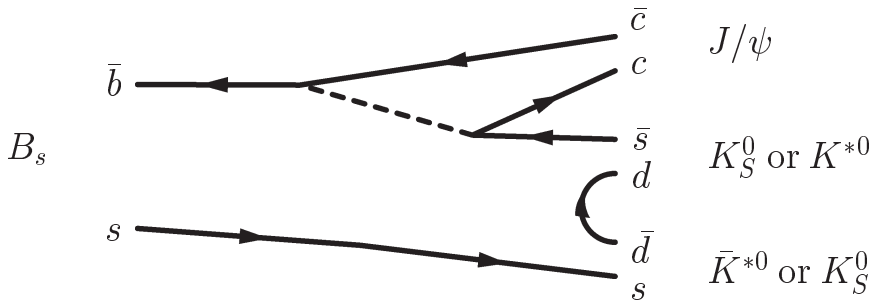

Figure 6.1: The Feynman diagram for $B_s \to J/\psi K^0_S K^0_S$, $J/\psi K^0_S \bar{K}^{*0}$, $J/\psi K^{*0} K^0_S$, and $J/\psi K^{*0} \bar{K}^{*0}$.

The first two modes involve a $d\bar{d}$ quark pair as shown in figure 6.1. They differ only by which kaon hadronizes[1] into a vector (K^{*0}) *vs.* a scalar (K^0_S) state.[2] The last two decay modes listed arise from a Feynman diagram similar to figure 6.1 but with a $u\bar{u}$ pair instead. These two modes also differ only by which kaon hadronizes into a vector *vs.* a scalar state.

These final states could also arise via a $K^{*0}K^0_S$ resonance such as $B_s \to J/\psi\phi(1680)$ with $\phi(1680) \to K^{*0}K^0_S$. Possibilities for such resonances are listed in table 6.1.

Resonance	BR to $K^*K + KK^*$
$a_1(1260)$	seen
$f_1(1420)$	dominant
$\eta(1440)$	seen
$\pi_2(1670)$	$(4.2 \pm 1.4)\%$
$\phi(1680)$	dominant
$\phi_3(1850)$	seen

Table 6.1: $K^{*0}K^0_S$ resonances

In general B_s decays are more difficult to observe than those of B^0 or $B^\pm$ mesons because the fraction f_s of b-quarks which hadronize into a B_s is smaller than the fractions f_d or f_u which hadronize into a B^0 or a $B^\pm$. At the Tevatron center of mass energy of 1.8 TeV, the ratio is $f_s/f_d = 2f_s/(f_u + f_d) = 2 \cdot (0.213 \pm 0.068)$ [31]. Given the small B^0 signals of chapter 5, this additional suppression could make it impossible

[1]The kaon formed with the spectator s-quark will be referred to as the "spectator kaon"; the other kaon will be referred to as the "W kaon". When a decay is written (*e.g.*, $B_s \to J/\psi K^{*0} K^0_S$) the first kaon will correspond to the W kaon and the second one will correspond to the spectator kaon.

[2]In principle the states $B_s \to J/\psi K^0_S K^0_S$ and $B_s \to J/\psi K^{*0} \bar{K}^{*0}$ are also possible, but these contribute to different final states and are not considered in this study.

to observe the equivalent B_s modes. On the other hand, the final state $J/\psi K^0_S \pi K$ potentially has four quark popping modes which contribute to it in comparison to two quark popping modes for $J/\psi K^0_S \pi^+ \pi^-$. These additional contributions might balance the f_s/f_d suppression to allow a $B_s \to J/\psi K^0_S \pi K$ observation.

6.1.2 Physics Possibilities

This section describes the possibilities for measuring B_s mixing and non-Standard Model CP violation with the $B_s \to J/\psi K^{(*)0} \bar{K}^{(*)0}$ modes, but the arguments and formulas apply to the charged kaon modes as well[3]. For CP violation, the crucial feature of these decay modes is that both B_s and $\bar{B}_s$ can decay to both $J/\psi K^0_S \bar{K}^{*0}$ and $J/\psi K^{*0} K^0_S$. This allows the possibility of CP violation due to interference between mixed and unmixed decays, similar to the situation of $B_s \to D_s^{\mp} K^{\pm}$ [39].

Since the final states are not CP eigenstates, the time dependent decay rates for these modes are rather complicated:

$$\begin{aligned}
\Gamma_f(t) = \Gamma_{B_s \to J/\psi K^0_S \bar{K}^{*0}} &= Ae^{-t}\Bigg[\sqrt{1-R^2}\,\cos(\theta+\delta)\sinh\left(\frac{\Delta\Gamma}{\Gamma}\cdot\frac{t}{2}\right)+\cosh\left(\frac{\Delta\Gamma}{\Gamma}\cdot\frac{t}{2}\right) \\
&\quad + R\cos(x_s t) \;-\; \sqrt{1-R^2}\,\sin(\theta+\delta)\sin(x_s t)\Bigg] \qquad (6.1)\\
\Gamma_{\bar{f}}(t) = \Gamma_{B_s \to J/\psi K^{*0} K^0_S} &= Ae^{-t}\Bigg[\sqrt{1-R^2}\,\cos(\theta-\delta)\sinh\left(\frac{\Delta\Gamma}{\Gamma}\cdot\frac{t}{2}\right)+\cosh\left(\frac{\Delta\Gamma}{\Gamma}\cdot\frac{t}{2}\right) \\
&\quad - R\cos(x_s t) \;-\; \sqrt{1-R^2}\,\sin(\theta-\delta)\sin(x_s t)\Bigg] \qquad (6.2)\\
\bar{\Gamma}_f(t) = \Gamma_{\bar{B}_s \to J/\psi K^0_S \bar{K}^{*0}} &= Ae^{-t}\Bigg[\sqrt{1-R^2}\,\cos(\theta+\delta)\sinh\left(\frac{\Delta\Gamma}{\Gamma}\cdot\frac{t}{2}\right)+\cosh\left(\frac{\Delta\Gamma}{\Gamma}\cdot\frac{t}{2}\right) \\
&\quad - R\cos(x_s t) \;+\; \sqrt{1-R^2}\,\sin(\theta+\delta)\sin(x_s t)\Bigg] \qquad (6.3)\\
\bar{\Gamma}_{\bar{f}}(t) = \Gamma_{\bar{B}_s \to J/\psi K^{*0} K^0_S} &= Ae^{-t}\Bigg[\sqrt{1-R^2}\,\cos(\theta-\delta)\sinh\left(\frac{\Delta\Gamma}{\Gamma}\cdot\frac{t}{2}\right)+\cosh\left(\frac{\Delta\Gamma}{\Gamma}\cdot\frac{t}{2}\right) \\
&\quad + R\cos(x_s t) \;+\; \sqrt{1-R^2}\,\sin(\theta-\delta)\sin(x_s t)\Bigg] \qquad (6.4)
\end{aligned}$$

where

- t is the time of decay, parameterized in units of the average B_s lifetime.

[3] Interference terms between the charged and neutral modes are ignored here since they contribute only in the small overlap region of the charged and neutral K^* contributions to the $K^0_S \pi K$ Dalitz plot

- $\Delta\Gamma/\Gamma$ is the fractional partial width difference of the CP-even *vs.* -odd components of the B_s. The CP-even and -odd B_s eigenstates are expected to have lifetimes which differ by $\sim 10\%$ [40].
- $x_s \equiv \Delta m_s/\Gamma$ is the $B_s \leftrightarrow \bar{B}_s$ mixing parameter.
- $R = (1-\rho^2)/(1+\rho^2)$ and $\rho = |A_f|/|\bar{A}_f|$ is the ratio of the amplitudes of the decays where the W *vs.* the spectator kaon is the K^*.
- A is a normalization factor
- δ is a strong phase difference between the decays arising from QCD interactions in the hadronization process. In other decay modes, δ is often predicted to be small. *E.g.*, the strong phase difference between $B_s \to D_s^- K^+$ and $B_s \to D_s^+ K^-$ is predicted to be less than 5% [41] even though the hadronization process is different in the two decays. In one case the spectator s quark combines with a $b \to c$ quark to form a D_s while in the other decay it combines with a $b \to u$ quark to form a K. It is likely that the strong phase difference of these quark popping decays is also small but the situation has not been specifically studied.
- θ is the weak phase in the B_s mixing and decay. As mentioned in section 2.7, the B_s mixing contributes only real terms, and the decay terms of $B_s \to J/\psi K_S^0 \pi K$ are V_{cb} and V_{cs}, both of which are also approximately real. Thus any large value for θ would be evidence of a non-Standard Model contribution.

To understand the structure of equations 6.1 to 6.4, we consider several limiting cases and the physics that could be extracted from these equations in those situations. Plots of $\Gamma_f(t)$ for the various cases discussed are shown in figure 6.2.

If $\Delta\Gamma/\Gamma$ is small, the sinh terms disappear and the cosh terms become approximately 1, reducing the equations to:

$$\Gamma_f(t) = Ae^{-t}\left[1 + R\cos(x_s t) + \sqrt{1-R^2}\sin(x_s t)\sin(\delta+\theta)\right] \quad (6.5)$$

$$\Gamma_{\bar{f}}(t) = Ae^{-t}\left[1 - R\cos(x_s t) - \sqrt{1-R^2}\sin(x_s t)\sin(\delta-\theta)\right] \quad (6.6)$$

$$\bar{\Gamma}_f(t) = Ae^{-t}\left[1 - R\cos(x_s t) - \sqrt{1-R^2}\sin(x_s t)\sin(\delta+\theta)\right] \quad (6.7)$$

$$\bar{\Gamma}_{\bar{f}}(t) = Ae^{-t}\left[1 + R\cos(x_s t) + \sqrt{1-R^2}\sin(x_s t)\sin(\delta-\theta)\right] \quad (6.8)$$

If the ratio of amplitudes ρ is close to 1 (*i.e.*, the W and the spectator kaons are equally likely to hadronize into a K^{*0} or a K_S^0), then R approaches 0 and the equations reduce to:

$$\Gamma_f(t) = Ae^{-t}\left[1 + \sin(x_s t)\sin(\delta+\theta)\right] \quad (6.9)$$

$$\Gamma_{\bar{f}}(t) = Ae^{-t}\left[1 - \sin(x_s t)\sin(\delta-\theta)\right] \quad (6.10)$$

$$\bar{\Gamma}_f(t) = Ae^{-t}\left[1 - \sin(x_s t)\sin(\delta+\theta)\right] \quad (6.11)$$

$$\bar{\Gamma}_{\bar{f}}(t) = Ae^{-t}\left[1 + \sin(x_s t)\sin(\delta-\theta)\right] \quad (6.12)$$

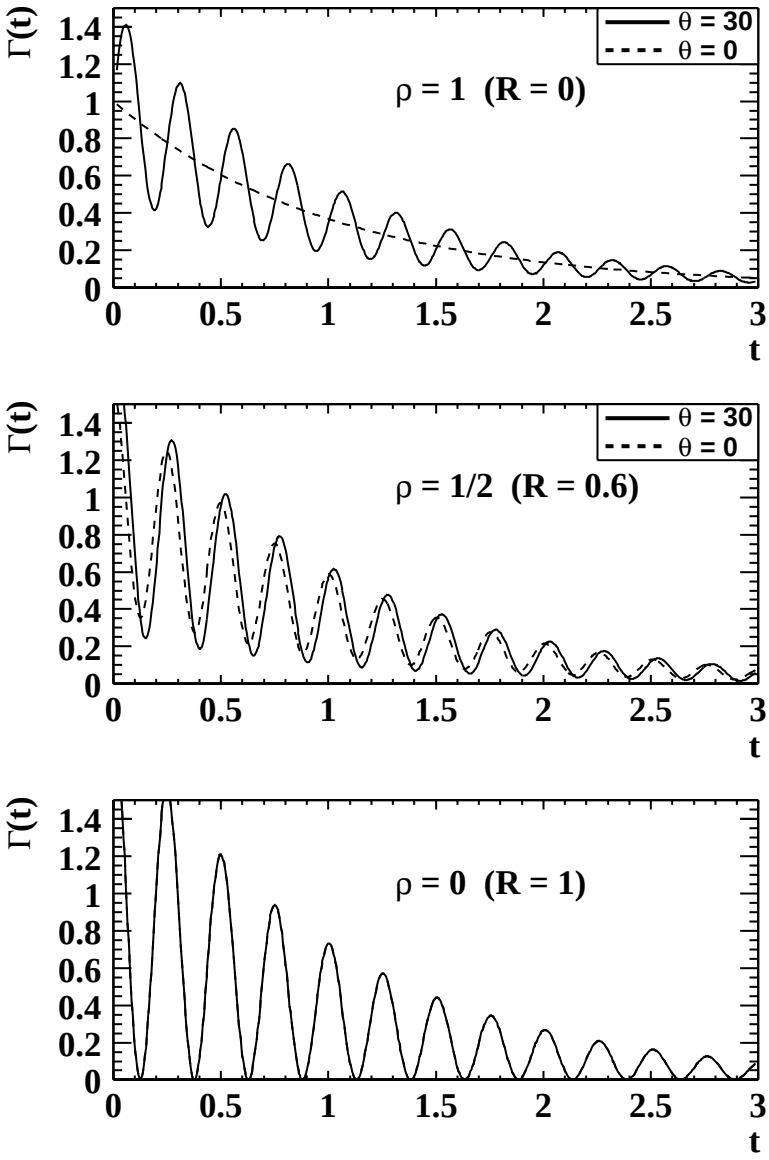

Figure 6.2: Time dependent decay rate $\Gamma_f(t)$ for $B_s \to J/\psi K^0_S \pi^- K^+$ showing a Standard Model phase of $\theta = 0°$ (dashed line) and a non-Standard Model phase of $\theta = 30°$ (solid line). The top plot is for $\rho = 1$, *i.e.*, both spectator and W-kaons are equally likely to hadronize into a K^0_S or a K^{*0}. The middle plot is when $\rho = 1/2$. When $\rho = 0$ (bottom plot) or infinity, $\Gamma_f(t)$ loses all dependence upon the weak phase but become maximally sensitive to B_s mixing due to the large oscillation amplitude. These plots use $x_s = 25$, $\Delta\Gamma/\Gamma = 0$, and $\delta = 0$.

This situation provides the best sensitivity for measuring the CP violating phase θ which should be small in the Standard Model. Figure 6.2 (top) shows the difference in $\Gamma_f(t)$ for the Standard Model (dashed line) and a non-Standard Model phase of $\theta = 30^\circ$ (solid line).

If $\rho = 1/2$, the $\theta = 0^\circ$ and $\theta = 30^\circ$ predictions become quite similar as shown in figure 6.2 (middle). If one of the amplitudes dominates, then ρ approaches 0 (or infinity), R approaches 1 (or -1), and the equations reduce to:

$$\Gamma_f(t) = Ae^{-t}\left[1 \pm \cos(x_s t)\right] \quad (6.13)$$
$$\Gamma_{\bar{f}}(t) = Ae^{-t}\left[1 \mp \cos(x_s t)\right] \quad (6.14)$$
$$\bar{\Gamma}_f(t) = Ae^{-t}\left[1 \mp \cos(x_s t)\right] \quad (6.15)$$
$$\bar{\Gamma}_{\bar{f}}(t) = Ae^{-t}\left[1 \pm \cos(x_s t)\right] \quad (6.16)$$

where the upper sign in $\pm$ and $\mp$ correspond to when $R = 1$. This situation is shown in figure 6.2 (bottom). The dependence upon θ is completely gone, but the amplitude of the oscillations is maximal which allows the best sensitivity for measuring B_s mixing.

The CP violating phase θ is the same as the phase measured with $B_s \to J/\psi\phi$. The decays $J/\psi \to \mu^+\mu^-$ and $\phi \to K^+K^-$ form a clean signature and the branching ratio for $B_s \to J/\psi\phi$ is expected to be the largest of the possible $B_s \to J/\psi X$ decay modes. Thus $B_s \to J/\psi\phi$ will likely provide a much more sensitive measurement of θ; these quark popping modes could serve as a cross check, especially if a non-Standard Model phase is observed.

CDF and BTeV intend to measure B_s mixing with $B_s \to D_s^{\pm}\pi^{\mp}$ but that mode depends crucially upon a displaced track trigger (see chapter 8) which has never before been tried. If there is initial difficulty with that trigger, these modes may serve as a backup option since they use the well established $J/\psi \to \mu^+\mu^-$ trigger. Chapter 7 discusses $B_s \to J/\psi\bar{K}^{*0}$ which is another $B_s \to J/\psi X$ mode which has potential for measuring B_s mixing. All of these modes appear to have small branching ratios which limit their usefulness; the specific branching ratios and the value of ρ will determine whether these quark popping modes or $B_s \to J/\psi\bar{K}^{*0}$ are more useful for a B_s mixing measurement.

If $\Delta\Gamma/\Gamma$ is large such that the sinh terms are not nearly 0, these equations may be added together and the rapidly oscillating $\sin(x_s t)$ and $\cos(x_s t)$ terms cancel. Thus $\cos(\theta \pm \delta)$ could be determined without needing to tag the flavor of the decaying B_s or resolve the rapid time oscillations of the $\cos(x_s t)$ and $\sin(x_s t)$ terms. Since the effective flavor tagging efficiency at CDF is only $\sim 10\%$ this method greatly increases the number of events available for the measurement. For the current predictions of $\Delta\Gamma/\Gamma \approx 10\%$ [40], this gain in number of events is not sufficient to resolve the small contribution of the sinh terms.

6.1.3 Choice of Reference Mode

For these modes it is not clear which reference mode should be used. On one hand, all contributions involve a K^0_S so $B^0 \to J/\psi K^0_S$ is an obvious choice. But in two of the submodes the K^0_S come directly from the B decay while in the other two it comes via a $K^{*\pm}$ which could result in different p_T spectra. Additionally, in the case of $B^0 \to J/\psi K^0_S \pi^+\pi^-$, the optimized $p_T(K^0_S)$ cut was quite low (1.0 GeV/c) as compared to the $p_T(K^{*0}) > 2.4$ GeV/c optimized cut for $B^0 \to J/\psi K^{*0}\pi^+\pi^-$. Thus $p_T(K^{*0})$ might be a more powerful cut than $p_T(K^0_S)$.

The other reference mode option is $B^0 \to J/\psi K^{*0}$. Two of the modes have a charged K^* rather than a neutral one, but the underlying p_T spectra should be the same for both. However, the observed $p_T(K^{*\pm})$ spectrum will be somewhat harder since $K^{*\pm}$ has three final state daughters (the pion plus the two K^0_S pions) which must be above the minimum p_T threshold rather than just two for K^{*0}. Additionally, it is not necessarily known which particle assignments should form a K^*. With a sufficient number of signal events (*i.e.*, hundreds), the $K^0_S\pi K$ Dalitz plot could statistically separate the relative contributions but any given candidate could have multiple plausible K^* combinations.

For this analysis we try both options for reference modes. In the case of $B^0 \to J/\psi K^{*0}$, we use the K^* candidate (charged or neutral) with the highest p_T for the $p_T(K^*)$ cut. *I.e.*, a cut of $p_T(K^*) > 2.0$ GeV/c would require that the K^* candidate with the highest p_T has $p_T > 2.0$ GeV/c.

6.2 Results

6.2.1 $B^0 \to J/\psi K^0_S$ Reference

Optimizing the $p_T(K^0_S)$, $ct(B)$, and Iso(B) cuts using $B^0 \to J/\psi K^0_S$ as the reference mode results in the cuts listed in table 6.2 and the mass distribution of figure 6.3. In the highlighted signal region (5.37 ± 0.02 GeV/c^2) there are 27 events on a sideband fitted background of 16.9. This leads to a Feldman Cousins[4] 95% confidence interval of [2.2, 21.9] signal events. Although this confidence interval technically excludes 0, the data plot does not appear to indicate a genuine signal. The 99% confidence interval is [0, 26.0].

With the cuts listed in table 6.2, the reference mode $B^0 \to J/\psi K^0_S$ has 60.3 ± 8.3 events and the ratio of efficiencies $\epsilon_{ref}/\epsilon_{sig}$ is 2.06. In order to extract a branching ratio, equation 4.2 must be slightly modified to account for the relative fraction of B_s

[4]The Feldman Cousins method [37] of setting confidence limits is a classical (*i.e.*, non-Bayesian) approach to setting confidence intervals which has the primary benefit of providing a smooth transition from the case of an upper limit to that of a confidence interval which excludes 0.

Cut	Minimum	Maximum	Step Size	Optimized Value SVX	Optimized Value non-SVX
$p_T(K_S^0)$	0.6 GeV/c	2.0 GeV/c	0.1 GeV/c	1.0 GeV/c	1.0 GeV/c
$ct(B)$	0 μm	200 μm	10 μm	30 μm	—
Iso(B)	0.40	0.80	0.05	0.75	0.80

Table 6.2: Optimized cuts for $B_s \to J/\psi K_S^0 \pi K$ using $B^0 \to J/\psi K_S^0$ as the reference mode.

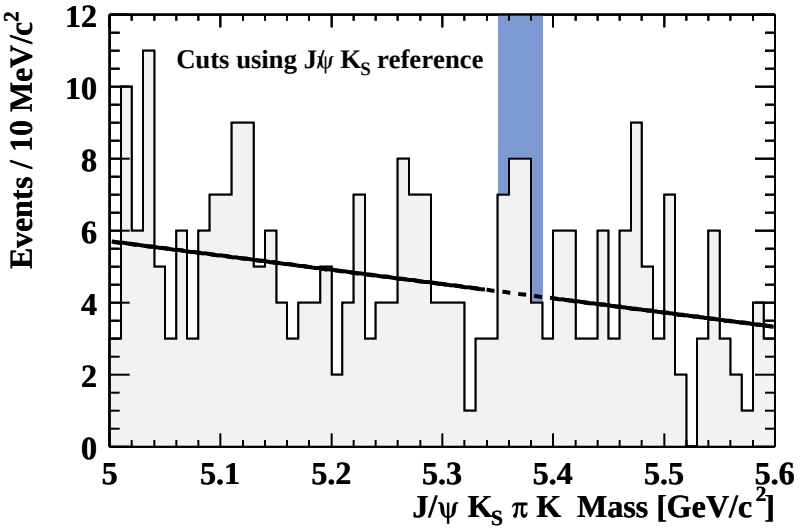

Figure 6.3: $J/\psi K_S^0 \pi K$ mass distribution with cuts from $J/\psi K_S^0$ reference. The dark band highlights the B_s mass region.

mesons produced (f_s) in comparison to the fraction of B^0 mesons produced (f_d):

$$\mathrm{BR}_{sig} = \frac{N_{sig}}{N_{ref}} \cdot \frac{\epsilon_{ref}}{\epsilon_{sig}} \cdot \frac{f_d}{f_s} \cdot \mathrm{BR}_{ref} \tag{6.17}$$

Using $\mathrm{BR}_{ref} = \mathrm{BR}(B^0 \to J/\psi K^0) = (8.9 \pm 1.2) \times 10^{-4}$ [11], this leads to a signal branching ratio between

$$1.6 \times 10^{-4} < \mathrm{BR}(B^0 \to J/\psi K^0 \pi^{\pm} K^{\mp}) < 16 \times 10^{-4}. \tag{6.18}$$

We re-emphasize, however, that the mass distribution of figure 6.3 does not appear to contain a genuine signal.

Cut	Minimum	Maximum	Step Size	Optimized
$p_T(K^{*0})$	1.6 GeV/c	3.0 GeV/c	0.1 GeV/c	1.8 GeV/c
$ct(B)$	100 μm	300 μm	10 μm	100 μm
Iso(B)	0.40	0.80	0.05	0.55

Table 6.3: Optimized cuts for $B_s \to J/\psi K^0_S \pi K$ using $B^0 \to J/\psi K^{*0}$ as the reference mode.

6.2.2 $B^0 \to J/\psi K^{*0}$ Reference

Optimizing the cuts using $B^0 \to J/\psi K^{*0}$ as the reference mode results in the cuts of table 6.3. The mass distribution with these cuts is shown in figure 6.4. Although a small peak appears, the mass is too low and the number of events are not sufficient to establish a signal at a 95% confidence level. Within the $\pm 2\sigma$ window about the B_s mass there are 15 events on a fitted background of 9.8 for a Feldman Cousins 95% confidence interval of [0, 14.5] signal events.

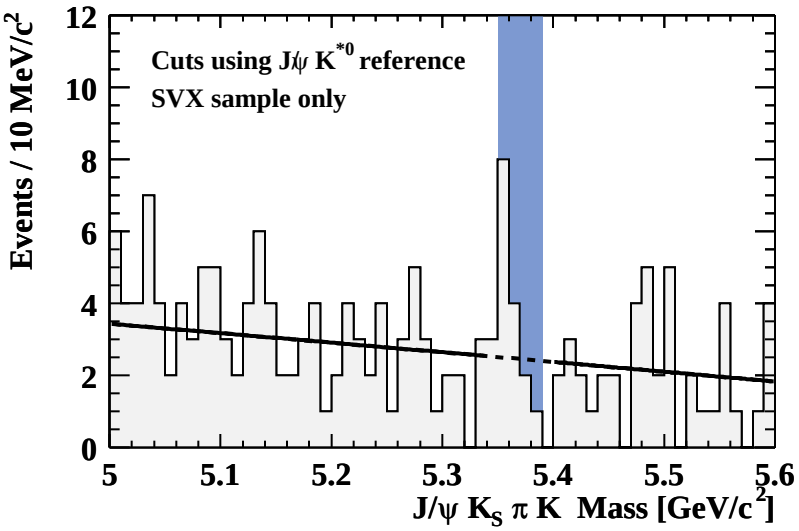

Figure 6.4: $J/\psi K^0_S \pi K$ mass distribution with cuts from $J/\psi K^{*0}$ reference. The dark band highlights the B_s signal region. Although there is a small excess of events within the signal region, it is not large enough to establish a signal at a 95% confidence level.

With these cuts the reference mode $B^0 \to J/\psi K^{*0}$ has 332 ± 21 events and a ratio of efficiencies $\epsilon_{ref}/\epsilon_{sig} = 2.55$. Using $\mathrm{BR}(B^0 \to J/\psi K^{*0}) = (1.50 \pm 0.17) \times 10^{-3}$ [11], we obtain the branching ratio limit of

$$\mathrm{BR}(B_s \to J/\psi K^0_S \pi^{\pm} K^{\mp}) < 3.9 \times 10^{-4} \ \ (\mathrm{FC}\ 95\%,\ J/\psi K^{*0}\ \mathrm{reference}) \qquad (6.19)$$

In comparison to the other quark popping modes studied here, this limit is rather low. Conclusions will be discussed in section 6.4.

6.3 Uncertainties

The systematic uncertainties for these modes are mostly the same as for the decay modes discussed in chapter 5 with the addition of a large uncertainty on the B_s *vs.* B^0 production fractions f_s/f_d. The systematic uncertainties are listed in table 6.4.

Systematic Uncertainty	%
f_s/f_d	32
BR($B^0 \to J/\psi K^{*0}$)	11
Helicity Model	10
Trigger Model	5
Sample Composition	5
B Production Model	2.5
Combined Systematics	**36**

Table 6.4: $B^0 \to J/\psi K^0_S \pi K$ Systematic Uncertainties

From the data the quantity which we fundamentally limit is the number of observed signal events. These systematic uncertainties are on the conversion factor between that number of events and an actual branching ratio and are not included in the Feldman Cousins branching ratio limit quoted in equation 6.19. For extrapolating these results into CDF Run II and estimating this mode's usefulness for making a physics measurement, the number of events is the more important quantity. The actual branching ratio is not particularly interesting except in comparison to the other quark popping modes.

6.4 $B^0_s \to J/\psi K^0 \pi^{\mp} K^{\pm}$ Conclusions

Given that at least four decay modes could contribute to $B_s \to J/\psi K^0_S \pi K$, the branching ratio limit of equation 6.19 is surprisingly low in comparison to the branching ratios of chapter 5, even when considering their $\mathcal{O}(20\%)$ contributions from $B^0 \to \psi(2S) K^{(*)0}$ for which there is no equivalent contribution to these B_s decays.

It is possible that these B_s decays have branching ratios similar to their B^0 counterparts and that the discrepancy lies in the uncertainty on the conversion factor between the number of observed events and the branching ratio. Currently there is no consensus within the high energy physics community on the best method for

setting confidence limits when there are large uncertainties, as is the case here. For now we quote equation 6.19 as the result with the caveat that it does not include the effects of the conversion factor uncertainty[5].

Since there is a hint of a signal, we extrapolate these results to Run II to ascertain how much data would be necessary to improve these results. For a 3σ effect, the observed signal size needs to be greater than 3 times the expected statistical fluctuation size of the background, *i.e.*, $S \geq 3\sqrt{B}$. Using $S/B = 1/2$, this corresponds to observing at least 18 signal events on an expected background of 36 events. We observe 15 events total in the signal region of figure 6.4, thus to establish a 3σ effect with a $S/B = 1/2$ we would need approximately 4 times the amount of data. As will be described in chapter 8, the increases in Run II luminosity and $J/\psi \to \mu^+\mu^-$ trigger efficiency correspond to almost twice as many $B \to J/\psi X$ events recorded each month as were collected in all of Run I. Thus only a few months of running at Run II design luminosity is required to establish a 3σ signal or improve the limit. A 5σ discovery would require approximately year of data taking.

[5]One example of incorporating systematic uncertainties into a limit is reference [42] which incorporates systematic uncertainties into classical Poisson limits. A small fractional uncertainty ξ increases the limit by a term proportional to ξ^2. But as ξ increases, the method fails and the effect on the limit can be much larger than ξ.

Chapter 7

$B_s^0 \to J/\psi \bar{K}^*(892)^0$

7.1 Overview

Several collaborations have considered using the decay $B_s \to J/\psi \bar{K}^{*0}$ to measure B_s mixing [43, 44]. The $\bar{K}^{*0} \to K^-\pi^+$ decay provides a tag of the flavor of the B_s at decay while $J/\psi \to \mu^+\mu^-$ provides an easy and well established trigger. The four daughter particles coming from the same secondary vertex allow a precise vertex measurement for good proper time resolution on the decay. The only disadvantage is the low expected branching ratio arising from CKM suppression due to a V_{cd} term in the Feynman diagram, shown in figure 7.1 (top).

The expected branching ratio may be estimated by comparing the $B_s \to J/\psi \bar{K}^{*0}$ Feynman diagram to the one for $B^0 \to J/\psi K^{*0}$. They differ only by an *s vs. d* spectator quark and by V_{cd} *vs.* V_{cs} as shown in figure 7.1. Neglecting the different spectator quark, the ratio of branching ratios is simply

$$\frac{\mathrm{BR}(B_s \to J/\psi \bar{K}^{*0})}{\mathrm{BR}(B^0 \to J/\psi K^{*0})} = \left(\frac{|V_{cd}|}{|V_{cs}|}\right)^2 = 0.051 \tag{7.1}$$

Using $\mathrm{BR}(B^0 \to J/\psi K^{*0}) = (1.50 \pm 0.17) \times 10^{-4}$ [11], the predicted $B_s \to J/\psi \bar{K}^{*0}$ branching fraction is:

$$\mathrm{BR}(B_s \to J/\psi \bar{K}^{*0}) = 7.65 \times 10^{-5} \ \text{(SM Prediction)} \tag{7.2}$$

It would be a surprise if the branching ratio were significantly different from this value. None-the-less, the CDF Run I sensitivity is close to this value and it is worthwhile to confirm that the branching ratio is this small and consider the usefulness of this mode for Run II B_s mixing measurements.

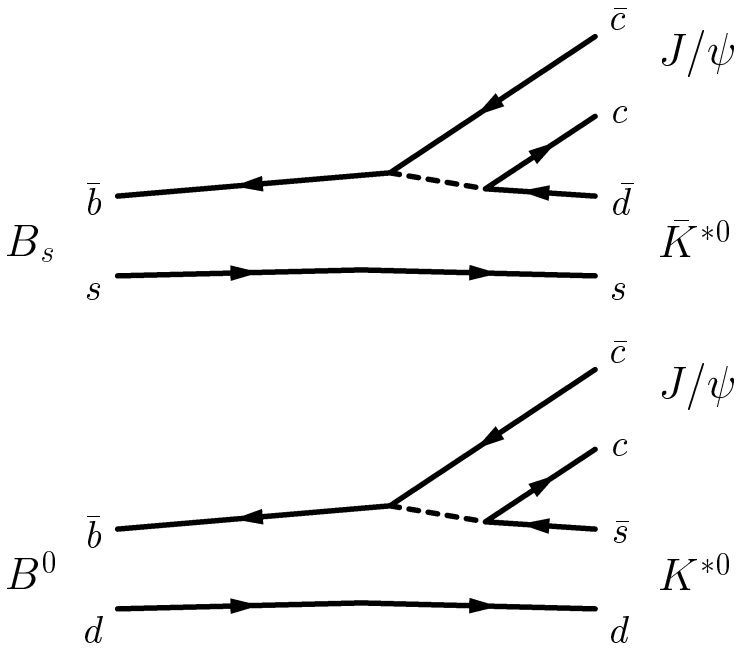

Figure 7.1: Feynman diagrams for $B_s \to J/\psi \bar{K}^{*0}$ (top) and $B^0 \to J/\psi K^{*0}$ (bottom).

7.2 Search Method

The method for optimizing the cuts is somewhat simpler in this case than in the other modes considered in this study since the reference mode $B^0 \to J/\psi K^{*0}$ has the same final state at a slightly lower mass than the B_s signal. Trigger, cut, and acceptance efficiencies completely cancel, making this a very clean measurement of the ratio of branching ratios.

As before, we relate the reference mode to the signal mode with:

$$\mathrm{BR}(B_s \to J/\psi \bar{K}^{*0}) = \mathrm{BR}(B^0 \to J/\psi K^{*0}) \cdot \frac{f_d}{f_s} \cdot \frac{N(B_s \to J/\psi \bar{K}^{*0})}{N(B^0 \to J/\psi K^{*0})} \tag{7.3}$$

Using

$$\frac{f_s}{f_d} = \frac{2f_s}{f_u + f_d} = 2 \cdot (0.213 \pm 0.068) \tag{7.4}$$

and $\mathrm{BR}(B^0 \to J/\psi K^{*0}) = (1.5 \pm 0.17) \times 10^{-3}$ we relate the number of observed events to the branching ratio with

$$\mathrm{BR}(B_s \to J/\psi \bar{K}^{*0}) = (3.52 \pm 1.19) \times 10^{-3} \cdot \frac{N(B_s \to J/\psi \bar{K}^{*0})}{N(B^0 \to J/\psi K^{*0})} \tag{7.5}$$

Since the Standard Model branching ratio prediction is so small, we optimize the cuts for search sensitivity, *i.e.*, we minimize the average limit that would be set

in the absence of a signal given the expected average background. For a given set of cuts this involves only measuring $N(B^0 \to J/\psi K^{*0})$ and calculating the limit on $N(B_s \to J/\psi \bar{K}^{*0})$ from the fitted background. This minimization does not use the number of events in the B_s signal region since using that information in the optimization could lead to a systematic search bias.

We fit the B mass distribution with an unbinned likelihood method using a Gaussian for the B^0 peak plus a quadratic background while excluding $\pm 3\sigma$ around the B_s mass. The mass resolution σ is taken from the fit to the B^0 peak and is 15 MeV/c^2. The signal window in which we eventually look for events is $\pm 2\sigma$ about the B_s mass, which introduces an additional factor of 1/0.9545 to equation 7.3 to account for the finite search window width.

We scanned the cut values for $p_T(K^{*0})$, $ct(B)$, and Iso(B), finding the best search sensitivity using the cuts in table 7.1.

Cut	Min	Max	Step Size	Optimized Value
$p_T(K^{*0})$	1.8 GeV/c	3.0 GeV/c	0.1 GeV/c	2.8 GeV/c
$ct(B)$	100 μm	350 μm	10 μm	150 μm
Iso(B)	0.50	0.70	0.02	0.60

Table 7.1: Optimized cuts for $B_s \to J/\psi \bar{K}^{*0}$

7.3 Results

Figure 7.2 shows the resulting mass peak, drawn with a log scale to make counting of the events in the B_s mass window easier. There are 225 ± 17 B^0 events and 9 events in the B_s signal region with an expected mean background of 10.5 events. Compared to the uncertainties on BR($B^0 \to J/\psi K^{*0}$), f_s/f_d, and $N(B^0)$, the uncertainty on the average background is negligible.

At this point it becomes somewhat of a matter of taste for what kind of limit is specifically quoted. Using the unified approach of Feldman and Cousins[1] for a 9 event observation with an expected background of 10.5, the 95% confidence interval on the signal size is $[0, 6.38]$ which corresponds to a branching ratio limit of

$$\mathrm{BR}(B_s \to J/\psi \bar{K}^{*0}) < 1.0 \times 10^{-4} \quad \text{(Feldman Cousins 95\%)} \tag{7.6}$$

We note, however, that this method does not incorporate the uncertainty on the conversion factor between number of events and the branching ratio. Currently there is

[1]The Feldman Cousins method [37] of setting confidence limits is a classical (*i.e.*, non-Bayesian) approach to setting confidence intervals which has the primary benefit of providing a smooth transition from the case of an upper limit to that of a confidence interval which excludes 0.

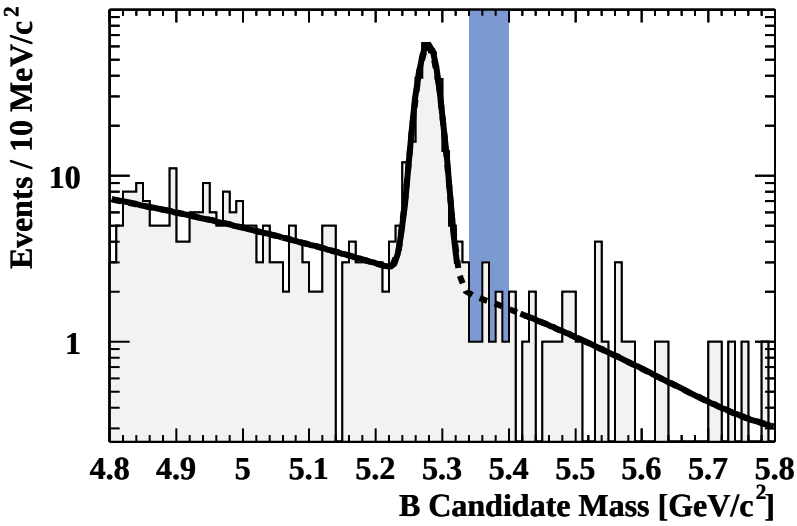

Figure 7.2: $B^0 \to J/\psi K^{*0}$ mass peak. There are 225 ± 17 B^0 events with 9 events in the highlighted B_s mass window with an expected mean background of 10.5 events.

no consensus within the high energy physics community on the best method for setting confidence limits when there are large uncertainties, as is the case here. We thus quote the limit in equation 7.6 with the caveat that there is an $\mathcal{O}(35\%)$ uncertainty in the conversion factor used in deriving it. The information provided here should be sufficient to derive a limit with any alternate method if so desired.

Since we observe a number of events lower than the average background the limit obtained is somewhat better than the search sensitivity. The average signal limit which would be obtained in the absence of a true signal given an expected background of 10.5 events is 8.27 events. This search sensitivity corresponds to a branching ratio limit of 1.3×10^{-4}.

7.3.1 x_s Reach

Whichever limit method is chosen, the important point is that the branching ratio for $B_s \to J/\psi \bar{K}^{*0}$ is small. The number of signal events required to place a 95% confidence limit on x_s may be obtained from equation 20 of [45]:

$$1.645 = \sqrt{\frac{1}{2}}\sqrt{\frac{S^2}{S+B}}\sqrt{\epsilon D^2}\exp[-(x_s\sigma_{t/\tau})^2/2] \tag{7.7}$$

where $\sigma_{t/\tau}$ is the proper time resolution in units of B_s lifetimes and ϵD^2 is the effective flavor tagging efficiency. Solving for the signal size S and using $S/B = 1/2$, $\sigma_{t/\tau} =$

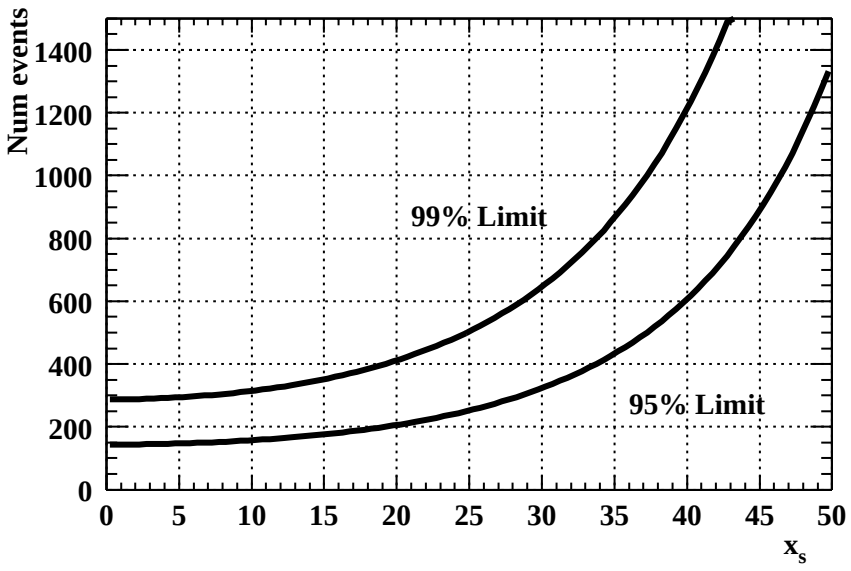

Figure 7.3: Number of events required to place a 95% confidence limit on x_s with $S/B = 1/2$ and a proper time resolution $\sigma_{t/\tau} = 0.03$. The Standard Model branching ratio corresponds to approximately 120 $B_s \to J/\psi K^{*0}$ events per fb^{-1}.

0.03, and $\epsilon D^2 = 0.113$ [46], we obtain:

$$S = 140 \exp[0.0009 x_s^2] \tag{7.8}$$

This function is plotted in figure 7.3.

As described in chapter 8, the $J/\psi \to \mu^+\mu^-$ yield of the first two years of Run II is expected to be 50 times larger than that of Run I. Scaling from the number of B^0 events observed here, the limit in equation 7.6 corresponds to less than 320 $B_s \to J/\psi \bar{K}^{*0}$ events within the first 2 fb^{-1} of Run II for a maximum x_s 95% confidence limit of 30. The Standard Model branching ratio corresponds to only 245 events for an x_s limit reach of 25. Although these limits are near or slightly above the Standard Model prediction of $x_s = 25$, the number of events are not sufficient to make a 5σ discovery. Thus this branching ratio limit confirms that $B_s \to J/\psi \bar{K}^{*0}$ will likely not be very useful in Run II since at least a year's worth of data will be necessary to set any x_s limit with this mode. Provided that the displaced vertex trigger (described in chapter 8) works, x_s should be measured with $B_s \to D_s \pi$ long before it is measured with $B_s \to J/\psi \bar{K}^{*0}$.

Chapter 8

Future Prospects

8.1 CDF II Detector Upgrade

CDF is entering a new Run with a significantly upgraded detector. The Tevatron will be running at much higher luminosity (up to 2×10^{32} cm^{-2}s^{-1}, in comparison to a maximum of 2.8×10^{31} cm^{-2}s^{-1} in Run I) with a much faster bunch crossing rate (either 396 ns or 132 ns between collisions in comparison to 3.5 μs in Run I). During the first two years of Run II, this increased luminosity will provide 20 times the amount of integrated luminosity of Run I. The higher bunch crossing rate necessitated a replacement of much of the CDF detector and readout electronics to be able to process the higher event rates. Many of the upgraded detector components are designed to operate with similar performance (other than speed) to the Run I detector. Detector portions with major improvements in performance are the muon systems which have increased coverage and shielding; the Silicon Vertex Detector which has been considerably expanded; and the trigger and data acquisition system which will allow triggering on the displaced vertices of B decays.

8.1.1 Muon Systems

There are two major improvements to the muon systems in CDF II: more complete coverage and better shielding. Figure 8.1 shows the Run I muon coverage; the light gray portions between $0.6 < |\eta| < 1.0$ were uninstrumented in Run I and have been completed for Run II. A more important upgrade is additional shielding to reduce backgrounds. During Run I a major source of backgrounds in the muon chambers came from beam–beampipe interactions. These backgrounds necessitated high trigger $p_T(\mu)$ thresholds and pre-scaling to control the rates and were a major limitation of the Run I dimuon trigger. Additional shielding has been added to absorb these backgrounds so that lower p_T thresholds may be used without pre-scaling to greatly improve the trigger efficiency. These improvements are expected to improve the $J/\psi \to \mu^+\mu^-$ trigger efficiency by a factor of 2.5 [46]. *I.e.*, for the same amount

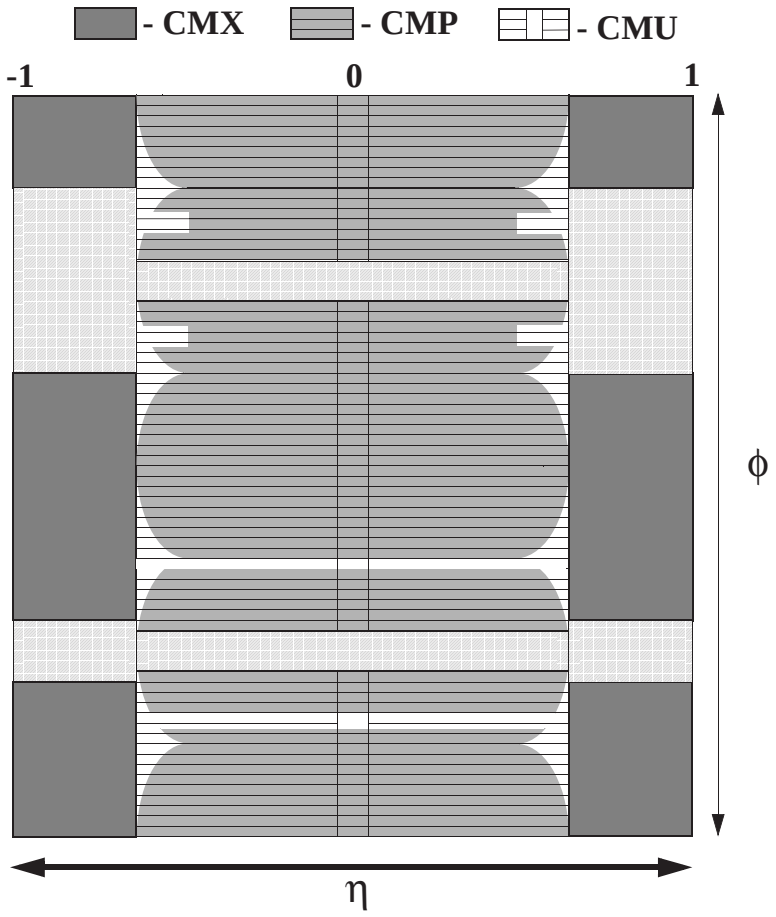

Figure 8.1: CDF Run I muon system coverage. The light gray portions at large η were uninstrumented in Run I but have been completed for Run II.

of luminosity, CDF should record 2.5 times as many $B \to J/\psi X$ decays.

8.1.2 Silicon Vertex Detector

A major limitation of the Run I SVX was that its 51 cm length only covered 60% of the $p\bar{p}$ interaction region. The upgraded SVX II is 87 cm long to provide more complete coverage. It has five layers of double sided silicon strips: one side of each layer has readout strips running parallel to z in order to measure an $r\phi$ position as in Run I; the other side has strips at an angle in order to provide a z position measurement. This provides the SVX II with full 3D tracking ability.

The new SVX II is augmented by an additional single sided silicon strip layer mounted directly on the beam-pipe at a radius of 1.6 cm to provide even more precise impact parameter resolution. Additional silicon detector layers are located at larger radii and higher η regions to extend the tracking ability to $|\eta| < 2.0$.

During Run I, the event readout time of 4 μs was dominated by the SVX but this was not a major problem because the $p\bar{p}$ collisions were separated by a similar time of 3.5 μs. In Run II, however, the SVX II readout time of 6 μs is much longer than the collision spacing of 132 ns. In order to avoid deadtime while digitizing and reading out events, all events are recorded and stored in a capacitor pipeline on the detector, but only those which pass a level 1 trigger[1] are digitized and read out. The digitization and data readout can occur in parallel with the recording of new events. Deadtime is incurred only if there is a fluctuation in the level 1 accept rate such that more than 4 events are accepted in a 21 μs timeperiod.

8.1.3 Trigger

The trigger system has also been upgraded to include a Silicon Vertex Trigger (SVT) which will use SVX II information at the second trigger level to identify long lived particles (*e.g.*, B mesons) by their decay vertices which are displaced from the interaction point. Previously, all-hadronic B decay modes such as $B \to D\pi$ were unavailable to CDF because there was no viable trigger which could distinguish signal from background at a sufficient rate. This trigger will allow all hadronic decay modes of the B to be studied with the large sample of B mesons available at a hadronic accelerator.

8.2 $B \to J/\psi X$ Decays

The increased luminosity of Run II will produce 20 times the integrated luminosity of Run I in just 2 years of operation. In conjunction with the expected 2.5 times

[1]The Level 1 trigger is based upon information from the muon and tracking chambers and the calorimeters, all of which can be read out much faster than the SVX II which has 405,504 channels of data.

increase in the $J/\psi \to \mu^+\mu^-$ trigger efficiency, this corresponds to 50 times are many $B \to J/\psi X$ decays recorded within 2 years. In a single month of running at design luminosity approximately twice as many $B \to J/\psi X$ decays will be recorded in Run II as were recorded in all of Run I.

The decay modes reported in this thesis with $\mathcal{O}(10)$ events in Run I should have many hundreds of events in Run II. This greatly increased data sample will allow much more accurate measurements of their branching ratios and better determination of their constituent sub-modes as well as providing a sufficient number of signal events to begin using these modes for $V_{\rm CKM}$ related physics measurements.

Chapter 9

Conclusions

We have reported evidence for several previously unobserved $B \to J/\psi X$ decay modes. The results of this thesis are summarized as:

- $\mathrm{BR}(B^0 \to J/\psi K^{*0}\pi^+\pi^-) = (8.0 \pm 2.2 \pm 1.5) \times 10^{-4}$
  - Contribution seen from $B^0 \to \psi(2S)K^{*0}$
  - No other substructure seen
- $\mathrm{BR}(B^0 \to J/\psi K^0\pi^+\pi^-) = (1.1 \pm 0.4 \pm 0.2) \times 10^{-3}$
  - $\mathrm{BR}(B^0 \to J/\psi K^0\rho^0) = (5.8 \pm 3.1 \pm 1.2) \times 10^{-4}$
  - $\mathrm{BR}(B^0 \to J/\psi K^{*+}\pi^-) = (8.3 \pm 4.4 \pm 1.7) \times 10^{-4}$

  Contributions also seen from $B^0 \to J/\psi K_1(1270)$ and $B^0 \to \psi(2S)K^0$.
- $\mathrm{BR}(B_s \to J/\psi K^0\pi^\pm K^\mp) < 3.9 \times 10^{-4}$ (Feldman Cousins 95% CL)
- $\mathrm{BR}(B_s \to J/\psi \bar{K}^{*0}) < 1.0 \times 10^{-4}$ (Feldman Cousins 95% CL)

The most statistically significant mode, $B^0 \to J/\psi K^{*0}\pi^+\pi^-$, is a 3.7σ effect. It has a $\sim$ 20% contribution from $B^0 \to \psi(2S)K^{*0}$ which has been observed by CLEO. The remaining 80% of the events are consistent with non-resonant $B^0 \to J/\psi K^{*0}\pi^+\pi^-$ decays.

$B^0 \to J/\psi K^0_S\pi^+\pi^-$ is a 3.3σ effect, however its unexpected narrowness warrants caution in interpreting the results. There is an approximately 20% contribution from $\psi(2S)K^0_S$ (also observed by CLEO) and the $\pi^+\pi^-$ and $K^0_S\pi^\pm$ mass distributions of figures 5.20 and 5.21 indicate contributions from $B^0 \to J/\psi K^0_S\rho^0$ and $B^0 \to J/\psi K^{*+}\pi^-$. With the current data we cannot distinguish whether these are genuine quark popping decays of table 2.1 or whether they proceed via a combination of the resonances listed in table 5.6, *e.g.* $B^0 \to J/\psi K_1(1270)$ with $K_1(1270) \to K^0_S\rho^0$. We note, however, that these modes may be used for CP violation measurements whether they are genuine quark popping decay modes or not.

If the $B^0 \to J/\psi K^0_S \rho^0$ and $B^0 \to J/\psi K^{*+}\pi^-$ decays reported here are quark popping decays and the remaining decay modes listed in table 2.1 have similar branching ratios, this class of decays could explain most of the "missing" $B \to J/\psi X$ decays.

The B^0 decay modes reported here have large enough branching ratios that they should be visible in the current CLEO, Belle, and BaBar datasets. The low backgrounds of $e^+e^- \to \Upsilon(4S) \to B^0\bar{B}^0$ should make these decay modes clearly evident. CDF should record many hundreds of these decays in Run II. That sample should be sufficient to begin making physics measurements using these decay modes.

With the CDF Run I dataset we are only able to establish branching ratio limits for the B_s decay modes studied here. The limits established here are close to the expected branching ratios and these B_s decay modes should be observed in Run II.

• • •

CP violation with B mesons is one of the few remaining areas of the Standard Model which has not yet been precision tested. It is also an area in which non-Standard Model theories make different predictions. The strength of CP violation measurements with B mesons does not lie in a single measurement, but rather in the multitude of possible measurements, all of which must be consistent with a single phase in the $V_{\rm CKM}$ matrix for the Standard Model to be correct. This thesis has added several new decay modes to the list of B decays which may be used to test the consistency of the Standard Model's explanation of CP violation.

Appendix A

CDF Specific Details

This appendix describes CDF specific details of this analysis as a reference for those who wish to perform a similar analysis in Run II. No attempt has been made to limit CDF jargon. In most cases, the relevant details are well documented elsewhere and this appendix simply references the appropriate internal CDF notes.

A.1 Dimuon Trigger

This analysis uses the Stream A Run Ia and Run Ib dimuon datasets located in cdfsga:/data09/bottom/psix_5p (Ia) and cdfsga:/data17/bottom/psia_7b (Ib). The basic trigger requirements are described in section 4.2.1. These triggers require two muon stubs in either the CMU or CMX, but CMP-only muons are not used. Further details about the dimuon triggers may be found in CDF notes 1999 (Ia) and 4076 (Ib).

In the $B^0 \to J/\psi K^0_S$ subsample, the composition of these triggers is approximately as follows:

- 67%: Both trigger muons come from the $J/\psi \to \mu^+\mu^-$ candidate.
- 23%: One of the trigger muons comes from the J/ψ, the other trigger muon is from another decay (*e.g.*, a semileptonic B or D decay).
- 10%: The event did not pass a level 1 or level 2 dimuon trigger but it was included in the Stream A dataset because it passed a single muon trigger at levels 1 and 2 and passed the level 3 dimuon trigger.

Further details of the dataset composition may be found in CDF note 4745.

The Run II dimuon trigger has been changed to lower the $p_T(\mu)$ thresholds and increase the track finding efficiency for low p_T particles. These changes are documented in CDF notes 4718 and 5093. For an analysis such as this it will be important to understand the new dimuon trigger efficiency and have a Run II equivalent of the

DIMUTG module which applies the measured efficiency curves to Monte Carlo data. The Run I dimuon trigger efficiency is documented in CDF note 4076; DIMUTG is documented in CDF note 3537.

A.2 Muon Selections

This analysis only used muons with stubs in both the CMU and CMP. The χ^2 matching cuts were applied to the match between the CMU stub and the CTC track. The χ^2_ϕ referred to in section 4.2.2 is often referred to as χ^2_x in CDF internal documentation since the ϕ direction is referred to as the x direction in the muon internal coordinate system. Analyses which use CMX muons usually use $\chi^2_x < 9$ with no χ^2_z cut for the CTC track to CMX muon stub matching requirement. *E.g.*, see CDF notes 3068, 4267, and 4747.

A.3 L_{xy} Significance Cut

The significance of the K^0_S transverse displacement, $L_{xy}/\sigma_{L_{xy}}$, was determined using the DECLEN subroutine found in cdfsga:/cdf/offln/offline/top/version_7_12/declen.cdf. This subroutine incorporates the uncertainties on the location of the B and K^0_S decay vertices into the L_{xy} calculation.

A.4 Reconstruction Code

This analysis used Petar Maksimović's generic B decay reconstruction code. During Run I this code was not part of the official offline code but it was used by several analyses[1] because of its ease of use for searching for multiple decay topologies. Petar's code has been incorporated into the Run II environment as part of the Sin2BetaMods package. The initial version is documented in CDF note 5217.

A.5 Suggested Changes

Following is a list of suggested changes to consider for future analyses using the much larger Run II dataset.

- The exclusion of CMX muons was simply an oversight, discovered too late to incorporate into the analysis in a timely fashion. Future analyses should use

[1] *E.g.*, in addition to Petar's same side B flavor tagging thesis (CDF note 4614) and this analysis, his reconstruction code was used for Dejan Vucinic's thesis (B^* mesons, CDF note 4718) and Hongquan Niu's thesis (B_s mixing, CDF note 5280).

CMX muons. The loss is not as large as it might appear, however. Since the CMX covers $0.6 < |\eta| < 1.0$, decays which have muons in the CMX are more likely to lose other decay products with $|\eta| > 1.0$ and not be reconstructable anyway. Thus the effective loss in data is $\sim 20\%$.

- More sophisticated fits could improve the statistical significance of these measurements. *E.g.*, the B mass fit could be done with an unbinned likelihood fit that considers the mass resolution on an event by event basis. In the $B^0 \to J/\psi K^0_S \pi^+\pi^-$ submode fits, a simultaneous fit to the $m^2(\pi^+\pi^-)$, $m^2(K^0_S\pi^\pm)$, and $m(J/\psi K^0_S\pi^+\pi^-)$ distributions could produce a more accurate answer than a fit to $m(J/\psi K^0_S\pi^+\pi^-)$ alone. With the full Run II dataset, a direct Dalitz plot fit would be best.

- Although cut based search techniques are standard within high energy physics, a statistically more powerful method would be to weight events by how signal-like they appear based upon their $p_T(K^{(*)0})$, $ct(B)$, and Iso(B) values. *I.e.*, rather than discard B candidates with $ct(B) < 100$ μm and keep the rest, events would be weighted as being more B-like if they have large $ct(B)$ and less B-like with small $ct(B)$. The quantitative assessment of the weights would require a detailed understanding of these distributions for both the signal and background samples. Our understanding of the B backgrounds in Run I was not sufficient to apply such a procedure.

- The $\Delta R < 1.0$ cut is $\sim 95\%$ efficient for the signal. Given that it was applied to particles both with respect to the J/ψ momentum direction and with respect to the other particle from the same parent, this cut was perhaps tighter than optimal. Future analyses should consider loosening this cut.

- For comparison to other analyses, a standardized definition of J/ψ and K^0_S candidates would have been useful. The CDF B physics analysis group seems to be moving in this direction for Run II.

- K^0_S mesons have a $c\tau$ of 2.7 cm, thus they often decay after the first layer of the SVX which is at a radius of 3 cm. This analysis did not explicitly exclude SVX information from layers at a smaller radius than the K^0_S decay vertex. This can lead to picking up noise tracks which degrade the K^0_S vertex fit. Work is in progress for a dedicated K^0_S finding algorithm in Run II which will include SVX II information from layers at a smaller radius than the K^0_S decay. Currently Ilya Kravchenko and Joe Boudreau are working on this algorithm but no CDF note is available.

- Although $p_T > 0.5$ GeV/c is a good background reducing cut for most final state particles, it may be too hard for the K^0_S daughter pions which tend to have lower momenta than other B decay daughters. A looser cut might be appropriate for these pions in order to increase the K^0_S finding efficiency.

Bibliography

[1] S. Dawson, SUSY and such, hep-ph/9612229. In *St. Croix 1996, Techniques and Concepts of High-Energy Physics IX* 33-80. (1996)

[2] T.D. Lee and C.N. Yang, Question of Parity Conservation in Weak Interactions, *Phys. Rev.* **104**, 254 (1956)

[3] C.S. Wu *et al.*, Experimental Test of Parity Conservation in Beta Decay, *Phys. Rev.* **105**, 1413 (1957)

[4] R. Garwin, L. Lederman, and M. Weinrich, Observations of the Failure of Conservation of Parity and Charge Conjugation in Meson Decays: the Magnetic Moment of the Free Muon, *Phys. Rev.* **105**, 1415 (1957)

[5] M. Gell-Mann and A. Pais, Behavior of Neutral Particles under Charge Conjugation, *Phys. Rev.* **97**, 1387 (1955)

[6] K. Lande *et al.*, Observation of Long-Lived Neutral V Particles. *Phys. Rev.* **103**, 1901 (1956)
W.F. Fry, J. Schneps, and M.S. Swami, Evidence for a Long-Lived Neutral Unstable Particle. *Phys. Rev.* **103**, 1904 (1956)

[7] J. H. Christenson *et al.*, Evidence for the 2π Decay of the K_2^0 Meson, *Phys. Rev. Lett.* **13**, 138 (1964)

[8] M. Kobayashi and T. Maskawa, CP-Violation in the Renormalizable Theory of Weak Interactions, *Prog. Theor. Phys.*, **49** 652 (1973)

[9] J.F. Donoghue, E. Golowich, and B.R. Holstein, Dynamics of the Standard Model, Cambridge University Press (1992)

[10] H. Fritzsch, The Kinematics and Dynamics of Flavor Mixing. *Acta Phys. Polon.* **B28** 2259-2277 (1997)

[11] D.E. Groom *et al.* (the Particle Data Group), The European Physical Journal **C15**, 1 (2000)

[12] L. Wolfenstein, Parametrization of the Kobayashi-Maskawa Matrix, *Phys. Rev. Lett.* **51**, 1945 (1983)

[13] A.D. Sakharov, Violation of CP Invariance, C Asymmetry, and Baryon Asymmetry of the Universe. *JETP Lett.* **5**, 24 (1967)

[14] P. Huet and E. Sather, Electroweak baryogenesis and standard model CP violation *Phys. Rev. D* **51**, 379 (1995)

[15] A.G. Cohen, D.B. Kaplan, and A.E. Nelson, Progress in Electroweak Baryogenesis, *Ann. Rev. Nucl. Part. Sci.* **43**, 27-70 (1993)

[16] T.E. Coan *et al.* (the CLEO Collaboration), Study of Exclusive Radiative B Meson Decays, *Phys. Rev. Lett.* **84** 5283 (2000)

[17] H.E. Haber, Low-Energy Supersymmetry and its Phenomenology, hep-ph/0103095
S. Dimopoulos and D. Sutter, *Nucl. Phys.* **B452**, 496 (1995)

[18] C. Gay, B Mixing, *Annu. Rev. Nucl. Part. Sci.* **50**, 577-641 (2000)

[19] T. Affolder *et al.* (The CDF Collaboration), Measurement of $\sin(2\beta)$ from $B \to J/\psi K^0_S$ with the CDF detector. *Phys. Rev. D* **61**, 072005 (2000)
B. Aubert *et al.* (The BaBar Collaboration), Measurement of CP-Violating Asymmetries in B^0 Decays to CP Eigenstates, *Phys. Rev. Lett.* **86**, 2515-2522 (2001)
A. Abashian *et al.* (The Belle Collaboration), Measurement of the CP Violation Parameter $\sin(2\phi_1)$ in B^0_d Meson Decays. *Phys. Rev. Lett.* **86**, 2509-2514 (2001)

[20] T. Affolder *et al.* (The CDF Collaboration) Measurement of the Decay Amplitudes of $B^0 \to J/\psi K^{*0}$ and $B^0_s \to J/\psi\phi$ Decays. *Phys. Rev. Lett.* **85** 4668-4673 (2000)

[21] C.P. Jessop *et al.* (The CLEO Collaboration), Measurement of the Decay Amplitudes and Branching Fractions of $B \to J/\psi K^*$ and $B \to J/\psi K$ Decays, *Phys. Rev. Lett.* **79**, 4533-4537 (1997)

[22] The CDF Collaboration, *The CDF II Detector Technical Design Report*, FERMILAB-Pub-96/390-E (November 1996)

[23] P.F. Harrison and H.R. Quinn, editors. The BaBar Physics Book. SLAC-R-504 (1998)

[24] Y. Grossman, Y. Nir, R. Rattazzi, CP Violation Beyond the Standard Model, in *Heavy Flavours II*, editors A.J. Buras and M. Lindner, Advanced Series on Directions in High Energy Physics, World Scientific Publishing Co., Singapore (1997)

[25] J.P. Marriner and M.D. Church, *Ann. Rev. of Nucl. and Part. Sci.* **43**, 253-295 (1993)
D.A. Finley, J. Marriner, and N.V. Mokhov, Tevatron Status and Future Plans. Presented at the Conference on Charged Particle Accelerators, Protvino, Russia, 22-24 October 1996. Fermilab-CONF-96-408. (1996)

[26] F. Abe *et al.* (the CDF Collaboration), The CDF Detector: An Overview, *Nucl. Instr. and Meth.* **A271**, 387-403 (1988)

[27] D. Amidei *et al.*, The Silicon Vertex Detector of the Collider Detector at Fermilab, *Nucl. Instr. and Meth.* **A350**, 73-130 (1994)

[28] F. Bedeschi *et al.*, Design and Construction of the CDF Central Tracking Chamber, *Nucl. Instr. and Meth.* **A268**, 50-74 (1988)

[29] G. Ascoli *et al.*, CDF Central Muon Detector, *Nucl. Instr. and Meth.* **A268**, 33-40 (1988)

[30] A. Anastassov *et al.* (the CLEO Collaboration), First Observation of the Decay $B \to J/\psi\phi K$, *Phys. Rev. Lett.* **84**, 1393 (2000)

[31] T. Affolder *et al.* (the CDF Collaboration), Measurement of b-Quark Fragmentation Fractions in $p\bar{p}$ Collisions at $\sqrt{s} = 1.8$ TeV. *Phys. Rev. Lett.* **84**, 1663 (2000).

[32] F. Abe *et al.* (the CDF Collaboration), J/ψ and $\psi(2S)$ Production in $p\bar{p}$ Collisions at $\sqrt{s} = 1.8$ TeV, *Phys. Rev. Lett.* **79**, 572-577 (1997)

[33] I. Dunietz *et al.*, How to extract CP-violating asymmetries from angular correlations, *Phys. Rev. D* **43**, 2193 (1991)

[34] T. Affolder *et al.* (the CDF Collaboration), Measurement of the Decay Amplitudes of $B^0 \to J/\psi K^{*0}$ and $B_s^0 \to J/\psi\phi$ Decays, *Phys. Rev. Lett.* **85**, 4668-4673 (2000)

[35] The Belle Collaboration, Observation of $B \to J/\psi K_1(1270)$, Reported at the XXXth International Conference on High Energy Physics, Osaka, July (2000)
http://bsunsrv1.kek.jp/conferences/ICHEP2000/conf0004.ps
To be published in "Proceedings of the 30th International Conference on High Energy Physics" Edited by C.S. Lim and T. Yamanaka, World Scientific Publishing Co. (2001)

[36] A.D. Martin, W.J. Stirling, and R.G. Roberts, Parton distributions updated, *Phys. Lett.* **B306**, 145 (1993)

[37] G.J. Feldman and R.D. Cousins, Unified Approach to the Classical Statistical Analysis of Small Signals, *Phys. Rev. D* **57**, 3873 (1998)

[38] S.J. Richichi *et al.* (the CLEO Collaboration), Study of $B \to \psi(2S)K$ and $B \to \psi(2S)K^*(892)$ decays, *Phys. Rev. D* **63**, 031103(R) (2001)

[39] R. Aleksan, I. Dunietz, and B. Kayser. Determining the CP-violating phase γ, *Z. Phys.* **C54**, 653-659 (1992)

[40] M. Beneke, A. Lenz, Lifetime Difference of B_s Mesons – Theory Status. Presented at UK Phenomenology Workshop of Heavy Flavour and CP Violation, 17-22 September 2000. Proceedings to appear in *J. Phys.* G. hep-ph/0012222 (2000)

[41] A.F. Falk and A.A. Petrov, Measuring γ Cleanly with CP-Tagged B_s and B_d Decays, *Phys. Rev. Lett.* **85** 252-255 (2000)

[42] R. Cousins, and V. Highland, Incorporating systematic uncertainties into an upper limit, *Nucl. Instr. and Meth. A320*, 331-335 (1992)

[43] W.D. Shephard (for the D0 Collaboration), A Study in Progress: D0 Measurement of ΔM_{B_s} Using $B_s \to J/\psi K^*$, Reported at the Run II B Physics Workshop, Fermilab, (February 2000)
http://http://www-theory.fnal.gov/people/ligeti/Brun2/febr/shephard.pdf

[44] R. Kutschke (for the BTeV Collaboration), The x_s Reach of BTeV, Talk at the Run II B Physics Workshop, Fermilab, (February 2000)
http://http://www-theory.fnal.gov/people/ligeti/Brun2/febr/kutschke2.ps.gz

[45] H.G. Moser and A. Roussarie, Mathematical methods for $B^0\bar{B}^0$ oscillation analyses, *Nucl. Instr. and Meth.* **A384**, 491-505 (1997)

[46] A.B. Wicklund (for the CDF Collaboration), CDF $\sin 2\beta \to J/\psi K^0_S$ in Run II, Talk at the Run II B Physics Workshop, Fermilab, (February 2000)
http://www-theory.fnal.gov/people/ligeti/Brun2/febr/wicklund1.ps.gz